

(NASA CR-161598) ADVANCED METHODS FOR
PREPARATION AND CHARACTERIZATION OF INFRARED
DETECTOR MATERIALS, Final Report, 5 Dec. 1978 ✓ *Pl. 1*
1.78 - 5 Jul. 1980 (McDonnell-Douglas
Technical Services) 159 p HC A08/MF A01

M81-20863

Unclas
29268

NASA CONTRACTOR REPORT

NASA CR-161598

ADVANCED METHODS FOR PREPARATION AND CHARACTERIZATION OF INFRARED DETECTOR MATERIALS, PART I

B. S. L. Lehoczky, F. R. Szofran, and B. G. Martin
McDonnell Douglas Research Laboratories
McDonnell Douglas Corporation

Interim Report

July 5, 1980

Prepared for

NASA - Marshall Space Flight Center
Marshall Space Flight Center, Alabama 35812

1. REPORT NO. NASA CR- 161596	2. GOVERNMENT ACCESSION NO.	3. RECIPIENT'S CATALOG NO.	
4. TITLE AND SUBTITLE Advanced Methods for Preparation and Characterization of Infrared Detector Materials, Part I		5. REPORT DATE July 5, 1980	
		6. PERFORMING ORGANIZATION CODE	
7. AUTHOR(S) S. L. Lehoczky, F. R. Szofran, and B. G. Martin		8. PERFORMING ORGANIZATION REPORT # MDC Q0717	
9. PERFORMING ORGANIZATION NAME AND ADDRESS McDonnell Douglas Research Laboratories McDonnell Douglas Corporation Box 516 St. Louis, Missouri 63166		10. WORK UNIT NO.	
		11. CONTRACT OR GRANT NO. NAS8-33107	
12. SPONSORING AGENCY NAME AND ADDRESS National Aeronautics and Space Administration Washington, DC 20546		13. TYPE OF REPORT & PERIOD COVERED Contractor Report	
		14. SPONSORING AGENCY CODE	
15. SUPPLEMENTARY NOTES Technical Monitor: Fred A. Reeves Prepared for George C. Marshall Space Flight Center, Marshall Space Flight Center, Alabama 35812			
16. ABSTRACT The pseudobinary HgTe-CdTe phase diagram was determined by precision differential-thermal-analysis measurements and was theoretically analyzed in terms of a regular associated solution model. $\text{Hg}_{0.8}\text{Cd}_{0.2}\text{Te}$ alloy crystals were grown by a Bridgman-Stockbarger method at furnace translation rates of 0.0685 to 5.62 $\mu\text{m/s}$. A theoretical analysis of the measured axial compositional profiles was used to establish the liquid HgTe-CdTe inter-diffusion coefficient and the liquid/solid-interface-temperature-gradient to growth-rate ratio required to prevent constitutional supercooling. Theoretical models based upon a microscopic theory of electrical conduction and computer programs specific to $\text{Hg}_{1-x}\text{Cd}_x\text{Te}$ were developed for calculations of charge-carrier concentrations, Hall coefficients, Fermi energy, and conduction-electron mobility as functions of x , temperature, and ionized-defect and neutral-defect concentrations. The measured and calculated results were in good agreement.			
17. KEY WORDS Crystal Growth, Semiconductors, Infrared Detectors, Mercury Cadmium Telluride, Phase Diagrams, Regular Associated Solutions, Electrical Properties, Theory of Electrical Conduction, Cadmium Telluride		18. DISTRIBUTION STATEMENT Unclassified--Unlimited	
19. SECURITY CLASSIF. (of this report) Unclassified	20. SECURITY CLASSIF. (of this page) Unclassified	21. NO. OF PAGES 161	22. PRICE NTIS

PREFACE

This report describes the work performed from December 5, 1978, through July 5, 1980, by the McDonnell Douglas Research Laboratories (MDRL) under the National Aeronautics and Space Administration (NASA) Contract NAS8-33107. The ultimate objectives of the study are to quantitatively establish the characteristics of $\text{Hg}_{1-x}\text{Cd}_x\text{Te}$ as grown on Earth as a basis for subsequent evaluation of the material processed in space and to develop the experimental and theoretical analytical methods required for such evaluation. The technical report was submitted to NASA in July 1980.

The work was performed in the Solid State Sciences Department, managed by Dr. C. R. Whitsett. The Principal Investigator was Dr. S. L. Lehoczky; Co-Investigators were Dr. F. R. Sofran and Dr. B. G. Martin.

CONTENTS

	<u>Page</u>
1. INTRODUCTION.....	1
1.1 Scope of Study.....	1
1.2 Summary of Progress.....	1
2. PSEUDOBINARY HgTe-CdTe PHASE DIAGRAM.....	4
2.1 Alloy Preparation.....	4
2.2 Experimental Method for Differential Thermal Analyses.....	6
2.3 Differential Thermal Analysis Results.....	8
2.4 Error Analysis and Comparison with Previous Results.....	18
2.5 Liquid-Solid Equilibrium Parameters.....	20
3. PHASE EQUILIBRIA CALCULATIONS.....	25
3.1 Theoretical Model.....	25
3.2 Regular Associated Solution Parameters for the HgCdTe Alloy System.....	29
3.3 Component Partial Pressures over the Pseudobinary Melt.....	32
4. HIGH-TEMPERATURE-GRADIENT DIRECTIONAL SOLIDIFICATION.....	36
4.1 Alloy Preparation.....	36
4.2 Experimental Arrangement and Procedures for Unidirectional Crystal Growth.....	36
4.3 Bridgman Crystal Growth Runs.....	38
4.4 Ingot Characterization.....	41
4.4.1 Determination of Alloy Composition by Mass Density Measurements.....	41
4.4.2 Infrared Transmission Measurements.....	46
4.5 Alloy Compositional Variation Along the Growth Axis.....	49
4.5.1 Theoretical Modeling.....	49
4.5.2 Comparison of Measured and Calculated Results.....	51

PRECEDING PAGE BLANK NOT FILMED

CONTENTS (continued)

	<u>Page</u>
5. THEORETICAL MODELING OF CHARGE-CARRIER CONCENTRATIONS AND ELECTRON MOBILITIES.....	65
5.1 Energy-Band Structure and Band Parameters.....	65
5.2 Calculation of the Temperature Dependence of the Carrier Concentrations.....	67
5.3 Theoretical Modeling of the Electron Mobility.....	72
5.4 Calculations of the Temperature Dependence of the Electron Mobility.....	74
REFERENCES.....	77
APPENDIX A: ELECTRON SCATTERING AND THE SOLUTION TO THE BOLTZMANN EQUATION.....	80
A.1 Longitudinal-Optical (LO) Phonon Scattering Mechanism.....	80
A.2 Acoustical-Phonon (ac) Scattering Mechanism.....	84
A.3 Ionized Impurity (ii) Scattering Mechanism.....	86
A.4 Electron-Hole (eh) Scattering Mechanism.....	88
A.5 Compositional-Disorder (dis.) Scattering Mechanism.....	88
A.6 Neutral-Defect (nd) Scattering Mechanism.....	89
A.7 Calculation of Electron Mobility.....	89
APPENDIX B: COMPUTER PROGRAM FOR CALCULATION OF CHARGE-CARRIER CONCENTRATIONS AND ELECTRON MOBILITIES.....	93
B.1 Description of Symbols - Main Program.....	93
B.2 Description of Symbols - Subroutine Programs.....	96
B.3 Computer Program Flow Charts.....	100
B.4 Computer Program.....	141

LIST OF ILLUSTRATIONS

<u>Figure</u>	<u>Page</u>
1. Experimental arrangement for differential thermal analysis measurements.....	7
2. Electronic instrumentation for differential thermal analysis.....	7
3. Rate dependence of thermal arrest for HgTe.....	9
4. Differential thermal analysis data for $\text{Hg}_{0.9}\text{Cd}_{0.1}\text{Te}$	10
5. Differential thermal analysis data for $\text{Hg}_{0.8}\text{Cd}_{0.2}\text{Te}$	11
6. DTA data for $x = 0.1, 0.2, 0.3, 0.4, 0.6, 0.7, 0.8,$ and $0.9 \text{ Hg}_{1-x}\text{Cd}_x\text{Te}$ alloys.....	12
7. $\text{Hg}_{1-x}\text{Cd}_x\text{Te}$ melting curves as observed.....	13
8. $\text{Hg}_{1-x}\text{Cd}_x\text{Te}$ phase diagram.....	17
9. Comparison of present phase-equilibria data with previous results.....	20
10. Temperature dependence of the interface distribution coefficient.....	21
11. Composition dependence of the distribution coefficient.....	22
12. Temperature dependence of the alloy liquid fraction for various alloy compositions.....	23
13. The temperature dependence of the rate of change with respect to temperature of the alloy liquid fraction for various alloy compositions.....	24
14. Compositional variation of the observed DTA signals as a function of sample temperature.....	24
15. Component partial pressures over the $\text{Hg}_{1-x}\text{Cd}_x\text{Te}$ melt.....	34
16. The temperature variation of Hg partial pressure over the $\text{Hg}_{1-x}\text{Cd}_x\text{Te}$ melt as a function of Cd fraction.....	35
17. Bridgman crystal-growth furnace assembly.....	37
18. Temperature profile of crystal-growth furnace during growth of ingot L3.....	39
19. Temperature profile of crystal-growth furnace during growth of ingot L4.....	40

LIST OF ILLUSTRATIONS (continued)

<u>Figure</u>	<u>Page</u>
20. Temperature profile of crystal-growth furnace during growth of ingots L6 and L7.....	40
21. (a) Location of wafers along the growth axis of ingot L6 and (b) the IR measurement positions for a wafer.....	47
22. Typical transmission spectra for a wafer (A26) from ingot L6...	48
23. Radial variations of the cut-on wavelength and Cd composition for ingot L6.....	48
24. Radial variation of wavelength at 50% relative transmission across slices from ingot L6.....	49
25. The variation of the interface segregation coefficient and interface translation rate along the growth axis of ingot L3...	53
26. The variation of the interface segregation coefficient and interface translation rate along the growth axis of ingot L4...	54
27. The variation of the interface segregation coefficient and interface translation rate along the growth axis of ingot L6...	55
28. A comparison between the measured and calculated compositional profiles for ingot L3.....	56
29. A comparison between the measured and calculated compositional profiles for ingot L4.....	57
30. A comparison between the measured and calculated compositional profiles for ingot L6.....	58
31. A comparison between the experimental data for ingot L3 and calculated results for various values of the diffusion coefficient.....	59

LIST OF ILLUSTRATIONS (continued)

<u>Figure</u>	<u>Page</u>
32. A comparison between the experimental data for ingot L4 and calculated results for various values of the diffusion coefficient.....	60
33. A comparison between the experimental data for ingot L6 and calculated results for various values of the diffusion coefficient.....	61
34. A comparison between the experimental data for ingot L3 and calculated results for a diffusion coefficient of $6.0 \times 10^{-5} \text{ cm}^2/\text{s}$ and constant k, R.....	62
35. A comparison between the experimental data for ingot L4 and the calculated results for a diffusion coefficient of $6.0 \times 10^{-5} \text{ cm}^2/\text{s}$ and constant k, R.....	63
36. A comparison between the experimental data for ingot L6 and the calculated results for a diffusion coefficient of $4.5 \times 10^{-5} \text{ cm}^2/\text{s}$ and constant k, R.....	64
37. Theoretical and experimental conduction-electron concentration for $\text{Hg}_{0.817}\text{Cd}_{0.183}\text{Te}$	69
38. A comparison of the temperature dependence of the calculated and measured conduction-electron mobilities for an alloy composition of $x = 0.183$	75
39. A comparison of the temperature dependence of the calculated and measured conduction-electron mobilities for an alloy composition of $x = 0.183$	76

LIST OF TABLES

<u>Table</u>	<u>Page</u>
1. Alloy samples prepared for the phase-diagram determinations.....	5
2. Elemental constituents of alloys used for the phase diagram determination.....	6
3. Measured phase-equilibria data for $\text{Hg}_{1-x}\text{Cd}_x\text{Te}$	15
4. Free-volume correction parameters and corrected liquidus temperatures.....	16
5. Liquidus and solidus temperatures for $\text{Hg}_{1-x}\text{Cd}_x\text{Te}$	17
6. Uncertainties of the solidus and liquidus temperatures.....	18
7. Best values for the fitting constants C_1 and D_1	21
8. R.A.S. parameters and thermodynamic data for the Hg-Cd-Te system.....	30
9. A comparison of experimental and calculated temperatures for $\text{Hg}_{1-x}\text{Cd}_x\text{Te}$	31
10. Mole fractions of species in liquid phase as functions of temperature.....	31
11. Calculated component partial pressures over the $\text{Hg}_{1-x}\text{Cd}_x\text{Te}$ melt.....	33
12. Average alloy compositions for various positions along the axis of ingot L3.....	44
13. Average alloy compositions for various positions along the axis of ingot L4.....	45
14. Average alloy compositions for various positions along the axis of ingot L6.....	46
15. Parameters for electron-mobility and charge-carrier- concentration calculation for $\text{Hg}_{1-x}\text{Cd}_x\text{Te}$ alloys.....	70

1. INTRODUCTION

1.1 Scope of Study

The overall study includes the entire range, $0 < x < 1$, of $\text{Hg}_{1-x}\text{Cd}_x\text{Te}$ alloy compositions. Crystals were prepared by the Bridgman method with a wide range of crystal growth rates and temperature gradients adequate to prevent constitutional supercooling under diffusion-limited, steady-state, growth conditions. The longitudinal compositional gradients for different growth conditions and alloy compositions were calculated and compared with experimental data to develop a quantitative model of the crystal growth kinetics for the $\text{Hg}_{1-x}\text{Cd}_x\text{Te}$ alloys, and measurements were performed to ascertain the effect of growth conditions on radial compositional gradients. The pseudobinary HgTe-CdTe constitutional phase diagram was determined by precision differential-thermal-analysis measurements and used to calculate the segregation coefficient of Cd as a function of x and interface temperature. Experiments will be conducted and theoretical analysis will be performed during the next phase of the program to determine the ternary phase equilibria in selected regions of the Hg-Cd-Te constitutional phase diagram, and electron and hole mobilities as functions of temperature will be analyzed to establish charge-carrier scattering probabilities. Computer algorithms specific to $\text{Hg}_{1-x}\text{Cd}_x\text{Te}$ were developed for calculations of the charge-carrier concentrations, charge-carrier mobilities, Hall coefficient, optical absorptance, and Fermi energy as functions of x , temperature, ionized donor and acceptor concentrations, and neutral-defect concentrations.

1.2 Summary of Progress

A series of differential-thermal-analysis (DTA) measurements was performed for $\text{Hg}_{1-x}\text{Cd}_x\text{Te}$ alloy compositions with $x = 0, 0.1, 0.2, 0.3, 0.4, 0.6, 0.7, 0.8, 0.9$, and 1.0 . The liquidus and solidus temperatures deduced from the DTA data were used to establish the pseudobinary HgTe-CdTe constitutional phase diagram. The segregation coefficient of Cd was determined as a function of x and interface temperature.

Iterative phase-equilibria calculations based on the regular associated solution (R.A.S.) theory^{1,2} were performed, and a set of R.A.S. parameters was

obtained by simultaneously least-squares-fitting the binary Hg-Te and Cd-Te³⁻⁶ and pseudobinary HgTe-CdTe phase diagrams. The R.A.S. parameters were used to calculate the activities of Hg, Cd, and Te₂ and their partial pressures over pseudobinary melts. The calculated mercury partial pressures are in reasonable agreement with Steininger's experimental results.⁷ The validity of the R.A.S. parameters and thus the calculated partial pressures are sensitively dependent upon necessary assumptions in the calculations; for example, negligible Te-Te association in the melt was assumed.

Hg_{0.8}Cd_{0.2}Te alloy crystals were grown by the Bridgman method at constant furnace translation rates of 0.0685, 0.310, 0.597, 1.12, and 5.62 $\mu\text{m/s}$. The temperature gradients at the solid-liquid interface, except for the 5.62 $\mu\text{m/s}$ growth rate, were adequate to prevent constitutional supercooling in the melts. For three of the ingots, the longitudinal compositional profiles were determined by precision density measurements and were compared with calculated profiles⁸ for various assumed values of D, the liquid HgTe-CdTe interdiffusion coefficient. The calculations included the variations in the interface translation rates and interface segregation coefficients during the growth process. These variations were calculated from the temperature profiles measured prior to each growth run, the measured compositional profiles, and phase equilibria data. The best fits to the data for the alloys with $x = 0.2$ yielded $5.5 \times 10^{-5} \text{ cm}^2/\text{s}$ for D and $1.5 \times 10^6 \text{ K}\cdot\text{s}/\text{cm}^2$ for G/R, the interface-temperature-gradient to growth-rate ratio required to prevent constitutional supercooling. Radial compositional variations were measured on thin slices from several ingots by infrared (IR) transmission-edge mapping. The radial compositional profiles deduced from the cut-on wavelengths implied concave solid/liquid interfaces for the entire lengths of the crystals.

Theoretical models and computer programs specific to Hg_{1-x}Cd_xTe were developed for calculations of charge-carrier concentrations, Hall coefficient, Fermi energy, and conduction-electron mobility as functions of x, temperature, and ionized-defect and neutral-defect concentrations. As in previous work on the HgCdSe alloy system^{9,10} the Kane three-band model¹¹ was used to describe the band structure of the HgCdTe alloys, and the best available band parameters were compiled from the literature. The temperature dependence of the electron concentration was calculated for various net donor concentrations from 4.2 K to 300 K, and the calculated results agreed well with available data.

The mobility calculations included the following intrinsic scattering mechanisms: longitudinal-optical phonon, longitudinal and transverse-acoustical phonon, heavy-hole, and alloy disorder potential. The extrinsic scattering mechanisms included charged and neutral point-defects. A comparison of calculated results with available experimental data indicated that longitudinal optical-phonon and charged and neutral defect scattering are the dominant mobility-limiting mechanisms.

2. PSEUDOBINARY HgTe-CdTe PHASE DIAGRAM

2.1 Alloy Preparation

The HgTe-CdTe alloys used for the phase diagram determinations were prepared by reacting the constituent elements in sealed, fused-silica, 5-mm i.d. x 10-mm o.d. ampules. The ampules were cleaned and etched in aqueous HF and annealed at 1150°C in vacuum to remove residual contaminants. Square cross-section bars of 99.9999% pure Cd and Te were cut from large ingots. The Cd bars were etched in concentrated HNO₃ and repeatedly rinsed in methanol. The Te bars were etched in Br₂ and repeatedly rinsed in methanol. The ampules were loaded in a vertical position first with 99.9999% pure Hg, then Te, and finally Cd. This procedure prevented contact between Hg and Cd in the presence of air. The ampules were evacuated and backfilled with He several times before final evacuation and sealing. Using the above procedure, little or no wetting occurred between the ampule and the alloy during reaction of the elements. In many cases, the reacted alloy would slide inside the ampule.

The various alloy preparations used for the phase diagram determinations are summarized in Table 1. As implied by the table, a substantial number of prepared ampules were discarded for various reasons. Following a series of initial experimental runs, a concentrated effort was undertaken to increase the fill factor (reduce the free-volume) of the ampules. For this purpose, a series of alloys was cast, the ampules were reopened, solid quartz rods were placed in the ampules, and the ampules were resealed. For the ampules containing alloy compositions of $x = 0.1$ and 0.2 , the rod diameters were 4 mm. For alloy compositions with x -values of 0.3 to 0.9 , 5-mm diameter rods, etched in concentrated hydrofluoric acid to achieve close fits, were used. With the exceptions of the 0.1 and 0.2 alloys, this sealing procedure repeatedly resulted in ampule ruptures at the measurement temperatures, and the cause of these failures is unclear.

In subsequent preparations of alloys in the high- x range, an increase of the alloy volume in the ampule was used to increase the ampule fill-factor. The alloy constituents for the ampules that served as samples for the majority of the measurements described in this report are listed in Table 2.

TABLE 1. ALLOY SAMPLES PREPARED FOR THE PHASE-DIAGRAM DETERMINATIONS.

Sample no.	Composition (x)	Quantity (moles)	Comments *
1	0.1	0.02	A, B
2	0.2	0.02	A, B
3	0.2	0.06	A, C
4	0.1	0.06	A, C
5	0.4	0.06	A, B, C
6	0.3	0.06	A, C
7	0.5	0.06	A
8	0.6	0.06	A
9	0.7	0.06	A, B
10	0.8	0.06	A, B
11	0.9	0.06	B
12	0.8	0.06	B
13	0.2	0.06	C
14	0	0.06	A, C
15	0	0.06	D
16	1.0	0.03	D
17	0.7	0.06	B
18	0.5	0.06	C, F
19	0.7	0.06	C, F
20	0.8	0.06	C, F
21	0.1	0.06	D
22	0.2	0.06	D
23	0.3	0.06	C, F
24	0.4	0.06	D
25	0.9	0.06	C, F
26	0.8	0.06	C
27	0.9	0.06	C
28	0.9	0.12	D
29	0.8	0.12	D
30	0.7	0.12	C
31	0.6	0.12	C
32	0.6	0.12	C
33	0.7	0.12	C
34	0.5	0.12	C
35	0.3	0.06	D
36	0.5	0.06	C
37	0.6	0.06	C
38	0.5	0.06	C
39	0.6	0.06	D
40	0.7	0.06	D

* A - Used for preliminary experiments
 B - Some sticking of alloy to ampule
 C - Ampule burst

D - Used for measurements reported here
 E - 0.4 mm diam rod sealed inside after reacting alloy
 F - As E, except that an HF-etched 0.5-mm rod was used

GP03-0750-60

TABLE 2. ELEMENTAL CONSTITUENTS OF ALLOYS USED FOR THE PHASE
DIAGRAM DETERMINATION. MASS MEASUREMENT ACCURACY
IS ± 0.56 mg.

Composition (x)	Hg (g)	Cd (g)	Te (g)	Stoichiometric Hg (g)	Excess Hg (mg)
0.1	10.8349	0.6732	7.6555	10.8345	0.4
0.2	9.6299	1.3501	7.6570	9.6289	1.0
0.3	9.5487	2.2950	8.6748	9.5428	5.9
0.4	7.2201	2.6992	7.6555	7.2190	1.1
0.6	4.5719	3.8343	7.2582	4.5687	3.2
0.7	3.6452	4.7582	7.7183	3.6433	1.9
0.8	4.7977	10.7427	15.2430	4.7939	3.8
0.9	2.4093	12.1474	15.3200	2.4083	1.0

GP03-0750-3

2.2 Experimental Method for Differential Thermal Analyses

Differential thermal analysis (DTA) measurements were used for the determination of the phase equilibria temperatures. The experimental arrangement of the ampules in the DTA furnace is shown in Figure 1.

An ampule containing the alloy sample is mounted end-to-end with a second ampule coaxially inside the 460-mm long isothermal furnace liner (Na heat pipe) and the 610-mm long tube furnace. The second ampule contains antimony, which in addition to serving as the reference heat capacity provides a thermocouple calibration point for each experimental run. The ampules are held on axis by a quartz centering fixture (not shown in the figure). The annular volume between the ampules and a 25-mm o.d. quartz tube is filled with powdered diatomaceous earth. The 25-mm tube is inside an Inconel tube, which prevents damage to the heat pipe and furnace in case of ampule failure.

Both the alloy and Sb-reference ampules are fitted with a Pt-foil band ~5-mm wide and positioned near the middle of the ampule axially. The two junctions of a type-K differential thermocouple are secured to the bands. A separate type-K thermocouple is secured to the band on the Sb-reference ampule. Each thermocouple lead extends to a copper junction maintained in a triple-point-of-water cell. A block diagram of the furnace control and data acquisition instrumentation is shown in Figure 2. The temperature of the Sb-reference sample was monitored on the x-axis, and the differential

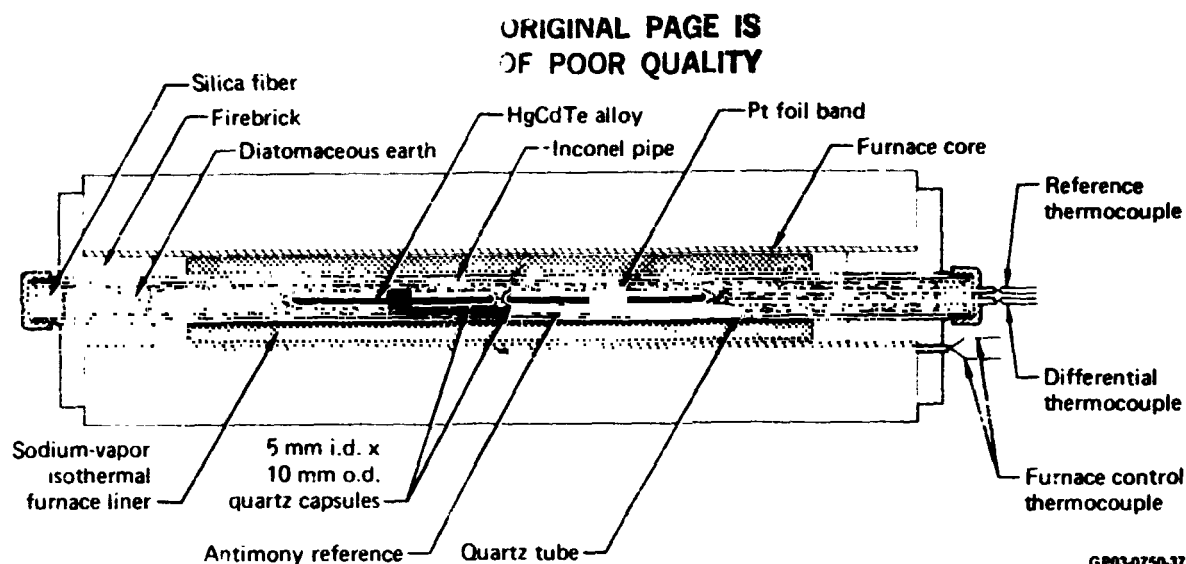


Figure 1. Experimental arrangement for differential thermal analysis measurements.

thermocouple output on the y-axis of an x-y recorder. Each graph-paper used for data recording was calibrated by drawing vertical lines at 1-mV intervals by driving the x-axis with a potentiometer (Leeds and Northrop model 8691). This potentiometer was in turn periodically checked against another potentiometer (Leeds and Northrop K-4) and verified to be accurate to within $\pm 20 \mu\text{V}$. The output of a type-K thermocouple is approximately $40 \mu\text{V}/\text{deg}$.

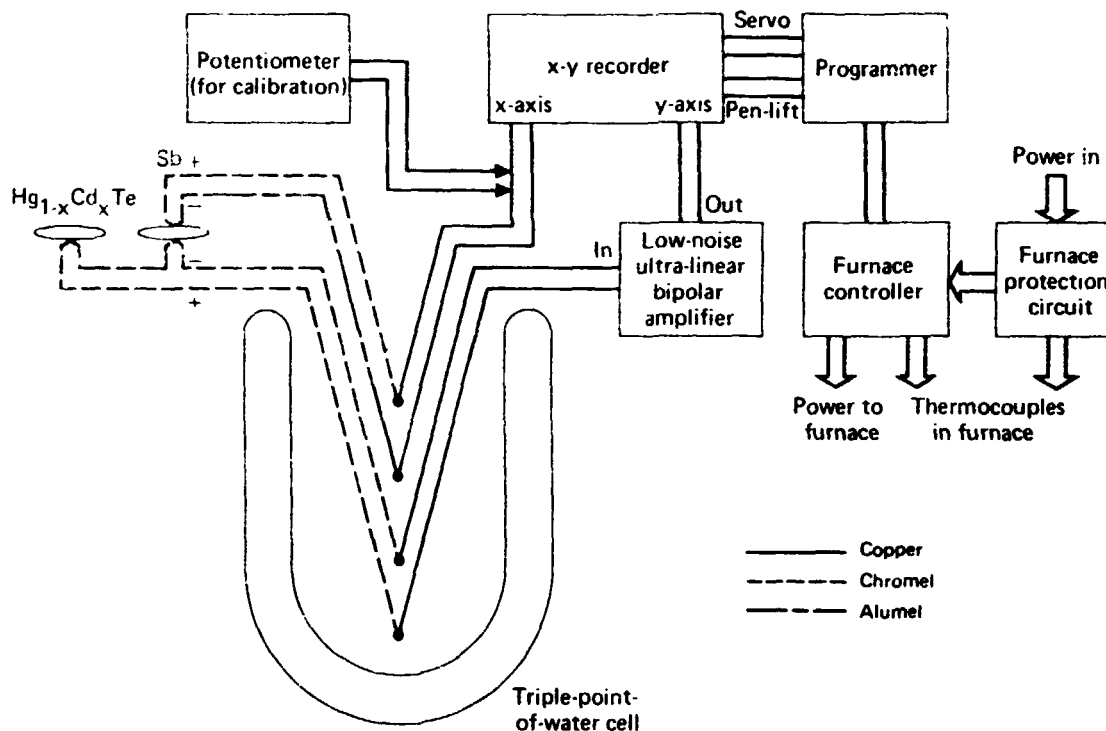


Figure 2. Electronic instrumentation for differential thermal analysis.

The temperature programmer allows the furnace temperature to be changed at a uniform rate and turns the x-y recorder servo and pen-lift on and off. The furnace protection circuit, a meter relay which drives a power relay, provides an additional margin of safety against excessive furnace temperatures.

A thermocouple calibration facility, similar to that described in NBS Circular 590¹², using graphite crucibles and NBS reference materials¹² was constructed and used to calibrate thermocouple wire lots used for the measurements. The melting-temperature reference materials were Zn, Al, and Cu. The melting temperature of the Sb-reference sample served as an internal calibration temperature, and the Sb melting point was checked at least once prior to each experimental run.

2.3 Differential Thermal Analysis Results

Generally, for DTA measurements, the output signal from the differential sensors varies directly with the heating/cooling rates used, i.e., high heating/cooling rates yield larger signals and thus better signal to noise ratios. Measurements made at too high heating/cooling rates, however, can significantly alter the details of the DTA curves, thereby yielding phase transformation temperatures that do not reflect true equilibrium values. To assure that heating/cooling rates used in this study were within the allowable range, HgTe calibration sample test runs were made at a series of heating rates (0.5, 1, 2, 3, 4, and 5°C/min). The thermal arrest curves for the various runs are shown in Figure 3. The melting temperatures deduced from the heating curves are within $\pm 1.7^\circ\text{C}$ of 669.5°C for the different heating rates, and there is no evidence for systematic variation of the onset of thermal-arrest with heating rate. Because the maximum cooling rate of the furnace at or below 670°C was about $3^\circ\text{C}/\text{min}$, all alloy heating and cooling curves were recorded at a rate of $2^\circ\text{C}/\text{min}$ in order to enhance the differential thermocouple outputs while allowing identical heating and cooling rates.

Alloy inhomogeneities broaden the range of temperatures over which transformations occur and thus introduce significant uncertainties into the phase equilibria temperatures as deduced from DTA. For this reason, the samples were always rapidly quenched following casting and uniformly cooled

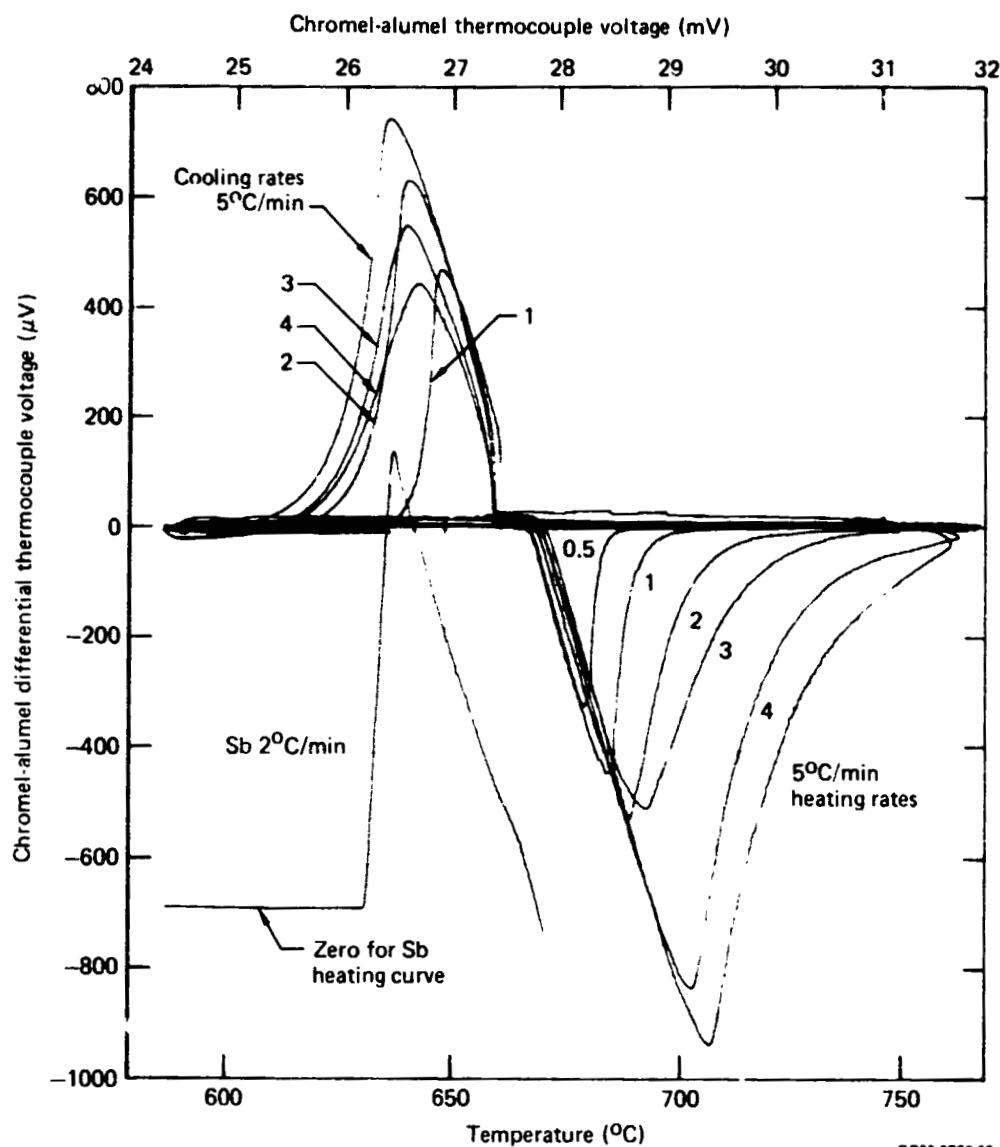


Figure 3. Rate dependence of thermal arrest for HgTe.

after each DTA run to reduce the possibility of preferential alloy segregation along the sample axis. To eliminate radial alloy inhomogeneities, the samples were annealed at temperatures, T_A , just below their solidus values. To ascertain the minimum annealing times required, samples with $x = 0.1, 0.2, 0.8$ and 0.9 were annealed for successively longer annealing times from 1 to 60 h, and a DTA run was made following each anneal. An increase in the annealing time from 1 to 15 h always resulted in a significant sharpening of the DTA

ORIGINAL PAGE IS
OF POOR QUALITY

curves in the vicinity of the apparent solidus temperatures, which indicates that the annealing effected alloy homogenization by diffusion. On the other hand, the changes caused by increasing the annealing time beyond 30 h were usually negligible, as shown for samples with $x = 0.1$ and 0.2 in Figures 4 and 5, respectively, where T_A and T_L correspond respectively to the annealing and liquidus temperatures, and the symbols 1, 2, 3, and 4 designate the DTA curves that were obtained following annealing times of 1, 15, 30 and 60 h, respectively.

DTA curves for fully annealed samples with $x = 0.1, 0.2, 0.3, 0.4, 0.6, 0.7, 0.8,$ and 0.9 are shown in Figure 6, and the collection of melting curves is shown in Figure 7. The horizontal axis shows the measured Sb-reference ampule temperature, T , and the vertical axis gives differential temperatures, S , for the alloy ampule as measured with respect to T .

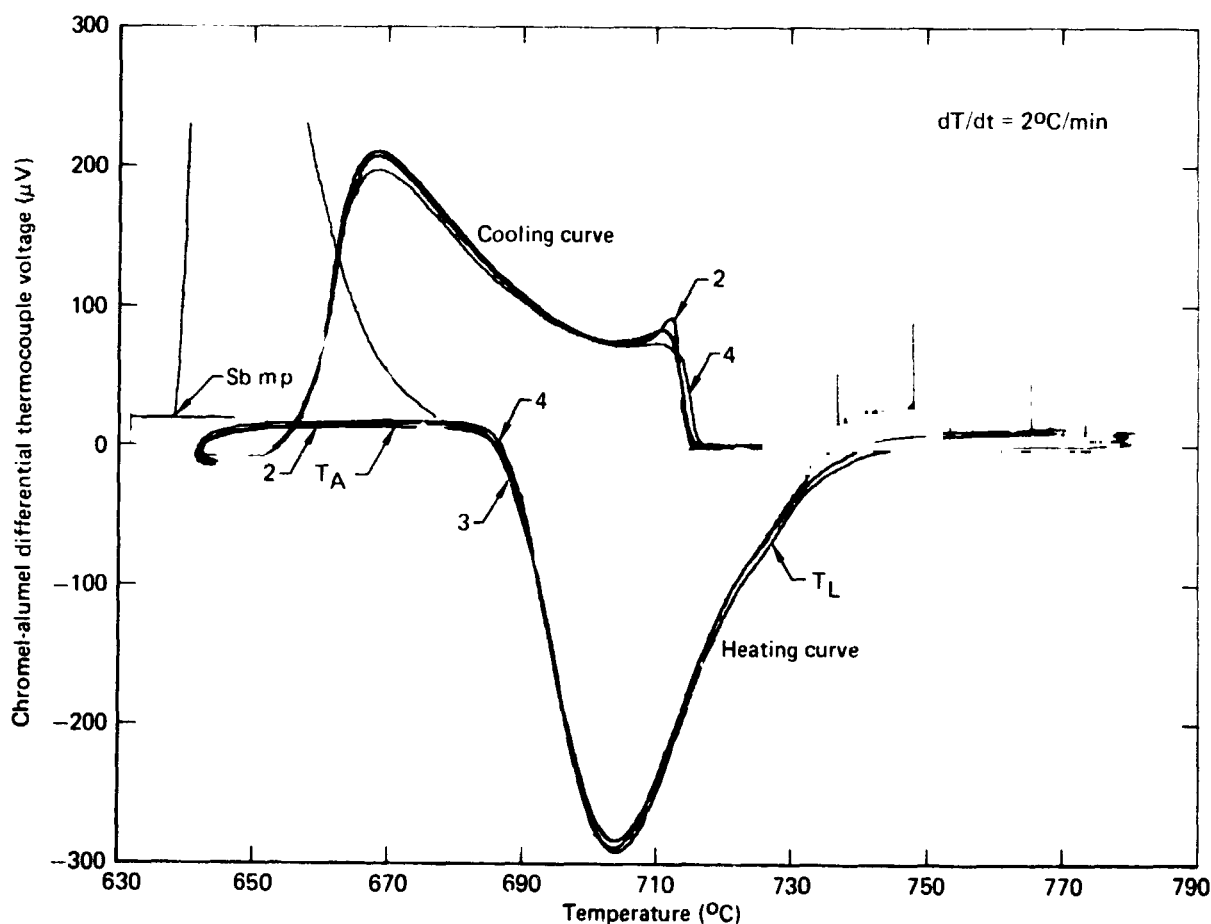


Figure 4. Differential thermal analysis data for $Hg_{0.9}Cd_{0.1}Te$.

GP03-0750-28

ORIGINAL PAGE 19
OF POOR QUALITY

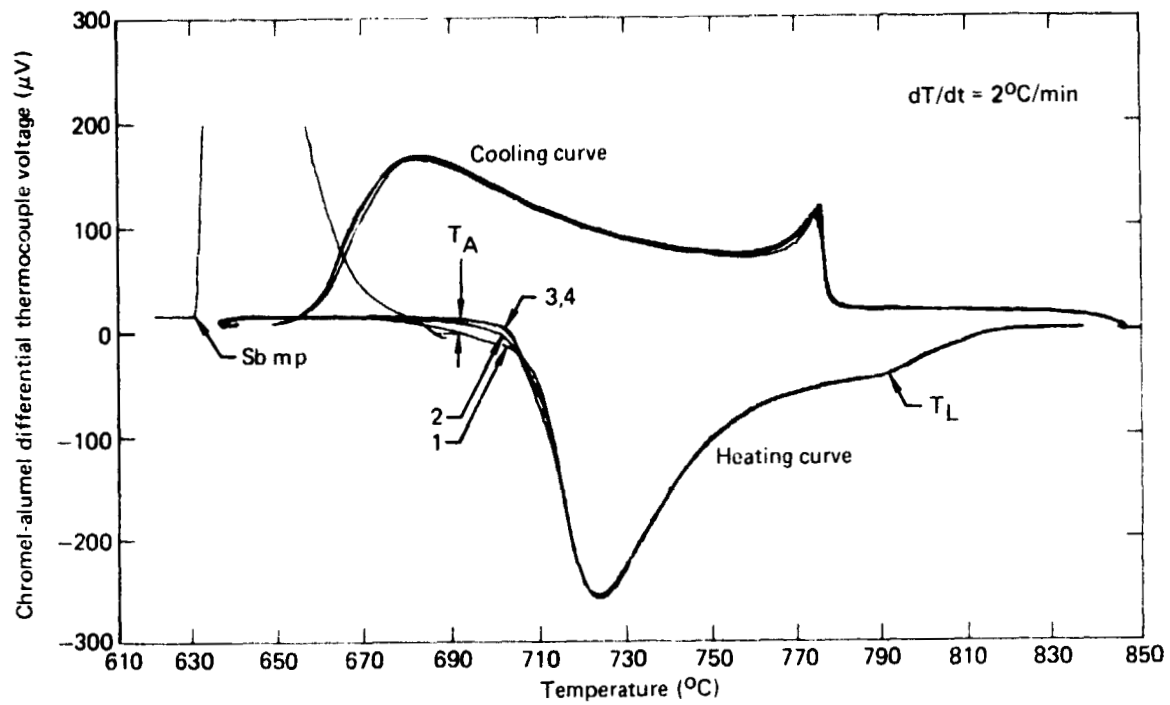
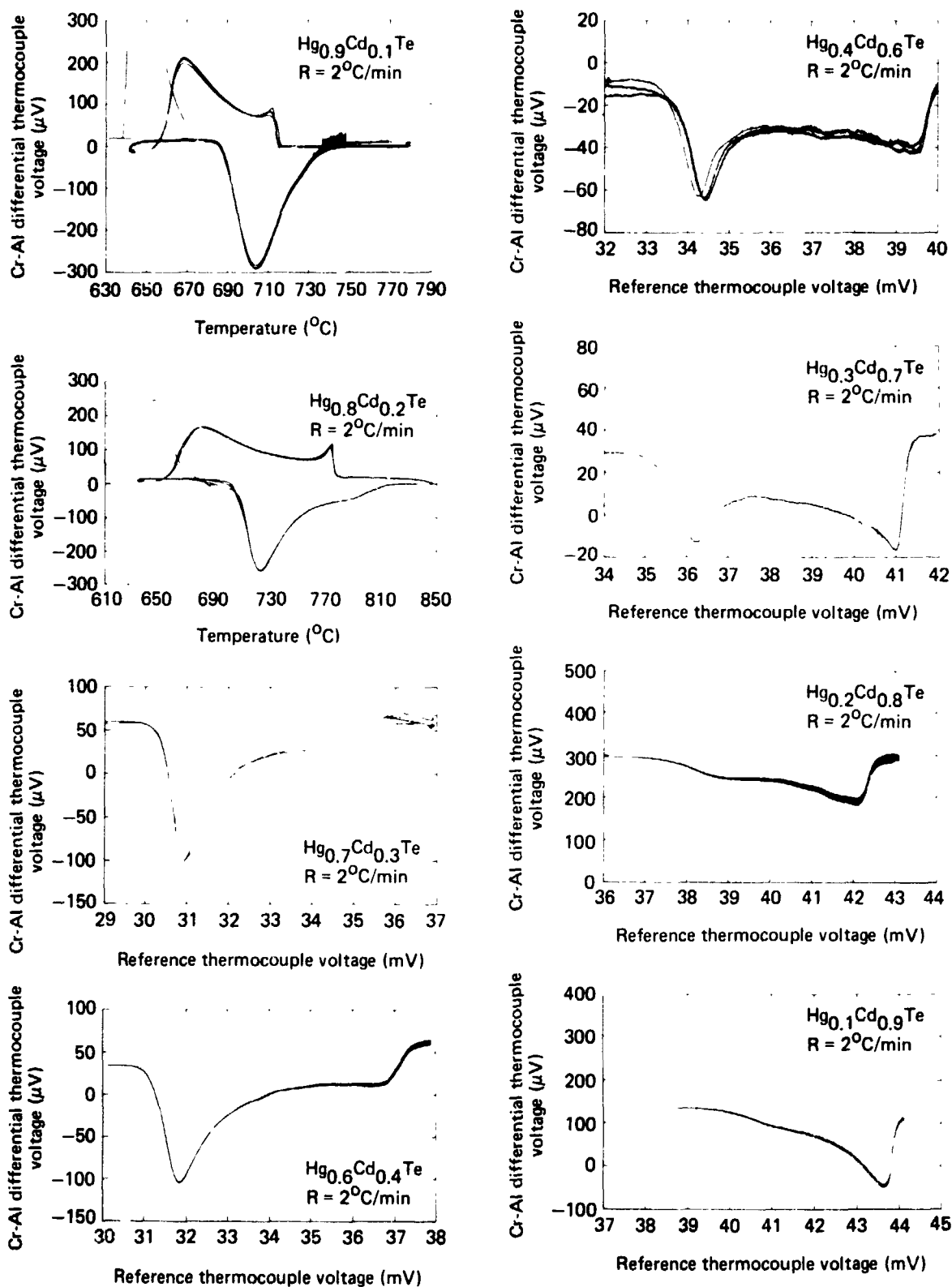


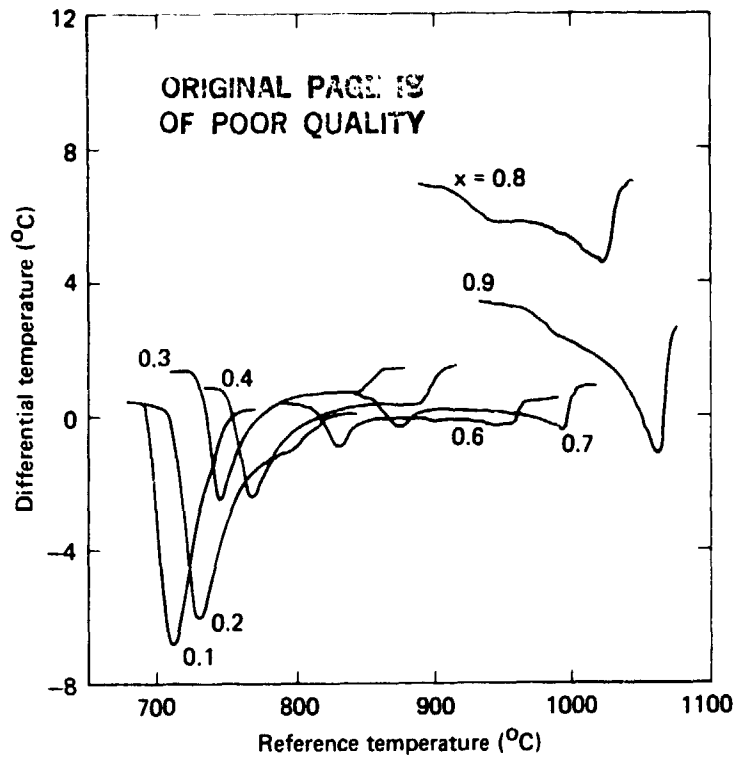
Figure 5. Differential thermal analysis data for $\text{Hg}_{0.8}\text{Cd}_{0.2}\text{Te}$.

GP03-0750-27



GP03-0750-29

Figure 6. DTA data for $x = 0.1, 0.2, 0.3, 0.4, 0.6, 0.7, 0.8$ and $0.9 \text{Hg}_{1-x}\text{Cd}_x\text{Te}$ alloys.



GP03-0750-25

Figure 7. $\text{Hg}_{1-x}\text{Cd}_x\text{Te}$ melting curves as observed.

Considering radiation heat transfer only, the heat balance at the outer wall of the sample ampule yields

$$\epsilon_F T_F^4 - \epsilon_p T_l^4 = \frac{r_s}{r_q} (\epsilon_p T_l^4 - \epsilon_s T_s^4), \quad (1)$$

where T_F , T_l , and T_s are the furnace, sample thermocouple, and sample temperatures, respectively, ϵ_F , ϵ_s , and ϵ_p are the furnace, sample, and quartz emissivities, respectively, and r_s and r_q are the inner and outer radii, respectively, of the quartz ampules. The measured differential thermocouple signal is given by $S = T_l - T$. For steady-state conditions where the furnace temperature increases at a constant rate, $T = T_F + P'$, where P' is a constant. Using the approximations

$$T_l^4 = (T + S)^4 \approx T^4 + 4ST^3 \quad (2)$$

and

$$T_F^4 = (T + P')^4 \approx T^4 + 4P'T^3, \quad (3)$$

Equation (1) yields

$$T_s^4 = T^4 \left[\left(1 + \frac{r_q}{r_s} \right) \frac{\epsilon_p}{\epsilon_s} - \frac{r_q}{r_s} \frac{\epsilon_F}{\epsilon_s} \right] + 4ST^3 \left(1 + \frac{r_q}{r_s} \right) \frac{\epsilon_p}{\epsilon_s} - 4P'T^3 \frac{r_q}{r_s} \frac{\epsilon_F}{\epsilon_s}. \quad (4)$$

A first-order expansion in ϵ/T and P'/T yields

$$T_s = a_1 T + a_2 S - a_3 P', \quad (5)$$

where a_1 , a_2 , and a_3 are functions of r_q/r_s , ϵ_p/ϵ_s , and ϵ_F/ϵ_s .

For HgTe the observed empirical correlation between T , S , and T_s is given by

$$T_s = T + 2S - P. \quad (6)$$

For CdTe also, a_2 was found to be 2. In the case of a nonzero baseline, S_0 , T_s is given by

$$T_s = T - S_0 + 2S - P. \quad (7)$$

P is primarily the temperature drop across the ampule wall, but this term also includes thermocouple calibration corrections. In the absence of a phase transition, $T_s = T + S_0 - P$, i.e., the sample temperature is equal to the reference thermocouple temperature plus the differential temperature minus the temperature drop across the ampule wall.

For each sample, P was determined by the difference between the observed and actual melting points of the Sb-reference. The values measured for P using other calibration samples with known melting points ranged from 1.3°C to 3.4°C, which agree reasonably with finite-difference calculations that include both radiation and conduction heat transfer.

The solidus temperatures were determined by replotting the data of Figure 6 as a function of T_s instead of T , using Equation (7). The solidus temperatures for $0.1 < x < 0.7$ were determined by extrapolating the initial, straight-line part of the replotted melting curves to the extended baseline. For $x = 0.8$ and 0.9 , the initial departure from the baseline was used because the melting curves had no straight-line sections even when replotted as functions of T_s . The liquidus points, in all cases, were considered to be the temperatures at which the melting curves broke suddenly toward the baseline. The observed phase equilibrium data are listed in Table 3.

TABLE 3. MEASURED PHASE-EQUILIBRIA DATA FOR $\text{Hg}_{1-x}\text{Cd}_x\text{Te}$.

Composition (x)	S_0 at solidus (°C)	S_0 at liquidus (°C)	P (°C)	Observed solidus temperature (°C)	Observed liquidus temperature (°C)
0.1	0.5	-1.5	2.9	690	733
0.2	0.4	-1.0	2.9	706	791
0.3	1.4	0.7	2.9	727	841
0.4	0.9	0.3	3.4	748	882
0.6	0.3	-0.3	1.3	810	952
0.7	0.7	-0.4	2.9	850	990
0.8	6.9	4.6	2.9	904	1022
0.9	3.4	-1.0	2.9	950	1051

GP03-0750-4

Each ampul. contained a small free volume. Because the partial vapor pressure of Hg over the alloy melt is much larger than the partial pressures of Cd and Te,^{7,14} the preferential evaporation of mercury into the ampule free volume alters both the Te/metal and Cd/Hg fractions. As suggested by the decrease of the binary Hg-Te and Cd-Te liquidus temperatures with increasing Te composition immediately above the 50 at.% Te composition,^{3,5,6,15} an increase in the Te/metal fraction can significantly affect the liquidus temperature. The Cd-Te liquidus temperature decreases at $\sim 10^\circ\text{C}/\text{at.}\% \text{ Te}$ ^{5,6}, and the Hg-Te liquidus temperature decreases at $1.2^\circ\text{C}/\text{at.}\% \text{ Te}$.^{3,15}

The following procedure was used to correct for the small Te-metal excess in the melt caused by preferential evaporation of Hg into the ampule free volume. Following the casting of an alloy, the free volume was estimated by measuring the length of the free space in the ampule. The amount of Hg in the gas phase was determined by using Steininger's⁷ empirical relationship for the Hg partial pressure, P, given by

$$P = P_0 \exp(21.732 - T_0/T), \quad (8)$$

where $P_0 = 1 \text{ Pa}$ and $T_0 = 7.149 \text{ K}$. The number of moles of Hg, n_{Hg} , remaining in the melt was obtained by subtracting the amount of Hg in the vapor from the amount loaded into the ampule. The actual Te/metal mole fraction in the melt at the observed liquidus temperature is then $n_{\text{Te}}/(n_{\text{Hg}} + n_{\text{Cd}} + n_{\text{Te}})$, where n_{Cd} and n_{Te} are respectively the number of moles of Cd and Te in the melt. The relatively small amounts of Cd and Te₂ in the vapor were neglected, and the

values of n_{Cd} and n_{Te} were assumed to be the same as originally placed in the ampule. The corrections to the observed liquidus temperatures were then obtained from the expression

$$\epsilon = \left[\frac{n_{Te}}{n_{Hg} + n_{Cd} + n_{Te}} \right] - 0.5 \quad (1.2 + 8.8x), \quad (9)$$

which is based on a linear interpolation between Hg-Te and Cd-Te of the rate of change of the liquidus temperature with respect to the Te concentration for Te mole fractions slightly above 0.5. The measured free volumes, the calculated atomic Te concentrations, the estimated temperature corrections for free-volume effects, and the corrected liquidus temperatures are summarized in Table 4.

Table 5 lists the liquidus and solidus temperatures determined in this investigation. Table 5 also gives the corrected x-values based on $x = n_{Cd}/(n_{Cd} + n_{Hg})$. The phase diagram data are plotted in Figure 8.

TABLE 4. FREE-VOLUME CORRECTION PARAMETERS AND CORRECTED LIQUIDUS TEMPERATURES.

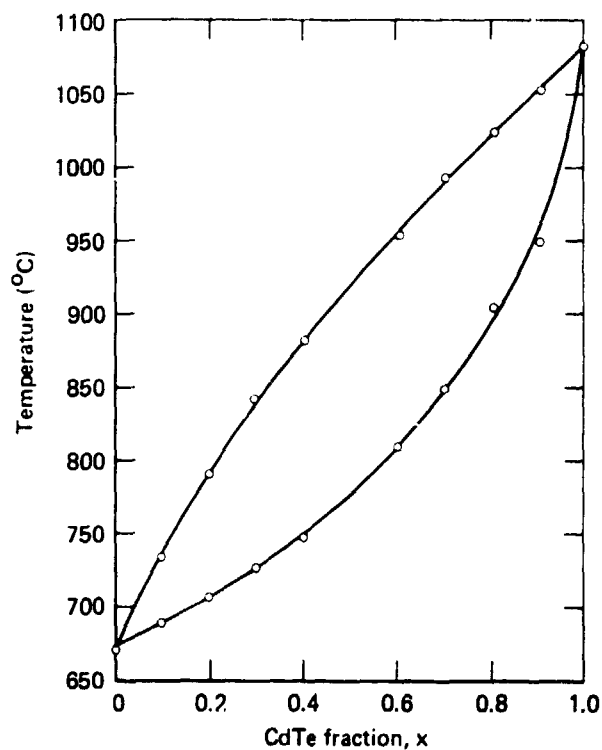
Cd composition (x)	Capsule free volume (cm ³)	Te fraction (%)	Liquidus temperature correction (°C)	Observed liquidus temperature (°C)	Corrected liquidus temperature (°C)
0.1	0.19	50.02	0	733	733
0.2	0.26	50.04	0.1	791	792
0.3	0.69	50.11	0.4	841	841
0.4	0.88	50.21	1.0	882	884
0.6	0.96	50.33	2.1	952	954
0.7	0.74	50.27	2.0	990	992
0.8	1.46	50.31	2.5	1022	1025
0.9	0.87	50.20	1.9	1051	1053

GP03-0750-5

ORIGINAL PAGE IS
OF POOR QUALITY
TABLE 5. LIQUIDUS AND SOLIDUS TEMPERATURES FOR $\text{Hg}_{1-x}\text{Cd}_x\text{Te}$.

Nominal composition (x)	Actual composition at solidus (x)	Solidus temperature (°C)	Actual composition at liquidus (x)	Liquidus temperature (°C)
0.1	0.100	690	0.100	733
0.2	0.200	706	0.200	792
0.3	0.301	727	0.302	841
0.4	0.402	748	0.404	884
0.6	0.604	810	0.607	954
0.7	0.704	850	0.707	997
0.8	0.806	904	0.810	1050
0.9	0.905	950	0.907	1050

GP03-0750-6



GP03-0750-18

Figure 8. $\text{Hg}_{1-x}\text{Cd}_x\text{Te}$ phase diagram.

2.4 Error Analysis and Comparison with Previous Results

The major recognized sources of error in the phase diagram data are the thermocouple calibrations, the subjectivity in selecting the proper phase-transformation points from the DTA curves, and the uncertainties in the ampule free-volume corrections.

Because the Sb melting point (630.7°C) was used to calibrate the thermocouples during each DTA run, the calibration should be quite accurate near that temperature and decrease in accuracy with increasing temperature. A type-K thermocouple calibrated at 630.7°C should be accurate to within $\pm 2^{\circ}\text{C}$ up to 930°C .^{12,16} The measured melting temperature of a Ag standard sample differed from the IPTS-68 value of 930°C by not more than $\pm 3^{\circ}\text{C}$ in tests of three different thermocouple combinations used during the course of this investigation. Therefore, the expression $3(T - 631^{\circ}\text{C})/(930 - 631)$ was used as the calibration uncertainty at temperature T, which is equivalent to an uncertainty at the Ag melting point of 3.3°C and is considered adequate to include any graph-paper calibration errors as well as thermocouple calibration errors. For each sample, the calculated uncertainties arising from the temperature measurement uncertainties are listed in Table 6.

TABLE 6. UNCERTAINTIES OF THE SOLIDUS AND LIQUIDUS TEMPERATURES.

Composition (x)	Solidus temperatures			Liquidus temperatures			
	Temperature calibration ($^{\circ}\text{C}$)	Reading DTA curve ($^{\circ}\text{C}$)	Total ($^{\circ}\text{C}$)	Temperature calibration ($^{\circ}\text{C}$)	Reading DTA curve ($^{\circ}\text{C}$)	Free volume effect ($^{\circ}\text{C}$)	Total ($^{\circ}\text{C}$)
0.1	0.6	1.0	1.6	1.0	3.0	0	4.0
0.2	0.8	1.0	1.8	1.6	1.0	0	2.6
0.3	1.0	1.0	2.0	2.1	1.0	0.1	3.2
0.4	1.2	1.0	2.2	2.5	1.0	0.3	3.8
0.6	1.8	2.0	3.8	3.2	1.0	0.5	4.8
0.7	2.2	1.0	3.2	3.6	1.0	0.5	5.1
0.8	2.7	2.0	4.7	3.9	2.0	0.6	6.6
0.9	3.2	2.0	5.2	4.2	2.0	0.5	6.7

GP03-0750 7

(4)

The second source of error is in determination of the critical points of the DTA curves. For the solidus points, the extrapolation of the S vs T_s curve to the baseline for alloys with $0.1 \leq x \leq 0.7$ and the choice of the onset of deviation from the baseline for alloys with $x = 0.8$ or 0.9 are somewhat subjective. Similarly, there were uncertainties in identifying the liquidus points. The latter uncertainties were about 1°C except for the $x = 0.1$ sample, for which the liquidus onset occurred where the curve had a very steep slope, and for the $x = 0.8$ and 0.9 samples, for which the sharpness of the liquidus onset was somewhat more rounded as shown in Figure 6. Estimates of subjectivity in reading the DTA curves are given in Table 6 under the columns headed "Reading DTA Curve."

The uncertainties listed for the free-volume corrections are 25% of the total free-volume corrections.

The total uncertainties listed in Table 6 are the sums of the individual uncertainties and are believed to represent the maximum possible errors in the reported phase-equilibria temperatures.

The solidus and liquidus temperatures are compared with the results of previous investigations in Figure 9. The data of Ray and Spencer¹⁷ and Blair and Newnham¹⁸ were derived from DTA measurements. Harman's¹⁹ data are from chemical analyses of first-to-freeze regions of molten alloy samples. Steininger's⁷ data were derived from thermal analyses of samples in a high-pressure apparatus.

A DTA measurement tends to yield too low a solidus temperature for a given x because of possible inhomogeneities in the sample. The inherent error of the first-to-freeze method tends to yield too low an x value for a given temperature. Therefore, on a temperature-composition plot, a solidus curve determined by the first-to-freeze compositions should fall at or above the true curve, and a solidus curve determined by DTA measurements should fall at or below the true curve. The present DTA data establish a solidus curve that nearly coincides with the lower limit of Harman's first-to-freeze data, and the two independent sets of data thus are corroborative.

ORIGINAL PAGE IS
OF POOR QUALITY

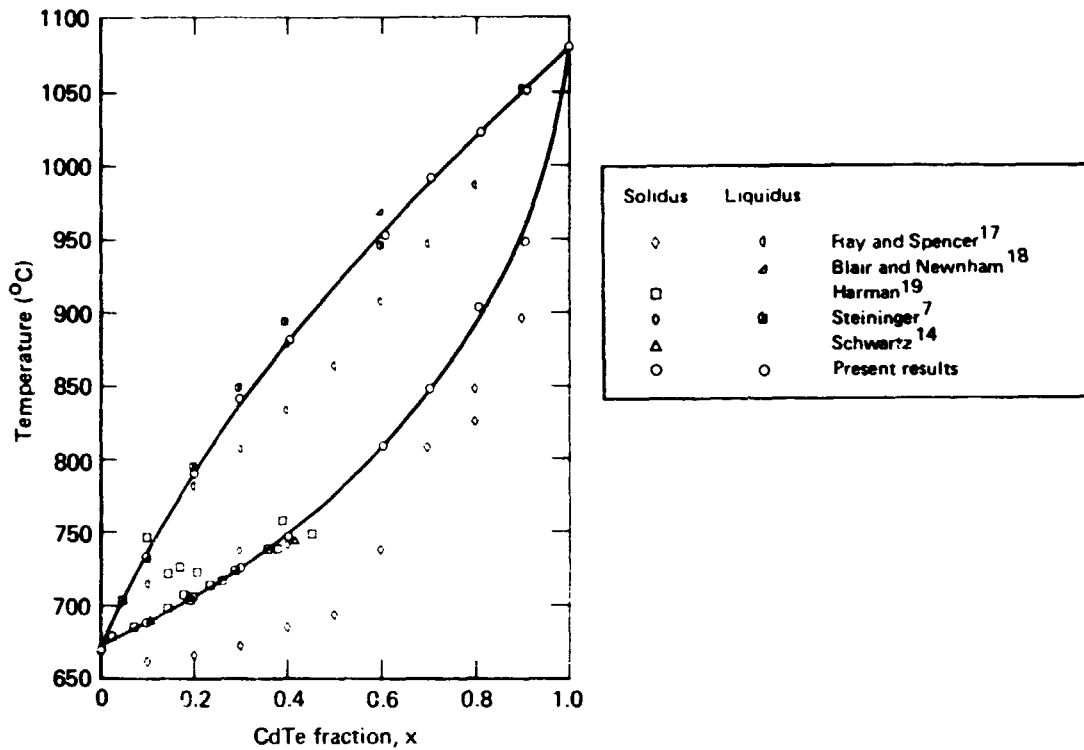


Figure 9. Comparison of present phase-equilibria data with previous results.

For most compositions, the solidus and liquidus temperatures determined by this investigation are much larger than those reported by Ray and Spencer.¹⁷ A possible explanation for the discrepancies is advanced in Reference 20.

2.5 Liquid-Solid Equilibrium Parameters

The equilibria temperatures in Table 5 were used to calculate the temperature and composition dependence of the liquid/solid interface distribution coefficient, $k(T) = x^S(T)/x^L(T)$, where x^S and x^L are the solidus and liquidus compositions, respectively. To facilitate the calculations, analytical expressions were developed for $x^S(T)/x^L(T)$. Reasonably good fits to the phase diagram data were given by the following functional forms:

$$x^S(T) = C_1 \sin\left(\frac{\pi}{2} T^*\right) + C_2 \sin\left(\frac{\pi}{2} T^{*1/2}\right) + C_3 \log_{10} \left(\frac{9T - 5618^\circ\text{C}}{412^\circ\text{C}} \right) + C_4 T^{*1/2} \quad (15)$$

and

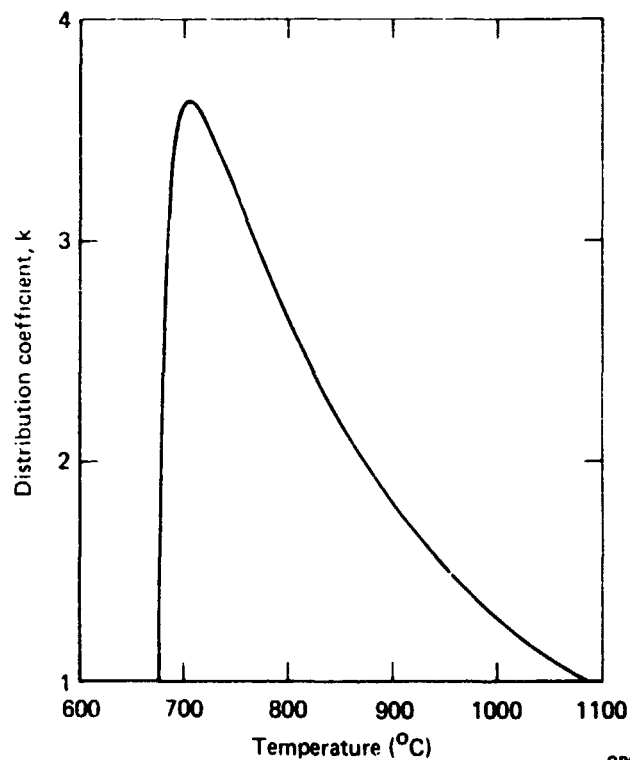
$$x^L(T) = D_1 T^* + D_2 T^{*2} + D_3 T^{*3} + D_4 T^{*4}, \quad (11)$$

where $T^* = (T - 670^\circ\text{C})/412^\circ\text{C}$ and the C_i and D_i are fitting constants. The values of the constants giving the best fits are given in Table 7. The solid curves drawn in Figures 8 and 9 are plots of Equations (10) and (11). The calculated values of $k(T)$ as functions of temperature and $x^S(T)$ are shown, respectively, in Figures 10 and 11. The failure of $k(T)$ to go through the point $(T, k) = (670^\circ\text{C}, 1)$ or the point $(x^S, k) = (0, 1)$ is an artifact of the solidus fit shown in Figure 8.

TABLE 7. BEST VALUES FOR THE FITTING CONSTANTS C_i AND D_i .

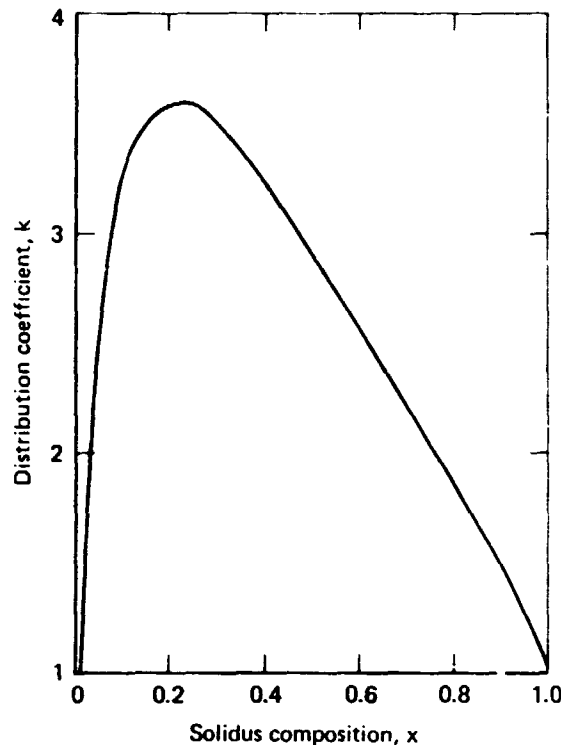
i	C_i	D_i
1	0.380857	0.607640
2	0.086277	0.077209
3	1.200139	0.696167
4	-0.665231	-0.381683

GP03-0750-8



GP03-0750-20

Figure 10. Temperature dependence of the interfacial distribution coefficient.



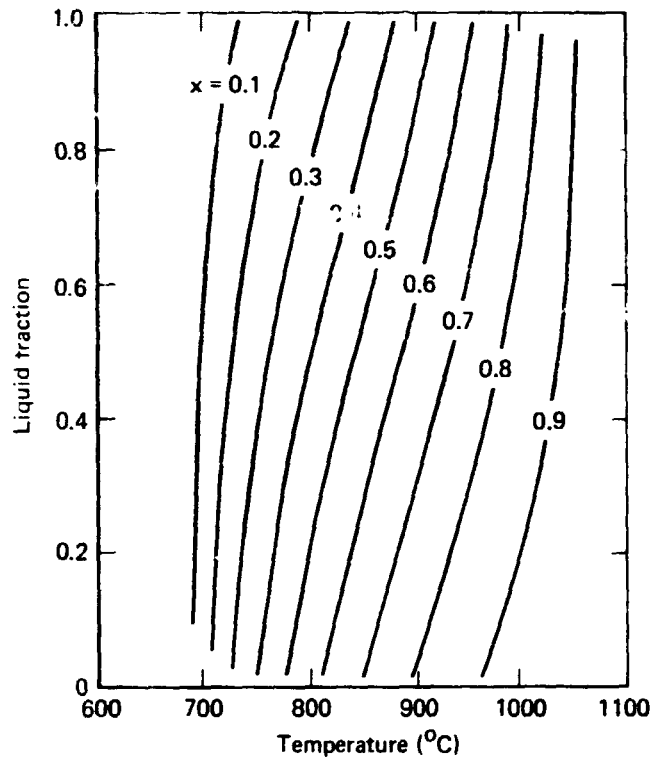
GP03-0750-21

Figure 11. Composition dependence of the distribution coefficient.

To compare the observed DTA signals with those expected from the alloy properties, the equilibrium liquid fraction, $M_L(T)$, was determined by using the lever rule, $M_L(T) = [x^S(T) - x_0] / [x^S(T) - x^L(T)]$, and the analytical expressions of Equations (10) and (11) for x^S and x^L . The temperature and composition dependences of $M_L(T)$ are shown in Figure 12, and their temperature derivatives are shown in Figure 13. Figure 14 shows the observed normalized DTA signals for the various alloy compositions. A comparison of the results shown in Figure 14 with the results in Figure 13 shows a one-to-one correlation between the relative magnitudes of the DTA signals and the variation of dM_L/dT with composition. In principle, if the heat transfer characteristics of the furnace/sample system are well known, the compositional and temperature variations of dM_L/dT and thus $M_L(x^S, x^L, x_0)$ can be calculated from the measured thermal arrest curves and vice versa. Approximate heat transfer calculations were performed, and in general, the calculated and observed DTA curves for the various alloy compositions were comparable. However, the detailed features of the calculated curves were sensitive to

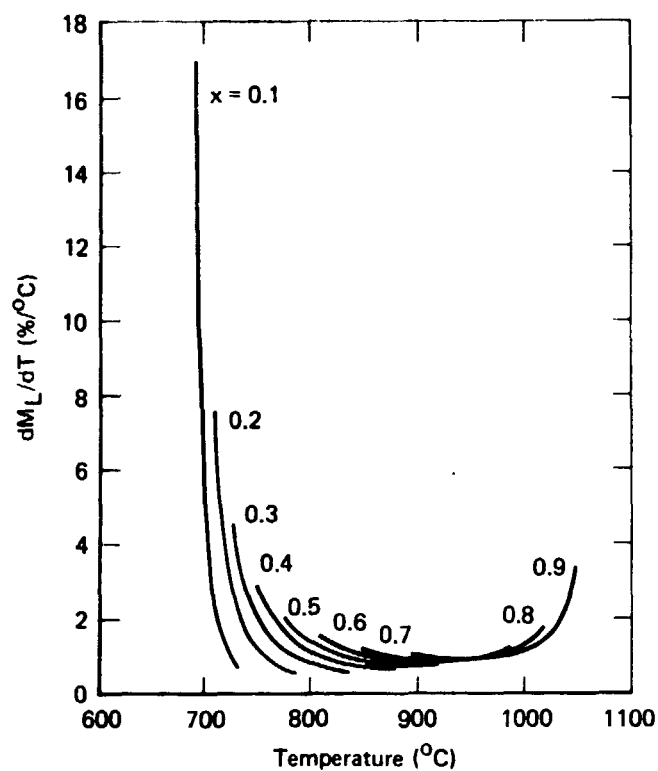
ORIGINAL PAGE IS
OF POOR QUALITY

small variations in the values of the heat transfer parameters, some of which are not precisely known. Meaningful deconvolutions of the measured DTA curves would require a precise thermal model for the sample/furnace system.



GP03-0750-22

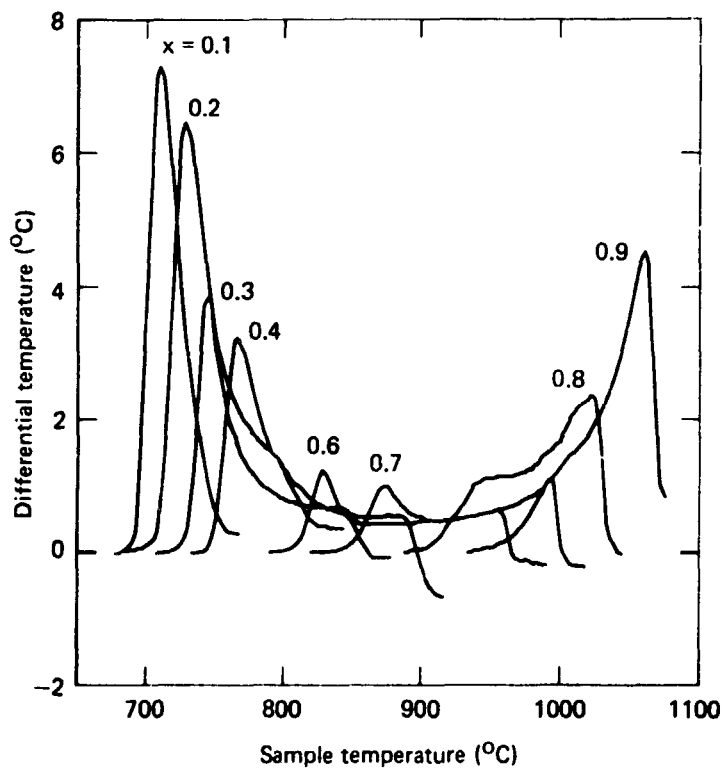
Figure 12. Temperature dependence of the alloy liquid fraction for various alloy compositions.



ORIGINAL PAGE IS
OF POOR QUALITY

GP03-0750-23

Figure 13. The temperature dependence of the rate of change with respect to temperature of the alloy liquid fraction for various alloy compositions.



GP03-0750-24

Figure 14. Compositional variation of the observed DTA signals as functions of sample temperature.

3. PHASE EQUILIBRIA CALCULATIONS

Iterative phase-equilibria calculations, based on the regular associated solution (R.A.S.) theory^{1,2} were performed, and a set of R.A.S. parameters was obtained by simultaneously least-squares-fitting the binary³⁻⁶ and pseudobinary phase diagrams. Using the set of R.A.S. parameters, the activities and partial pressures of Hg, Cd, and Te vapor over pseudobinary melts were calculated.

3.1 Theoretical Model

The term, regular solution, was used by Hildebrand²¹ to describe mixtures whose behavior was found experimentally to have certain regularities, and the definition of the term is essentially empirical. Subsequently, Guggenheim²² used the term to describe any mixture of molecules for which the entropy is that of an ideal solution but for which the interchange energy is not zero. The interchange energy is related to the nearest-neighbor pairwise interaction energies between atoms. Subsequently, Jordan¹ considered the consequences of the association of type A and type B atoms in the liquid, i.e., the existence of AB species, and developed a thermodynamic description for such liquid solutions. He termed his formulation the regular associated solution (R.A.S.) theory. We assumed that the binary alloys $\text{Hg}_{1-x}\text{Te}_x$ and $\text{Cd}_{1-x}\text{Te}_x$, and hence the ternary Hg-Cd-Te alloys, are regular associated solutions, and used Jordan's formalism, as extended to ternary alloy systems by Szapiro,² to determine the pertinent thermodynamic phase-equilibria parameters for the alloy system.

In the context of the R.A.S. theory, the liquidus and solidus ternary equations for an ABC ternary system are given by²:

$$[1 - y] \exp \left[\frac{W}{RT} y^2 \right] = \frac{x_{AC}}{x_{AC}^*} \times \exp \left[\frac{\Delta H_1 + \omega x_2(1 - 2x_1) + (\alpha_1 x_1 + \alpha_2 x_2 - 0.5\alpha_1)(1 - 2x_3)}{RT} - \frac{\Delta S_1}{R} \right], \quad (12)$$

and

$$y \exp \left[\frac{W}{RT} (1 - y^2) \right] = \frac{x_{BC}}{x_{BC}^*} \times \exp \left[\frac{\Delta H_2 + \omega x_1 (1 - 2x_2) + (\alpha_1 x_1 + \alpha_2 x_2 - 0.5\alpha_2) (1 - 2x_3)}{RT} - \frac{\Delta S_2}{R} \right], \quad (13)$$

where:

- y = mole fraction of complex BC in the solid phase,
 - x_1, x_2, x_3 = atom fractions of A, B, and C, respectively,
 - x_{AC}, x_{BC} = mole fractions of AC and BC in the liquid phase,
 - T = absolute temperature,
 - $\Delta S_1, \Delta S_2$ = entropies of fusion of the binary systems AC and BC,
 - $\Delta H_1, \Delta H_2$ = heats of fusion of the binary systems AC and BC,
 - R = the universal gas constant,
 - α_1 = the interaction parameter for the liquid binary system AC,
 - α_2 = the interaction parameter for the liquid binary system BC,
 - ω = the interaction parameter between species A and B,
- and
- W = the interaction parameter between species AC and BC in the solid.

Asterisks denote the standard states of the liquid phases (stoichiometric compositions in the binary systems AC and BC). The interaction parameters $\alpha_1, \alpha_2, \omega$, and W are related to the interchange energies for the various pairwise interactions.

For the $A_{1-x}C_x$ binary case, $y = 0$, $x_2 = 0$, and $x_1 + x_3 = 1$. Letting $x = x_3$, Equation (12) for this case reduces to

$$\exp \left[\frac{\Delta H_1 + 2\alpha (x - 0.5)^2}{RT} \right] = \frac{x_{AC}^*}{x_{AC}} \exp \left(\frac{\Delta S_1}{R} \right) \quad (14)$$

where

$$x_{AC} = \frac{1 - [1 - 4(1 - x)x/(1 + \kappa)]^{1/2}}{1 + [1 - 4(1 - x)x/(1 + \kappa)]^{1/2}}, \quad (15)$$

$$x_{AC}^* = x_{AC} \quad (x = 0.5), \quad (16)$$

and κ is given in terms of the temperature-independent equilibrium constant, K , by

$$\kappa = K \exp \left(\frac{-\alpha}{2RT} \right) - \left(\frac{\beta^2}{1 - \beta^2} \right). \quad (17)$$

The parameter β is defined by Equation (17) and is a measure of the degree of association in the liquid. For a completely associated solution, $\kappa = 0$, and thus $\beta = 0$. When the solution is completely dissociated, $\kappa = \infty$ and $\beta = 1$. The activities of the species a_A and a_C for the binary melt are given by

$$a_A = x_A \gamma_A = x_A \exp \left[\frac{x_A^2 \alpha}{RT} \right] \quad (18)$$

and

$$a_C = x_C \gamma_C = x_C \exp \left[\frac{(1 - x)^2 \alpha}{RT} \right], \quad (19)$$

where γ_A and γ_C are the activity coefficients,

$$x_A = x_1 [1 + x_{AC}] - x_{AC}, \quad (20)$$

and

$$x_C = x_3 [1 + x_{AC}] - x_{AC}. \quad (21)$$

For the pseudobinary cut, $x_3 = 0.5 = x_1 + x_2$, so that Equations (12) and (13) become

$$(1 - y) \exp \left[\frac{W}{RT} y^2 \right] = \frac{x_{AC}}{x_{AC}^*} \exp \left[\frac{\Delta H_1 + \omega x_2 (1 - 2x_1)}{RT} - \frac{\Delta S_1}{R} \right] \quad (22)$$

ORIGINAL PAGE IS
OF POOR QUALITY

and

$$y \exp \left[\frac{W}{RT} (1 - y)^2 \right] = \frac{x_{BC}}{x_{BC}^*} \exp \left[\frac{\Delta H_2 + \omega x_1 (1 - 2x_2)}{RT} - \frac{\Delta S_2}{R} \right], \quad (23)$$

where

$$x_{AC} = \frac{x_1 x_C (1 + \sigma)}{\kappa_1 + x_C}, \quad (24)$$

$$x_{BC} = \frac{x_2 x_C (1 + \sigma)}{\kappa_2 + x_C}, \quad (25)$$

and $\sigma (\equiv x_{AC} + x_{BC})$ is the solution of the cubic equation

$$\frac{x_1}{\kappa_1 + 0.5 (1 - \sigma)} + \frac{x_2}{\kappa_2 + 0.5 (1 - \sigma)} = \frac{\sigma}{0.5 (1 - \sigma^2)}. \quad (26)$$

The parameters $\kappa_1(AC)$ and $\kappa_2(BC)$ are defined by Equation (17), and the parameters x_{iC}^* ($i = A, B$) are defined by Equation (16).

The activities a_A , a_B , and a_C for the pseudobinary melt are given by the expressions:

$$a_A = x_A \gamma_A = [x_1 (1 + x_{AC} + x_{BC}) - x_{AC}] \gamma_A, \quad (27)$$

$$a_B = x_B \gamma_B = [x_2 (1 + x_{AC} + x_{BC}) - x_{BC}] \gamma_B, \quad (28)$$

and

$$a_C = x_C \gamma_C = 0.5 [1 - x_{AC} - x_{BC}] \gamma_C, \quad (29)$$

where γ_A , γ_B , and γ_C are the activity coefficients given by

$$\gamma_A = \exp \left[\frac{\omega x_2^2 + 0.25 \alpha_1 + (\omega + \alpha_1 - \alpha_2) (0.5 x_2)}{RT} \right], \quad (30)$$

$$\gamma_B = \exp \left[\frac{\omega x_1^2 + 0.25 \alpha_2 + (\omega - \alpha_1 + \alpha_2) (0.5 x_1)}{RT} \right], \quad (31)$$

and

$$\gamma_C = \exp \left[\frac{\alpha_1 x_1^2 + \alpha_2 x_2^2 + (\alpha_1 + \alpha_2 - \omega) x_1 x_2}{RT} \right]. \quad (32)$$

3.2 Regular Associated Solution Parameters for the HgCdTe Alloy System

The R.A.S. parameters α_1 , α_2 , κ_1 , κ_2 , ω , and W for the HgCdTe alloy system were determined by simultaneously least-squares-fitting the metal-rich segments of the binary liquidus curves³⁻⁶ and the pseudobinary (Figure 8) phase diagram. To facilitate the computations, Equations (22) and (23) were rewritten in the following forms:

$$T = \frac{\Delta H_1 + \omega x_2 (1 - 2x_1) - W y^2}{R \left[\ln(1 - y) - \ln \frac{x_{AC}}{x_{AC}^*} \right] + \Delta S_1} = T_2 \quad (33)$$

and

$$T = \frac{\Delta H_2 + \omega x_1 (1 - 2x_2) - W (1 - y)^2}{R \left[\ln y - \ln \frac{x_{BC}}{x_{BC}^*} \right] + \Delta S_2} = T_3. \quad (34)$$

These equations and Equation (14) were then fitted to the experimental data to obtain the best values of the parameters by minimizing the sum:

$$S = \sum_i \left[\left(T_{1(c)}^{\text{CdTe}} - T_{1(e)}^{\text{CdTe}} \right)^2 + \left(T_{1(c)}^{\text{HgTe}} - T_{1(e)}^{\text{HgTe}} \right)^2 + \left(T_{3i}^{\text{HgCdTe}} - T_{1(e)}^{\text{HgCdTe}} \right)^2 + \left(T_{2i}^{\text{HgCdTe}} - T_{1(e)}^{\text{HgCdTe}} \right)^2 \right]. \quad (35)$$

The symbols c and e designate, respectively, the calculated and experimental values.

Table 8 lists the calculated values of the parameters as well as the pertinent thermodynamic quantities used in the calculations. Table 9 indicates the relative accuracy of the fit to the measured pseudobinary data. The calculated mole fractions of the various species and complexes as functions of the solidus temperature are given in Table 10 to illustrate the relative effects of association on the $\text{Hg}_{1-x}\text{Cd}_x\text{Te}$ solutions.

TABLE 8. R.A.S. PARAMETERS AND THERMODYNAMIC DATA FOR THE Hg-Cd-Te SYSTEM.

R.A.S. parameters	Thermodynamic data
$K_1 = 0.9716$	$\Delta S_1 = 9.2 \text{ e.u.} = 38.5 \text{ J/mol K}^{(a)}$
$\alpha_1 = 953.0 \text{ cal/mol} = 3.987 \text{ kJ/mol}$	$\Delta S_2 = 8.9 \text{ e.u.} = 37.2 \text{ J/mol K}^{(a)}$
$K_2 = 0.1201$	$\Delta H_1 = 8675.6 \text{ cal/mol} = 36.299 \text{ kJ/mol}$
$\alpha_2 = 9051 \text{ cal/mol} = 37.87 \text{ kJ/mol}$	$\Delta H_2 = 12012 \text{ cal/mol} = 50.258 \text{ kJ/mol}$
$\omega = 971.7 \text{ cal/mol} = 4.066 \text{ kJ/mol}$	$T_{f1} = 943 \text{ K}^{(a)}$
$W = 836.0 \text{ cal/mol} = 3.498 \text{ kJ/mol}$	$T_{f2} = 1365 \text{ K}^{(a)}$

(a) A. Laugier, *Revue de Physique Appliquée* **8**, 259 (1973).

GP03-0750-9

(b) The subscript 1 refers to HgTe and the subscript 2 refers to CdTe.

TABLE 9. A COMPARISON OF EXPERIMENTAL
AND CALCULATED TEMPERATURES
FOR $\text{Hg}_{1-x}\text{Cd}_x\text{Te}$.

T_{exp} (K)	T_2^{\dagger} (K)	T_3^{\dagger} (K)
973	968	981
998	991	1003
1023	1012	1026
1048	1032	1052
1073	1053	1074
1098	1074	1098
1123	1097	1122
1148	1121	1145
1173	1149	1168
1198	1180	1192
1223	1213	1217
1248	1254	1242
1273	1298	1268
1298	1358	1294

The quantities designated by \dagger were calculated using Equations (33) and (34); the parameters are given in Table 8.

GP03-0750-10

TABLE 10. MOLE FRACTIONS OF SPECIES IN LIQUID
PHASE AS FUNCTIONS OF LIQUIDUS
TEMPERATURE.

T_L (K)	x_{Hg}	x_{Cd}	x_{Te}	x_{HgTe}	x_{CdTe}
973	0.387	0.001	0.388	0.198	0.026
998	0.379	0.002	0.380	0.189	0.050
1023	0.370	0.003	0.373	0.179	0.075
1048	0.359	0.004	0.363	0.169	0.104
1073	0.348	0.005	0.354	0.158	0.134
1098	0.335	0.007	0.342	0.147	0.169
1123	0.319	0.010	0.329	0.134	0.207
1148	0.302	0.013	0.315	0.120	0.250
1173	0.282	0.017	0.299	0.106	0.296
1198	0.258	0.022	0.281	0.091	0.348
1223	0.231	0.029	0.260	0.075	0.405
1248	0.200	0.038	0.238	0.059	0.465
1273	0.164	0.050	0.214	0.044	0.529
1298	0.121	0.066	0.187	0.028	0.597

GP03-0750-11

3.3 Component Partial Pressures over the Pseudobinary Melt

Following Jordan,²³ the partial pressures of the components over the pseudobinary melt can be related to the activities by the expressions

$$P_{\text{Hg}} = a_{\text{Hg}} P_{\text{Hg}}^{\circ} \quad (36)$$

$$P_{\text{Cd}} = a_{\text{Cd}} P_{\text{Cd}}^{\circ} \quad (37)$$

and

$$P_{\text{Te}_2} = a_{\text{Te}}^2 P_{\text{Te}_2}^{\circ} \quad (38)$$

where P_{Hg}° , P_{Cd}° , and $P_{\text{Te}_2}^{\circ}$ are the vapor pressures over the standard states and the respective activities a_{Hg} , a_{Cd} , and a_{Te} are given by Equations (27-29). Using Equations (36-38) and the parameters of Table 8, the component partial pressures were calculated as functions of the liquidus temperature, and the results are summarized in Table 11 and Figure 15. Figure 16 illustrates the temperature variation of the Hg partial pressure over the pseudobinary melt as a function of the Cd fraction. The calculated Hg partial pressures are in reasonable agreement with Steininger's experimental results.⁷ However, the validity of the calculated R.A.S. parameter values and thus the calculated partial pressures are sensitively dependent upon assumptions concerning the melt composition. For example, the derivation of Equations (12) and (13) assumes negligible Hg-Hg, Cd-Cd, and Te-Te associations in the melt. The validity of at least the last of the assumptions is highly suspect.

TABLE 11. CALCULATED COMPONENT PARTIAL PRESSURES OVER THE
 $\text{Hg}_{1-x}\text{Cd}_x\text{Te}$ MELT AT THE LIQUIDUS TEMPERATURE.

T_L (K)	Composition (x)	a_{Hg}	a_{Cd}	a_{Te}	P_{Hg}^0 (a) (atm)	P_{Cd}^0 (b) (atm)	$P_{\text{Te}_2}^0$ (c) (atm)	P_{Hg} (atm)	P_{Cd} (atm)	P_{Te_2} (atm)
973.2	0.044	0.421	0.009	0.457	50.6	0.457	0.039	21.3 (17.5)	0.004	0.008
998.2	0.084	0.396	0.016	0.463	60.8	0.626	0.056	24.1 (21.0)	0.010	0.012
1023.2	0.124	0.374	0.023	0.468	72.5	0.844	0.078	27.1 (25.0)	0.020	0.017
1048.2	0.170	0.350	0.031	0.473	85.6	1.120	0.108	29.9 (29.5)	0.035	0.024
1073.2	0.215	0.327	0.039	0.476	100.0	1.470	0.146	32.8 (34.5)	0.057	0.033
1098.2	0.268	0.302	0.048	0.479	117.0	1.910	0.196	35.3 (40.4)	0.091	0.045
1123.2	0.324	0.278	0.057	0.480	135.0	2.440	0.259	37.5 (47.0)	0.140	0.061
1148.2	0.384	0.252	0.068	0.479	155.0	3.090	0.338	39.1 (53.5)	0.210	0.078
1173.2	0.446	0.227	0.080	0.475	177.0	3.880	0.436	40.1 (61.0)	0.309	0.098
1198.2	0.514	0.200	0.094	0.468	201.0	4.820	0.556	40.2 (69.0)	0.451	0.122
1223.2	0.586	0.172	0.110	0.456	227.0	5.930	0.703	39.0 (77.0)	0.654	0.146
1248.2	0.660	0.143	0.130	0.439	255.0	7.250	0.880	36.5	0.943	0.170
1273.2	0.736	0.113	0.155	0.415	286.0	8.780	1.090	32.3	1.360	0.188
1298.2	0.816	0.081	0.188	0.385	318.0	10.600	1.340	25.7	1.980	0.199

Values in parentheses correspond to Steininger's experimental results (Ref. 7).

P_{Hg}^0 , P_{Cd}^0 and $P_{\text{Te}_2}^0$ represent the vapor pressures over the elemental melts.

(a) P_{Hg}^0 was obtained from the equation, $\log_{10} P_{\text{Hg}}^0 \text{ (atm)} = 4.891 - \frac{3080}{T(K)}$, which gives P_{Hg}^0 with an accuracy of better than 1% [S. Sugawara et al., Bull. Jap. Soc. Mech. Eng. 5, 711 (1962)].

(b) P_{Cd}^0 was obtained from the equation, $\log_{10} P_{\text{Cd}}^0 \text{ (atm)} = 5.106 - \frac{5300}{T(K)}$, which gives P_{Cd}^0 with an accuracy of better than 0.5% [D.R. Stull and G.E. Sinke, Thermodynamic Properties of the Elements, (Am. Chem. Soc., Washington, D.C. 1956)].

(c) $P_{\text{Te}_2}^0$ was obtained from the equation, $\log_{10} P_{\text{Te}_2}^0 \text{ (atm)} = 4.7191 - \frac{5960.2}{T(K)}$ [An. N. Nesmeyanov, Vapor Pressure of the Elements (Academic Press, New York, 1963)].

GP03-0750-12

(+)

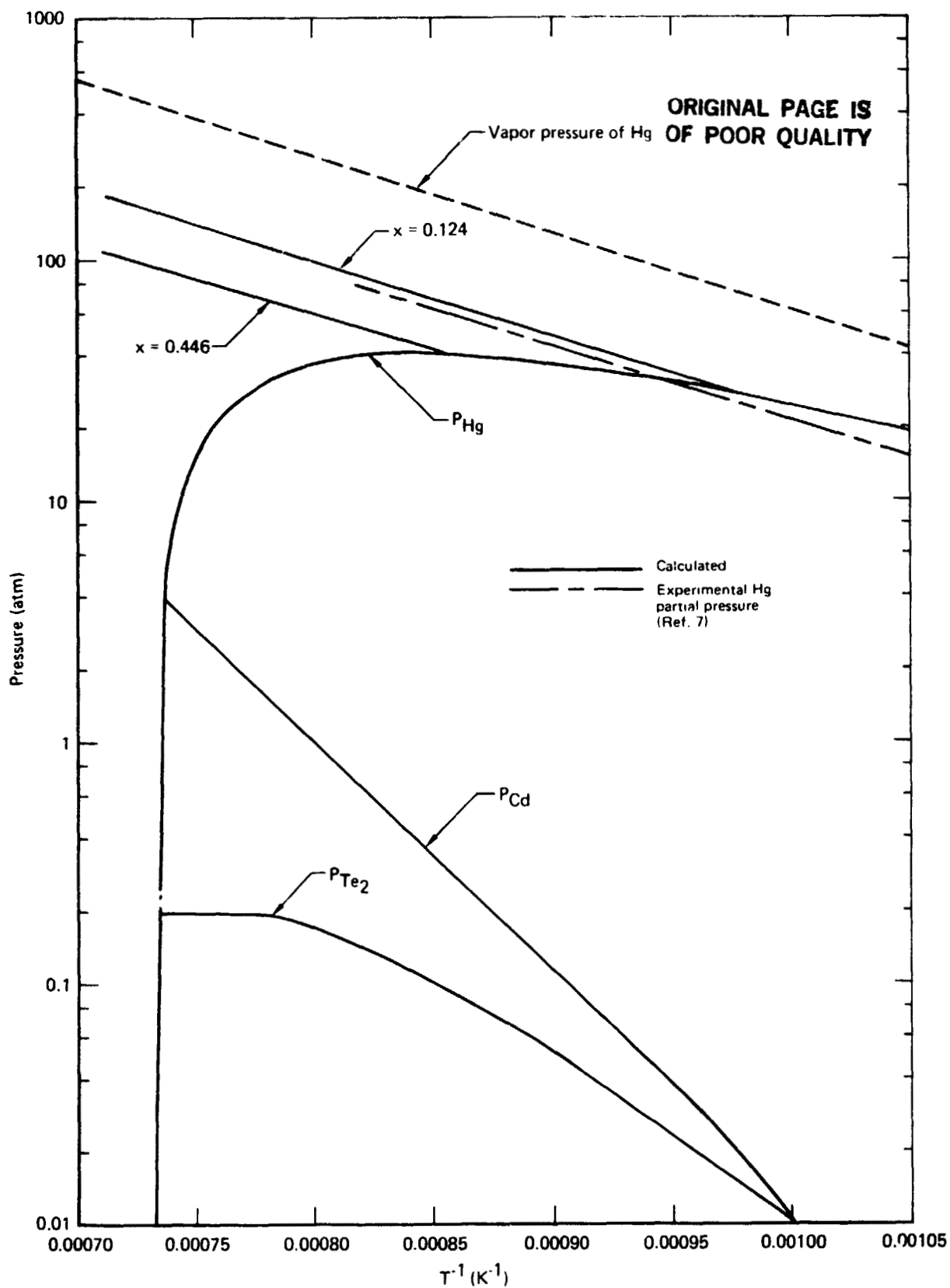
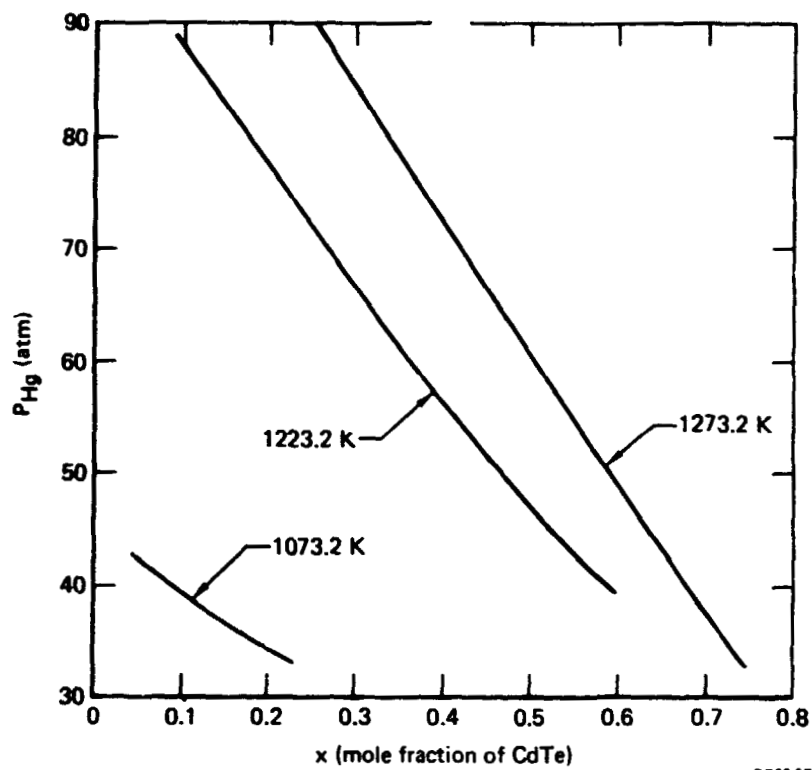


Figure 15. Component partial pressures over the $\text{Hg}_{1-x}\text{Cd}_x\text{Te}$ melt.

ORIGINAL PAGE IS
OF POOR QUALITY



GP63-0750-2

Figure 16. The temperature variation of Hg partial pressure over the $\text{Hg}_{1-x}\text{Cd}_x\text{Te}$ melt as a function of Cd fraction.

4. HIGH-TEMPERATURE-GRADIENT DIRECTIONAL SOLIDIFICATION

4.1 Alloy Preparation

$\text{Hg}_{0.8}\text{Cd}_{0.2}\text{Te}$ alloys were prepared by reacting 99.9999% pure elemental constituents in sealed, evacuated, fused-quartz tubing. The tubing dimensions were 5-mm i.d. x 10-mm o.d. To prepare an ampule, the end of the tubing where solidification was to begin was tapered to a point to enhance the probability of single-crystal growth. For the initial experiments, a 5-mm i.d. x 10-mm o.d. quartz tube was fused to the tapered end of the ampule to serve as a coupling sleeve to a 5-mm diam quartz-rod pedestal, which supported the ampule during the growth process. This coupling arrangement was susceptible to mechanical failure, and after several failures, a configuration was used in which a 4-mm diameter silica rod is fused directly to the tapered end of the ampule. The solid silica rod inserts into a 5-mm i.d. silica tube, which serves as a pedestal.

Following fabrication, the ampules were cleaned thoroughly, with the final cleaning being done with a dilute HF solution, evacuated, and baked at 1150°C. The ampules were loaded with precisely weighed amounts of Hg, Cd, and Te. Following loading, the ampules were sealed and the alloys were cast as described in Section 2.1.

Altogether, 12 crystal-growth ampules (L1-L12) containing alloys with $x = 0.2$ were prepared. The ampules L1-L5 contained stoichiometric proportions of the constituent elements. The alloy preparations yielded highly p-type ingots because of the Te excess in the melt caused by the preferential Hg evaporation into the ampule free volume. For ampules L6-L12, excess mercury was added to compensate for the preferential mercury evaporation. Ampules L1, L2, and L8 failed during casting. Ampules L9, L10, and L11 showed wetting of the ampule wall by the alloy, and they were discarded.

4.2 Experimental Arrangement and Procedures for Unidirectional Crystal Growth

The precast alloys were regrown by unidirectional solidification in the growth apparatus illustrated in Figure 17. The ampule is mounted, with its tapered end down, atop a quartz pedestal and remains stationary during the growth process. Two resistively heated, tubular furnaces provide for the

ORIGINAL PAGE IS
OF POOR QUALITY

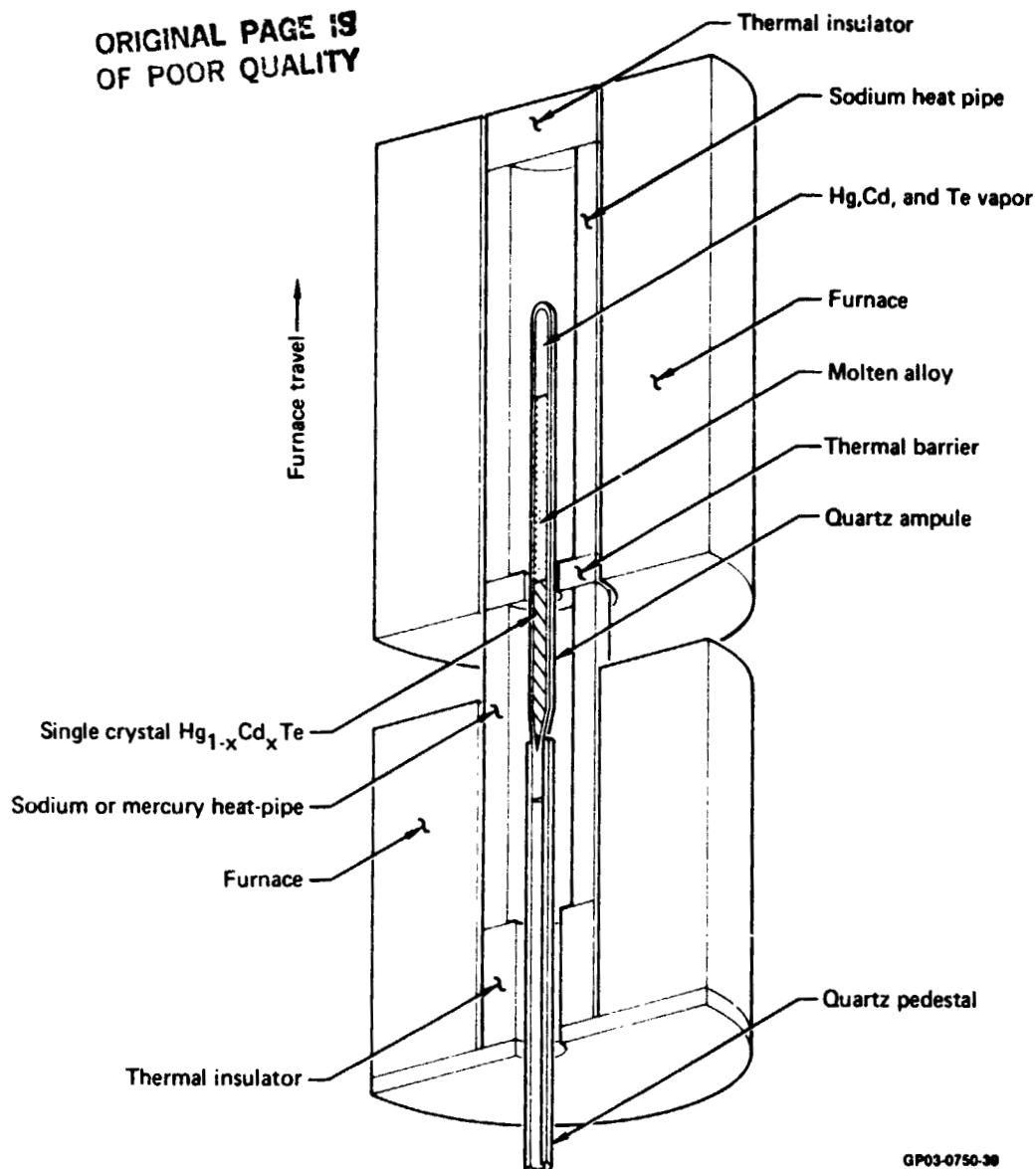


Figure 17. Bridgman crystal-growth furnace assembly.

temperature control of the hot and cold zones. The furnace assembly travels upward on vertical ways so that the crystal grows progressively upward from the bottom, tapered end of the ampule. Each furnace is provided with a heat-pipe isothermal furnace liner to provide two well-defined heated zones. The hot-zone heat-pipe is sodium-charged, and the cold-zone heat-pipe is either sodium or mercury charged depending on the temperature requirements. The heat-pipes are separated by a heat barrier. Besides providing the necessary thermal isolation between the heated zones, the barrier also provides a semi-

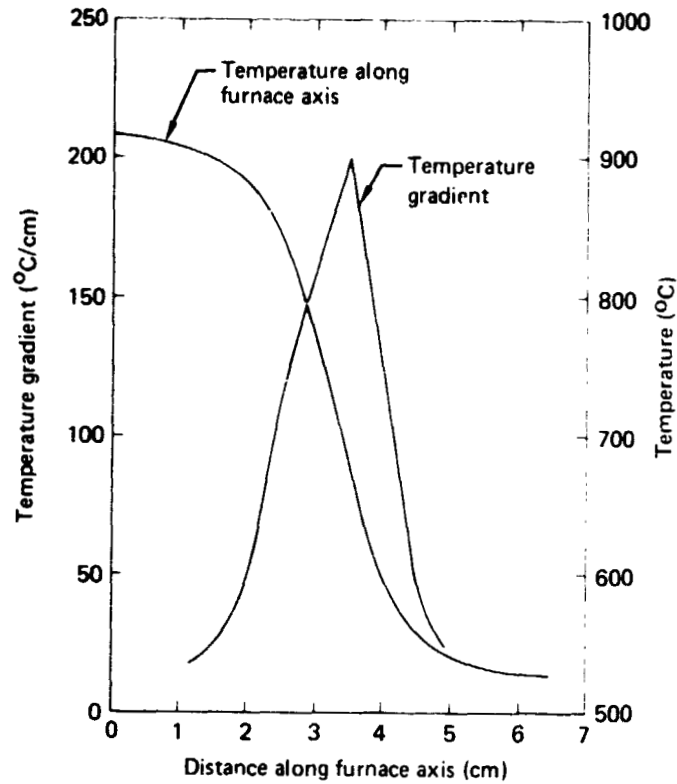
adiabatic region. The barrier consists of 4-mm thick zirconia-felt or various thicknesses of fire-brick disks sandwiched between two 25- μ m thick polished platinum foils on the hot side and two 25- μ m aluminum foils on the cold side. The diameter of the circular opening in the heat barrier is 12-mm to accept 10-mm diameter ampules.

Prior to a given growth run, a dummy ampule with an attached thermocouple is placed in the upper zone of the furnace, and the two heated-zone temperatures are raised to their desired values. The furnace assembly is translated upward, and the thermocouple output is recorded as a function of furnace position to establish the temperature variation along the furnace assembly axis. The furnaces are then cooled to ambient temperature, the growth ampule is positioned in the upper zone, and the zone temperatures are increased to the previous values. Prior to growth initiation, the molten alloy is maintained at temperature for 24 h to assure melt homogenization.

4.3 Bridgman Crystal Growth Runs

Crystal growth runs were completed for ampules L3, L4, L5, L6, and L7 at furnace translation rates of 0.597, 1.12, 5.62, 0.310, and 0.068 μ m/s, respectively. The longitudinal temperature profiles in the furnace at the initiation of growth of ingots L3 and L4 are shown in Figures 18 and 19, respectively, and the furnace profile for ingots L6 and L7 is shown in Figure 20.

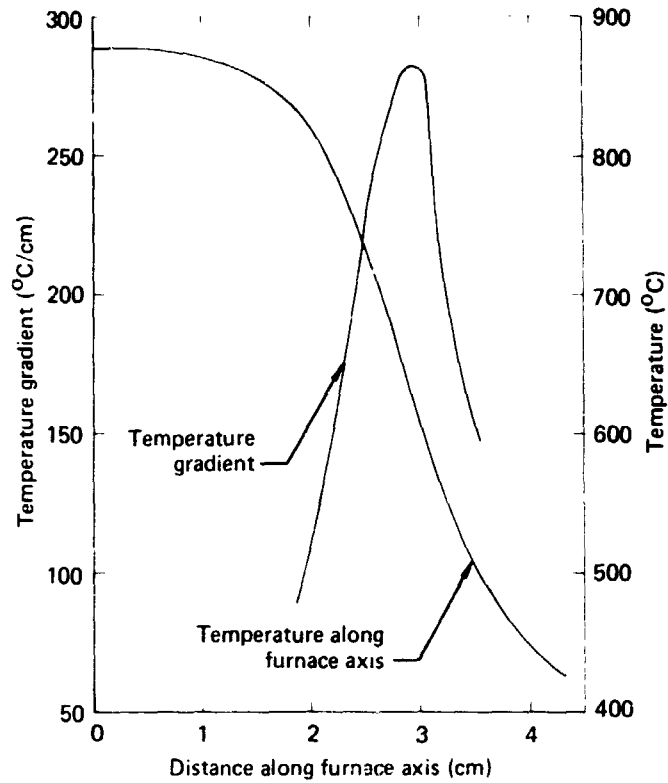
The recrystallized ingots were removed from the ampules by dissolving the quartz in concentrated HF. Sample L5 showed excessive wetting between the ampule and the ingot and was not evaluated further. The remaining ingots were sliced into wafers by a wire saw for characterization.



GP03-0750-40

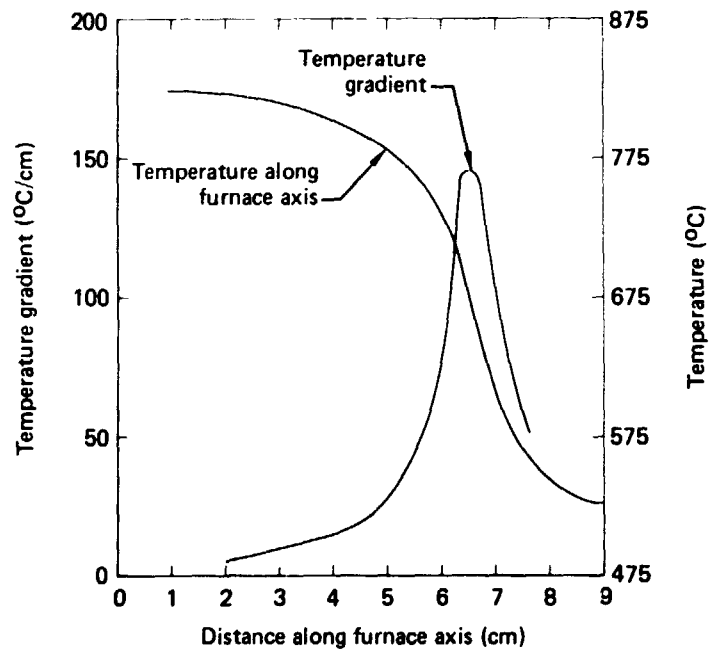
Figure 18. Temperature profile of crystal-growth furnace during growth of ingot L3.

ORIGINAL PAGE IS
OF POOR QUALITY



GP03-0750-41

Figure 19. Temperature profile of crystal-growth furnace during growth of ingot L4.



GP03-0750-42

Figure 20. Temperature profile of crystal-growth furnace during growth of ingots L6 and L7.

4.4 Ingot Characterization

4.4.1 Determination of Alloy Composition by Mass Density Measurements

The crystal lattice spacing of the $\text{Hg}_{1-x}\text{Cd}_x\text{Te}$ alloys varies so little with x that its measurement cannot be used readily to calculate precise values for the compositions of specimens. For this study, the average x -values of slices transverse to the growth axis were calculated from the measured mass densities and values of the crystal lattice constant published by Woolley and Ray.²⁴

The lattice constant data of Woolley and Ray can be represented by the cubic equation

$$a_0 = 0.646153 + (0.73671 x + 1.90501 x^2 - 0.69347 x^3)/1000, \quad (39)$$

where a_0 is the cubic lattice constant in nanometers and x is the mole fraction of CdTe in the $\text{Hg}_{1-x}\text{Cd}_x\text{Te}$ alloy. There are, on the average, $4x$ Cd atoms, $4(1-x)$ Hg atoms, and 4 Te atoms in each cubic unit cell. Thus, the lattice constant is related to the mass density, ρ_m , by the expression

$$a_0 = \{ [4x M_{\text{Cd}} + 4(1-x) M_{\text{Hg}} + 4 M_{\text{Te}}] / \rho_m \}^{1/3}, \quad (40)$$

where M_{Cd} , M_{Hg} , and M_{Te} are the atomic masses of Cd, Hg, and Te, respectively. For a given density, the value of x can be determined by simultaneously solving Equations (39) and (40).

The mass density of a specimen was determined by obtaining its weight, W_a , in air and its weight, W_w , when it is immersed in water. The specimen density is given by the relation

$$\rho_m = \frac{W_a \rho_w - W_w \rho_a}{W_a - W_w}, \quad (41)$$

where ρ_w is the mass density of water and ρ_a is the mass density of air.

Near $x = 0.2$, an uncertainty of 0.0022 g/cm^3 in ρ_m leads to an uncertainty of about 0.001 in calculating x . The uncertainty in ρ_m can be approximated by

$$\Delta \rho_m = \frac{(\rho_m + \rho_w) \Delta W_a + \rho_m \Delta W_w + W_a \Delta \rho_w}{W_a - W_w}, \quad (42)$$

where ΔW_a , ΔW_w , and $\Delta \rho_w$ are the uncertainties in W_a , W_w , and ρ_w , respectively. Because ΔW_a and $\Delta \rho_w$ are usually much smaller than ΔW_w ,

$$\Delta \rho_m \approx \frac{\rho_m \Delta W_w}{W_a - W_w} \approx \frac{\rho_m^2 \Delta W_w}{W_a \rho_w} \approx \frac{\rho_m^2 \Delta W_w}{W_a}. \quad (43)$$

The uncertainty in x , Δx , is thus given by

$$\Delta x \approx \frac{\Delta W_w \rho_m^2}{2.2 W_a}, \quad (44)$$

where the density is in the units of g/cm^3 . For specimens that weigh about 0.5 g, ΔW_w must be less than 0.00002 g to give x to within ± 0.001 .

The method described by Bowman and Schooner²⁵ was used for the mass density determinations. The $\text{Hg}_{1-x}\text{Cd}_x\text{Te}$ specimen is immersed in water, and the water is boiled briefly to eliminate gases dissolved in the water and to rid the specimen of minute air bubbles that may be sorbed. After the sample and the water have cooled to room temperature, the weight of the immersed specimen is measured with a balance that weighs with a precision of $\pm 0.000001 \text{ g}$. However, the precision of the weight determination in water is much poorer than this because of the surface-tension forces upon the 0.013-mm diam wire that is used to suspend the specimen from the balance arm. Some of the suspension wires that were prepared permitted the weight in water to be determined with an accuracy of $\pm 0.00001 \text{ g}$, but usually an accuracy of only $\pm 0.00002 \text{ g}$ is achieved. To do significantly better requires an inordinate amount of time.

ORIGINAL PAGE IS
OF POOR QUALITY

The following expression, from Reference 25, was used to calculate the density of the water in which the sample is immersed:

$$\rho_w = \left[1 - \frac{(t_w - 3.9863)^2}{508929.2} \frac{t_w + 288.9414}{t_w + 68.12963} \right] \times [0.999973] \left[\frac{1}{1 - C \left(\frac{B}{101325} + \frac{I}{10330} - 1 \right)} \right] \times \left[1 - (2.11 - 0.053t_w) \left(1 - \frac{1}{1 + D} \right) (10^{-6}) \right] \text{ g/cm}^3. \quad (45)$$

In this expression, t_w is the water temperature in $^{\circ}\text{C}$, C is the compressibility of water ($C = 471 \times 10^{-12} \text{ Pa}^{-1}$), B is the barometric pressure in Pa, I is the depth of immersion of the sample in water in mm, and D is the number of days elapsed since the water was boiled. After the measurement in water, the specimen is dried and weighed in air with the same balance. The mass density of air is calculated from the following expression given in Reference 25:

$$\rho_a = \left[\frac{464.56B - H(0.085594t_a^2 - 1.8504t_a + 34.47)}{t_a + 273.16} \times 10^{-6} \right] \text{ g/cm}^3, \quad (46)$$

where H is the relative humidity in percent and t_a is the air temperature in $^{\circ}\text{C}$.

Nichrome (80Ni-20Cr) wire, 0.013 mm in diam, was used to suspend the specimens for the weighings in water. The wires were baked at 700-800 $^{\circ}\text{C}$ for 1 h in air at 0.1 Pa (1×10^{-3} Torr) to prepare their surfaces. The oxidized surfaces of the wires developed microfissures when the wires were cooled. These microfissures cause the water meniscus and surface tension to be nearly the same at each point along the wire when it is raised and lowered in the water during the weighings. No surface film on the water is tolerable, and microscopic dust particles in the meniscus region can invalidate the weight measurements in water.

Tables 12, 13, and 14 summarize the results of mass density measurements for ingots L3, L4, and L6. The distance from the tip given in the tables is the distance to the midplane of a slice.

TABLE 12. AVERAGE ALLOY COMPOSITIONS FOR VARIOUS POSITIONS ALONG THE AXIS OF INGOT L3.

Sample number	Distance from tip (cm)	Mass density (g/cm ³)	Average composition (x)
L31	0.25	7.0319	0.472
L32	0.64	7.2416	0.378
L35	2.07	7.5906	0.221
L310	5.01	7.6312	0.203
L312	6.35	7.6237	0.207
L313	7.27	7.6296	0.204
L314	8.22	7.6285	0.204
L321	12.60	7.6328	0.202
L322	13.32	7.6377	0.200
L327	15.91	7.7200	0.163
L328	16.60	7.8468	0.106

GP03-0750-13

TABLE 13. AVERAGE ALLOY COMPOSITIONS FOR
VARIOUS POSITIONS ALONG THE AXIS
OF INGOT L4.

Sample number	Distance from tip (cm)	Mass density (g/cm ³)	Average composition (x)
L4TIP	0.29	7.1098	0.437
L41A	0.73	7.4947	0.265
L41B	0.81	7.5886	0.222
L41C	1.26	7.6051	0.215
L41D	1.53	7.6144	0.211
L41E	1.79	7.6220	0.207
L41G	2.33	7.6174	0.209
L41I	2.86	7.6176	0.209
L41K	3.39	7.6194	0.208
L42	4.32	7.6252	0.206
L43	5.40	7.6162	0.210
L44	6.43	7.6211	0.208
L45	7.45	7.6334	0.202
L46	8.47	7.6404	0.199
L47	9.49	7.6327	0.202
L48	10.52	7.6320	0.203
L49	11.54	7.6206	0.208
L410	12.32	7.6154	0.210
L411A	13.07	7.6171	0.210
L411B	13.33	7.6263	0.205
L411D	13.87	7.6474	0.196
L411F	14.40	7.6976	0.173
L411G	14.67	7.7458	0.151
L411H	14.93	7.8229	0.117
L411J	15.21	8.0653	0.007

GP03-0750-14

TABLE 14. AVERAGE ALLOY COMPOSITIONS FOR
VARIOUS POSITIONS ALONG THE AXIS
OF INGOT L6.

Sample number	Distance from tip (cm)	Mass density (g/cm ³)	Average composition (x _i)
L6A8	0.80	7.1005	0.442
L6A10	1.00	7.1196	0.433
L6A12	1.20	7.2979	0.353
L6A17	1.65	7.5192	0.254
L6A20	2.00	7.5606	0.235
L6A24	2.40	7.5843	0.224
L6B135	3.50	7.6069	0.214
L6B148	4.85	7.6221	0.207
L6B162	6.25	7.6239	0.206
L6C2	7.75	7.6067	0.214
L6C5	9.25	7.6158	0.210
L6C7	10.25	7.6278	0.205
L6DT122	12.25	7.6247	0.206
L6ET138	13.80	7.6249	0.206
L6ET147	14.75	7.6428	0.198
L6ET157	15.75	7.6802	0.181
L6ET162	16.20	7.7101	0.168
L6FT169	16.90	7.8925	0.085
L6FT172	17.20	7.8985	0.082
L6FT177	17.70	8.0522	0.013

GP03 0750 15

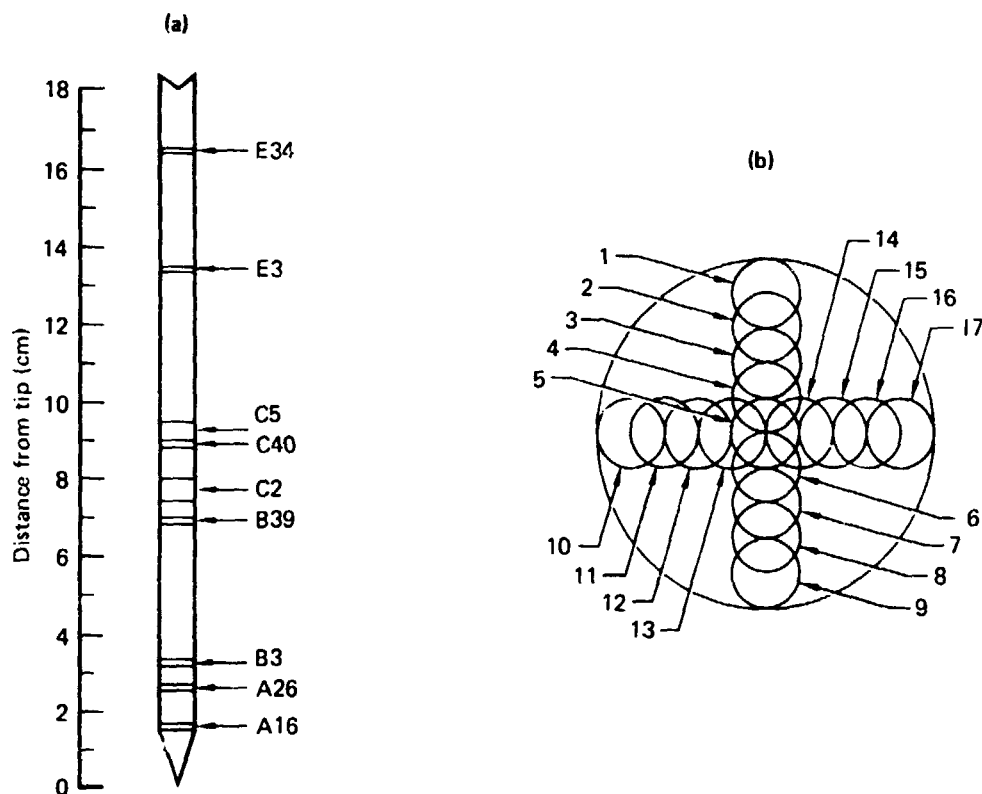
4.4.2 Infrared Transmission Measurements

From ingots L3, L4, and L6, thin (~200-300 μm) slices were prepared for evaluation of the radial compositional variation by infrared transmission-edge mapping. The transmission measurements were made at room temperature through 1-mm diam areas at regularly spaced locations on a slice.

The initial measurements on slices from ingots L3 and L4 showed no infrared (IR) transmission. Subsequently, the thicknesses of these slices were reduced to 20-50 μm by polishing and etching, and the measurements were repeated. However, even for these small thicknesses, the slices remained essentially opaque to IR radiation. This result was attributed to the highly p-type character of the slices.

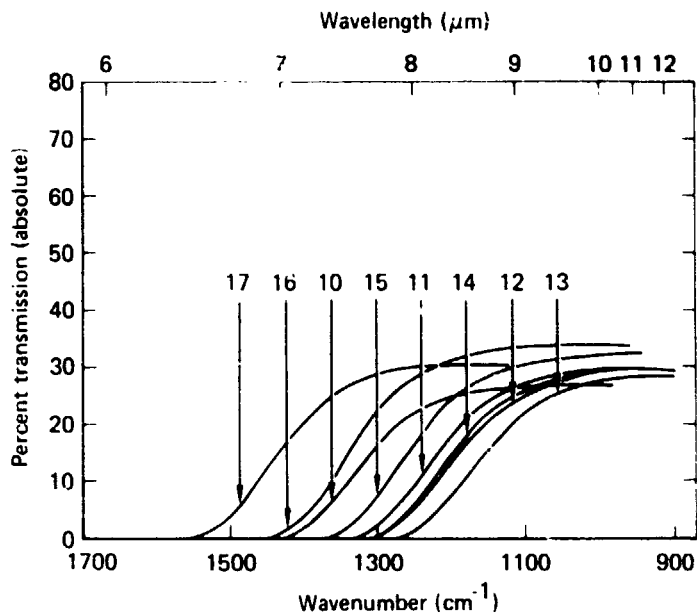
The slices from ingot L6 showed up to 40% transmission above the cut-off wavelengths. The axial positions along the ingot of the slices on which IR measurements were made are shown in Figure 21(a). The radial measurement

positions are shown in Figure 21(b). The diameter of the circles and their positions correspond to the width and relative locations of the incident infrared beam. Typical transmission data for slice A26 are shown in Figure 22. For slices A16, A26, E3, E39, and E34, the radial variation of the cut-on wavelengths and the corresponding alloy compositions are shown in Figure 23. Figure 24 shows the radial variation of the wavelength at 50% transmission. The radial compositional profiles indicate concave solid/liquid interfaces for the entire growth length and thus significant radial temperature gradients in the vicinity of the interface.



GP03-0750-43

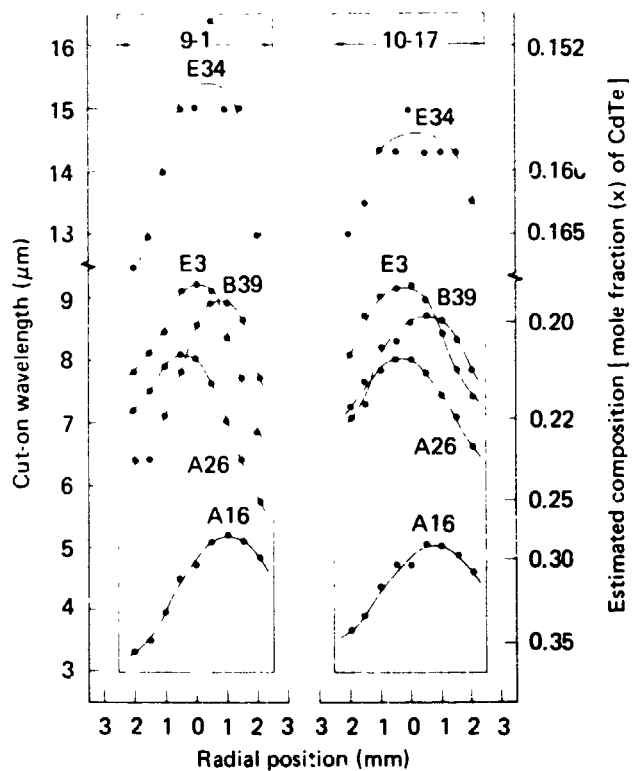
Figure 21. (a) Location of wafers along the growth axis of ingot L6 and (b) the IR measurement positions for a wafer.



ORIGINAL PAGE IS
OF POOR QUALITY

GP03-0750-44

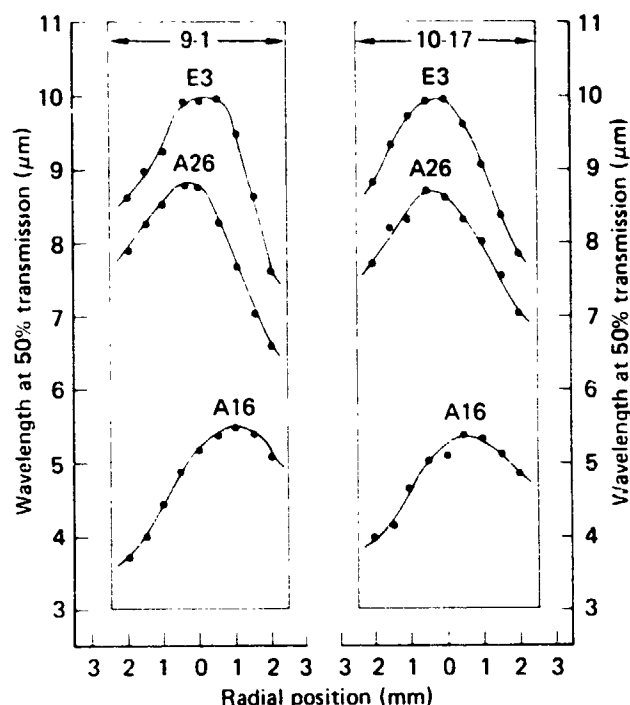
Figure 22. Typical transmission spectra for a wafer (A26) from ingot L6. Numbers of curves refer to locations on wafer as shown in Figure 21.



GP03-0750-45

Figure 23. Radial variations of the cut-on wavelength and Cd composition for ingot L6. Left-side plots are for areas 1 through 9 and right-side plots are for areas 10-13, 5, and 14-17 as shown in Figure 21.

ORIGINAL PAGE IS
OF POOR QUALITY



GP03-0750-46

Figure 24. Radial variation of wavelength at 50% relative transmission across slices from ingot L6. Left-side plots are for areas 1 through 9 and right-side plots are for areas 10-13, 5, and 14-17 as shown in Figure 21.

4.5 Alloy Compositional Variation Along the Growth Axis

4.5.1 Theoretical Modeling

During directional solidification under conditions of complete mixing and near-equilibrium growth, the compositional variation along the growth axis is given by²⁶

$$C_s(\ell) = k C_o (1 - \ell)^{k-1}, \quad (47)$$

where $C_s(\ell)$ is the solute (CdTe) concentration at a distance ℓ along an ingot of length L , C_o is the initial solute concentration in the melt, and k is the equilibrium distribution coefficient at the liquid-solid interface temperature. The distribution coefficient is given by $k = x^S/x$, where x^S and x^L are respectively the solute compositions of the solid and the liquid at the interface temperature. In the derivation of Equation (47), k is assumed to be independent of the interface temperature.

ORIGINAL PAGE IS
OF POOR QUALITY

Under conditions of elemental diffusion in the melt and negligible mixing, the compositional variation along the growth axis is dependent on the relative values of the interface translation rate, R , and the solute diffusion rate, D , in the melt. For $k > 1$ ($k < 1$), the solute distribution profile is expected to exhibit an initial transient of progressively decreasing (increasing) solute concentration, a region of constant composition equal to the original melt composition, and finally a region of rapidly decreasing (increasing) solute concentration. Smith, Tiller, and Rutter⁸ have examined the mathematical details of the problem and obtained analytical solutions for the transient compositional variations in terms of the material and growth parameters. Their solution for the initial composition-transient for constant R and k is given by

$$C_S(\ell) = \frac{C_0}{2} \left\{ 1 + \operatorname{erf} \left[\frac{1}{2} \left(\frac{R\ell}{D} \right)^{1/2} \right] + (2k - 1)e^{-k(1-k)(R\ell/D)} \right. \\ \left. \times \operatorname{erfc} \left(\frac{2k - 1}{2} \right) \left(\frac{R\ell}{D} \right)^{1/2} \right\}. \quad (48)$$

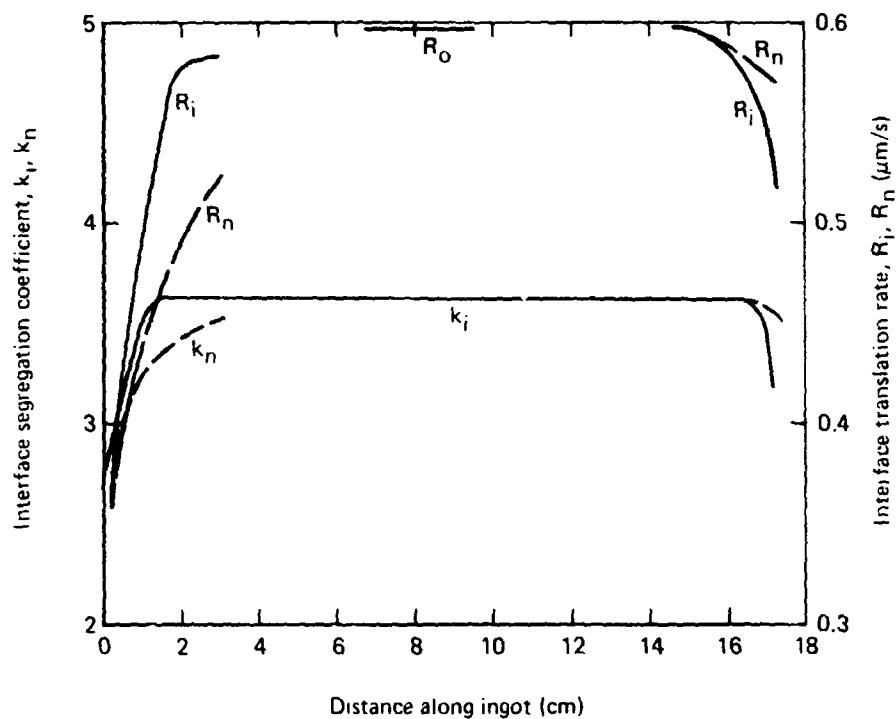
For the final composition-transient, they obtained the expression

$$C_S(\ell) = C_0 \left\{ 1 + \sum_{n=1}^{\infty} (2n + 1) \frac{(1 - k)(2 - k) \dots (n - k)}{(1 + k)(2 + k) \dots (n + k)} \right. \\ \left. \times e^{-n(n+1)[R(L-\ell)/D]} \right\}. \quad (49)$$

In the limit $R\ell \gg D$, the widths of the initial and final transients are small, and $C_S(\ell)$ is essentially independent of ℓ and equal to C_0 . For $R\ell \gg D$ and $k > 0$, the axial compositional profile has an initial transient such that the first-to-freeze solid has a composition $C_S(0) = kC_0$, and with increasing ℓ the composition decreases to a steady-state value of $C_S(\ell) = C_0$. A final transient of rapidly decreasing composition occurs as the melt is consumed. The length of the central steady-state region can be increased at

prior to growth initiation and the uncertainties introduced by the tapered geometry of the ampule tips, renders the initial-transient data unsuitable for quantitative evaluations.

ORIGINAL PAGE 19
OF POOR QUALITY



GP03-0750-51

Figure 25. The variation of the interface segregation coefficient and interface translation rate along the growth axis of ingot L3.

PRECEDING PAGE BLANK NOT FILMED

51, 52

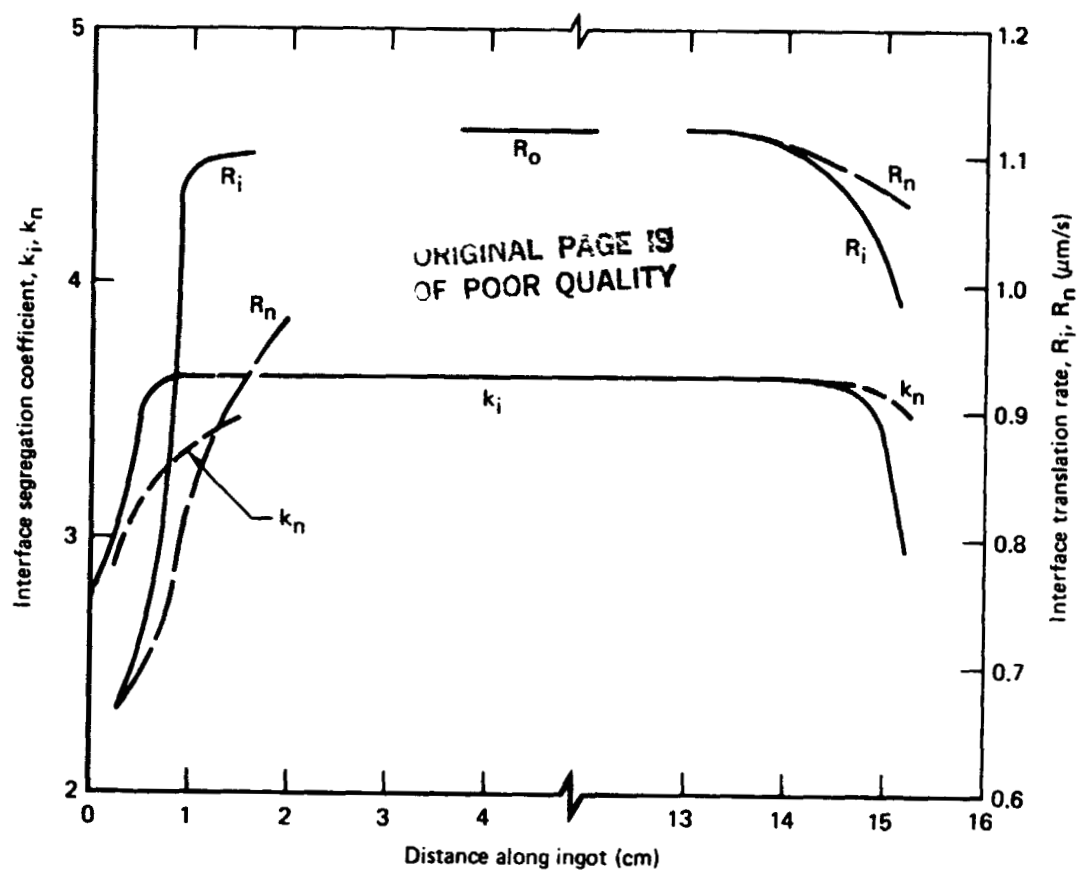
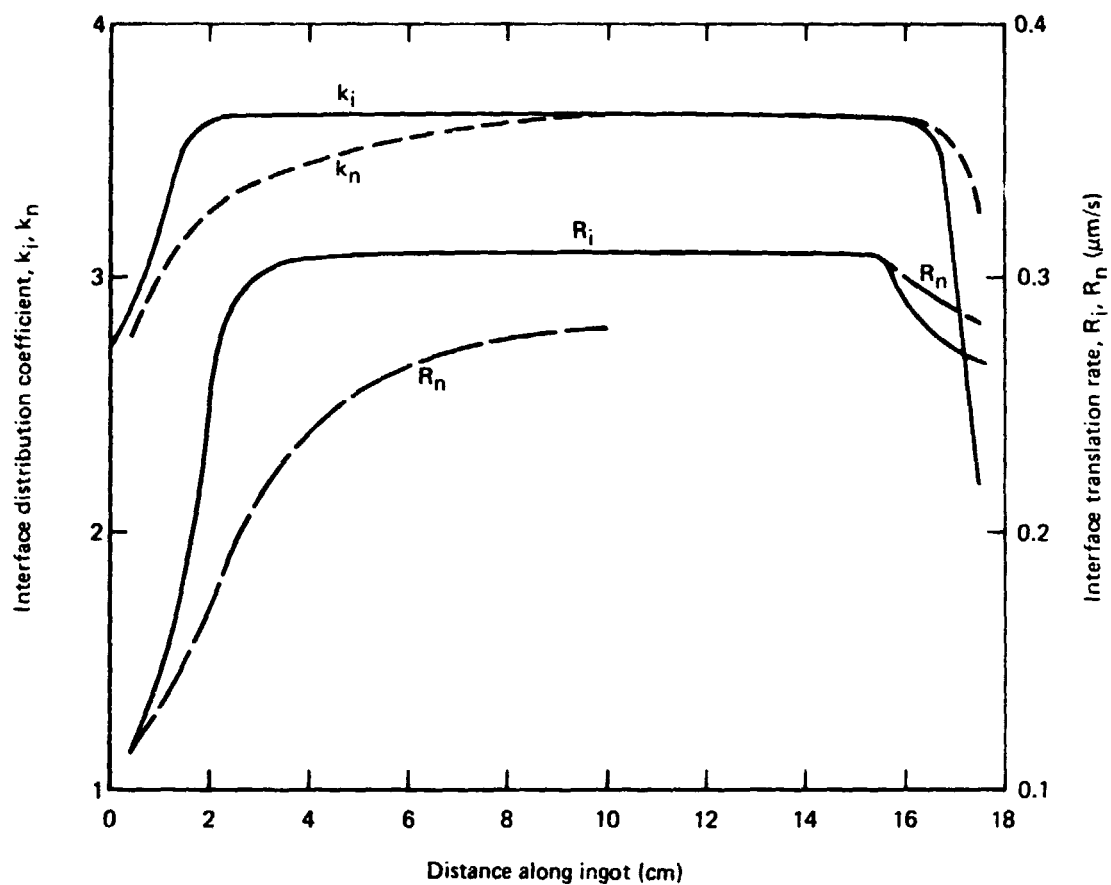


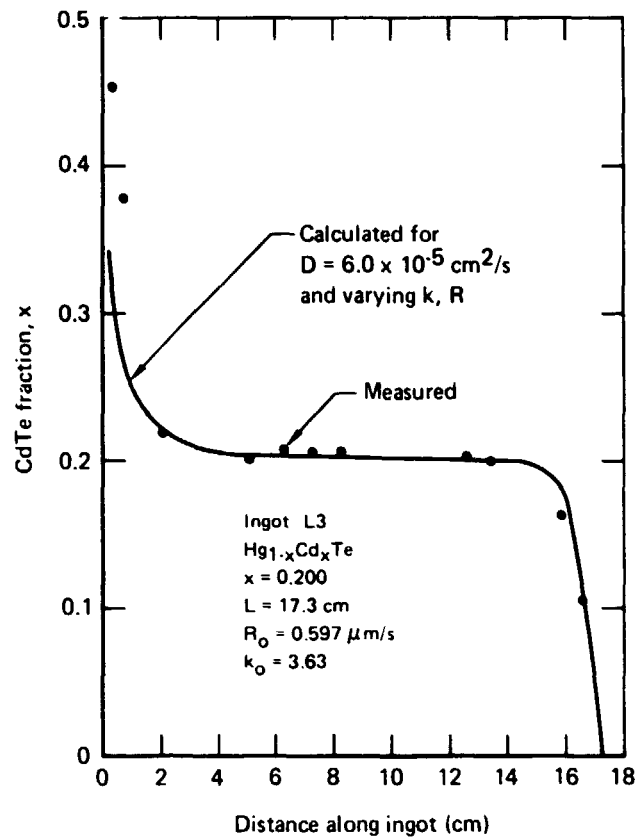
Figure 26. The variation of the interface segregation coefficient and interface translation rate along the growth axis of ingot L4.

ORIGINAL PAGE 18
OF POOR QUALITY



GP03-0750-53

Figure 27. The variation of the interface segregation coefficient and interface translation rate along the growth axis of ingot L6.

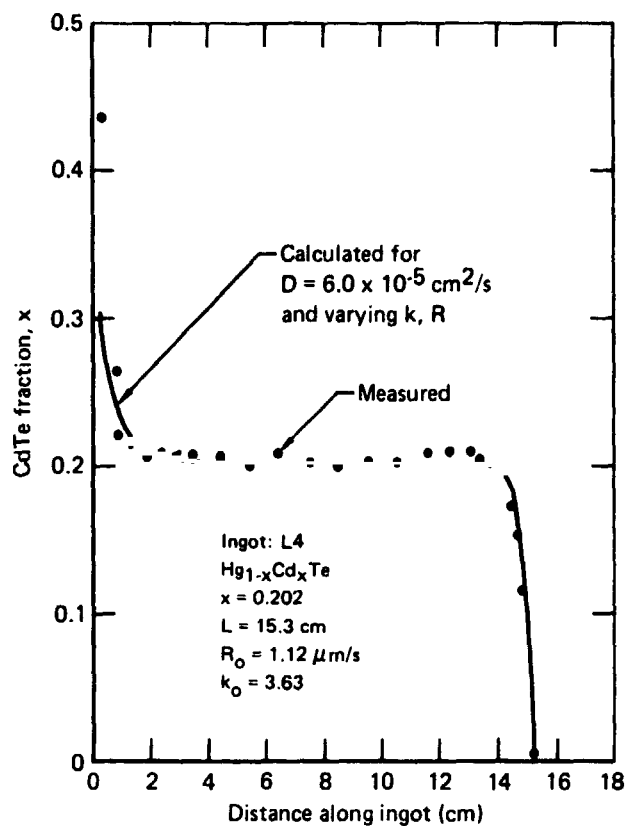


GP03-0750-62

Figure 28. A comparison between the measured and calculated compositional profiles for ingot L3. The calculations assumed a diffusion coefficient of $6.0 \times 10^{-5} \text{ cm}^2/\text{s}$ and included the variations in k and R along the growth axis

ORIGINAL PAGE IS
 OF POOR QUALITY

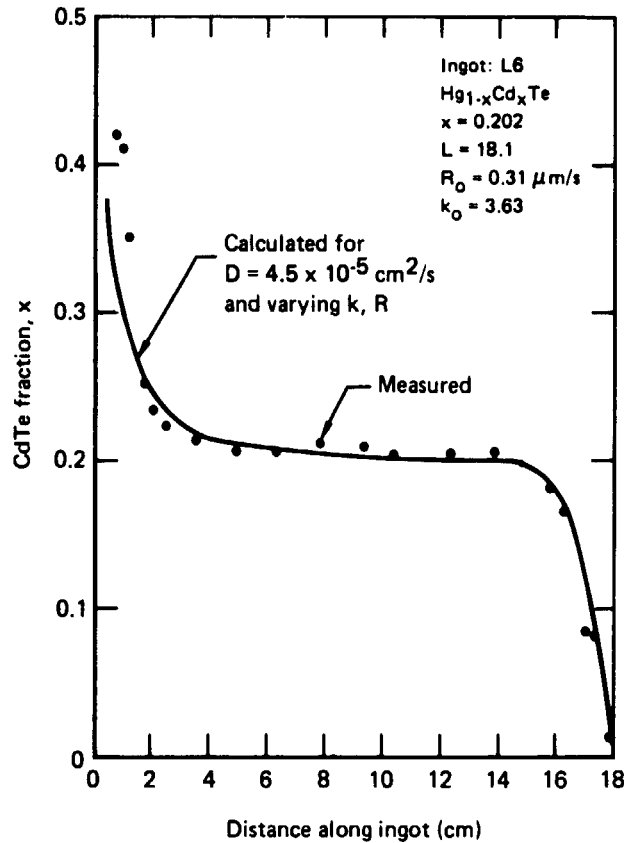
ORIGINAL PAGE 10
OF POOR QUALITY



GP03-0750-61

Figure 29. A comparison between the measured and calculated compositional profiles for ingot L4. The calculations assumed a diffusion coefficient of $6.0 \times 10^{-5} \text{ cm}^2/\text{s}$ and included the variations in k and R along the growth axis.

ORIGINAL PAGE IS
OF POOR QUALITY



GP03-0750-80

Figure 30. A comparison between the measured and calculated compositional profiles for ingot L6. The calculations assumed a diffusion coefficient of $4.5 \times 10^{-5} \text{ cm}^2/\text{s}$ and included the variations in k and R along the growth axis.

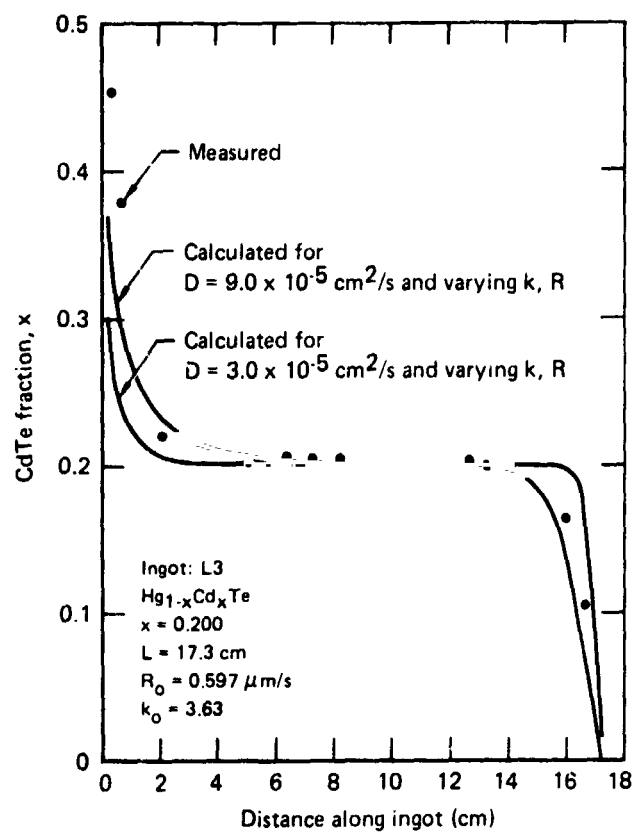


Figure 31. A comparison between the experimental data for ingot L3 and calculated results for various values of the diffusion coefficient.

ORIGINAL PAGE IS
OF POOR QUALITY

ORIGINAL PAGE IS
OF POOR QUALITY

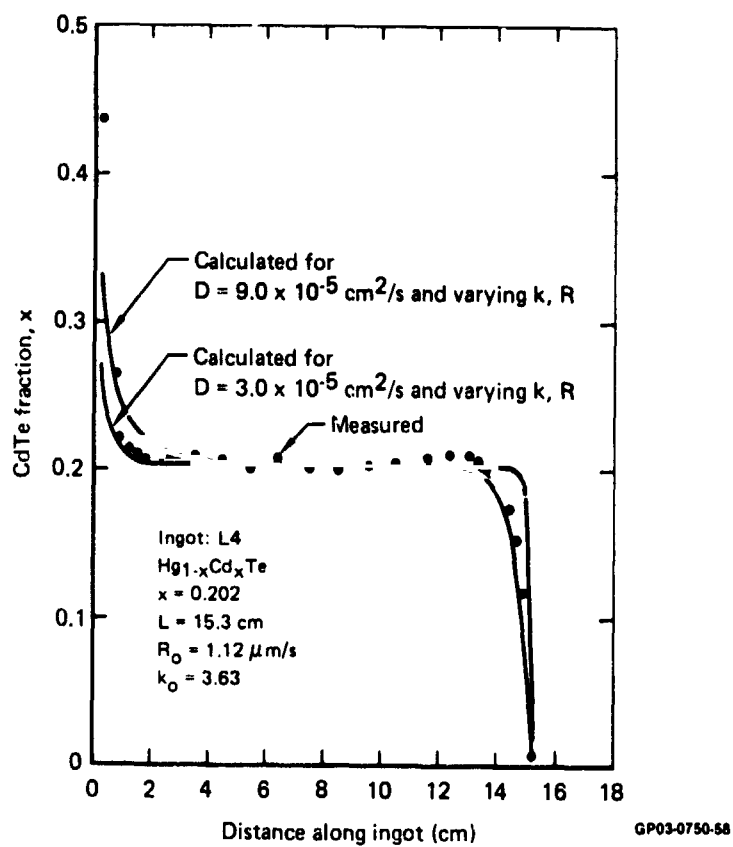


Figure 32. A comparison between the experimental data for ingot L4 and calculated results for various values of the diffusion coefficient.

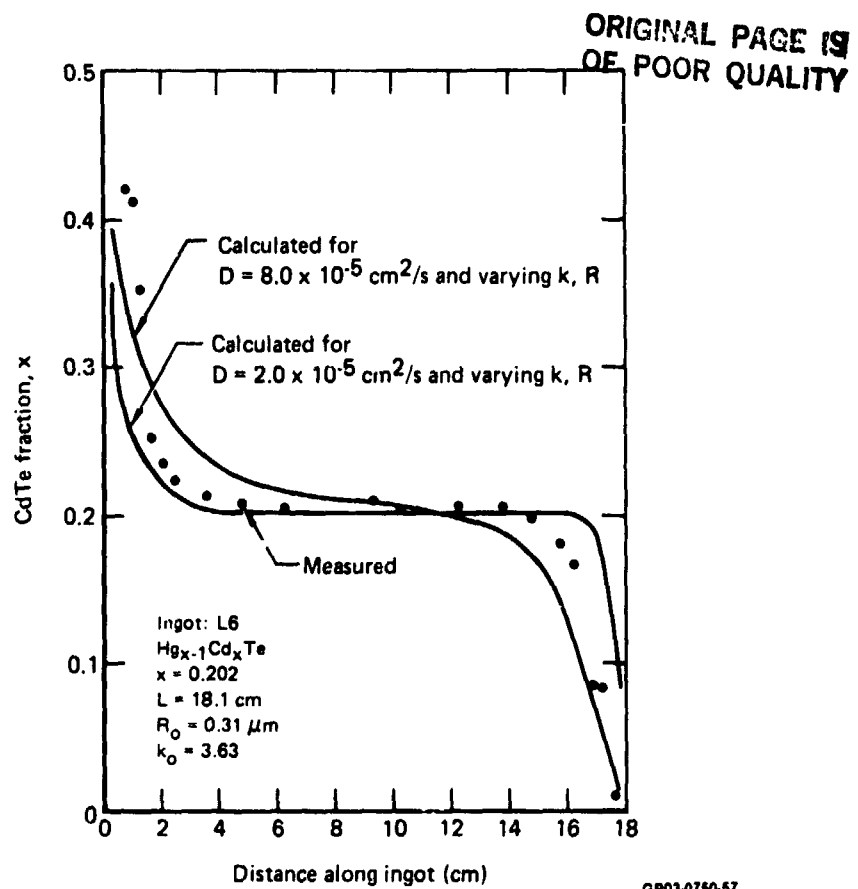
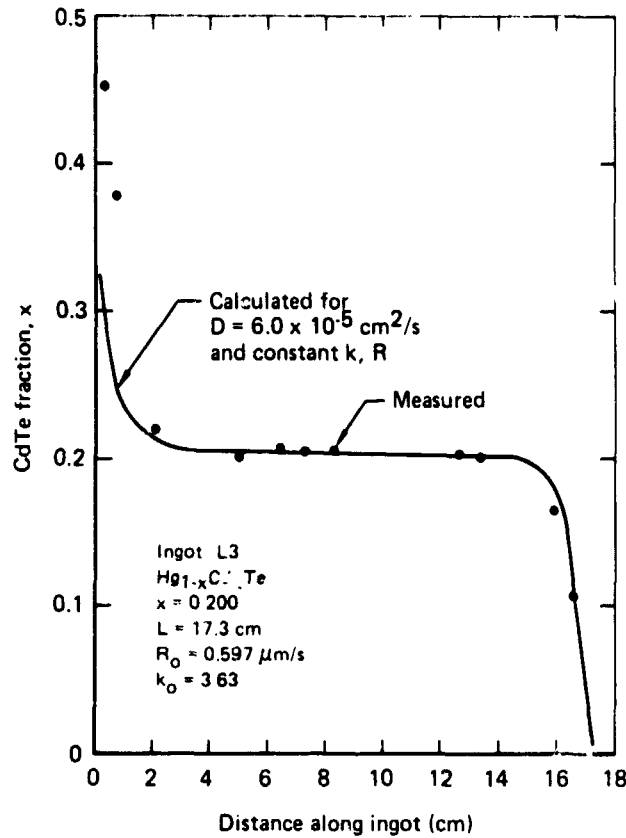
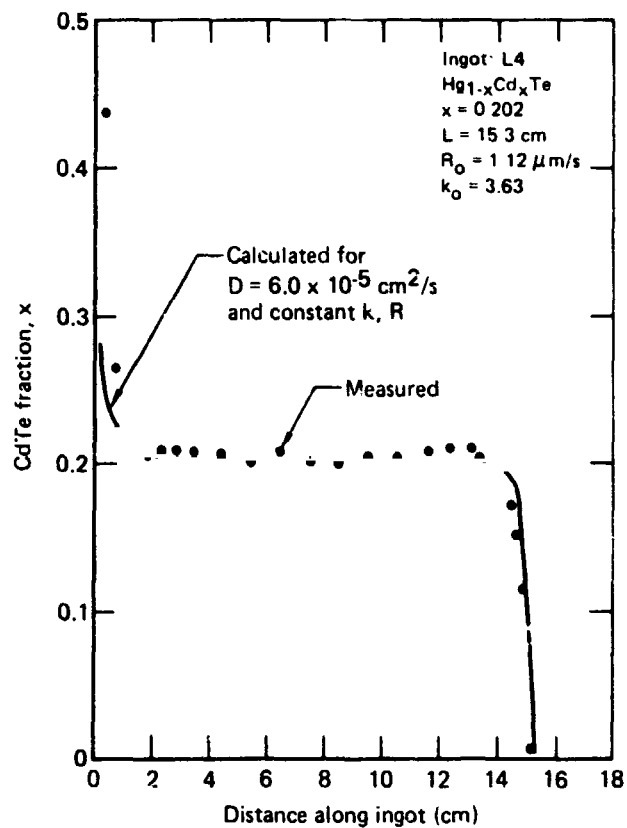


Figure 33. A comparison between the experimental data for ingot L6 and calculated results for various values of the diffusion coefficient.



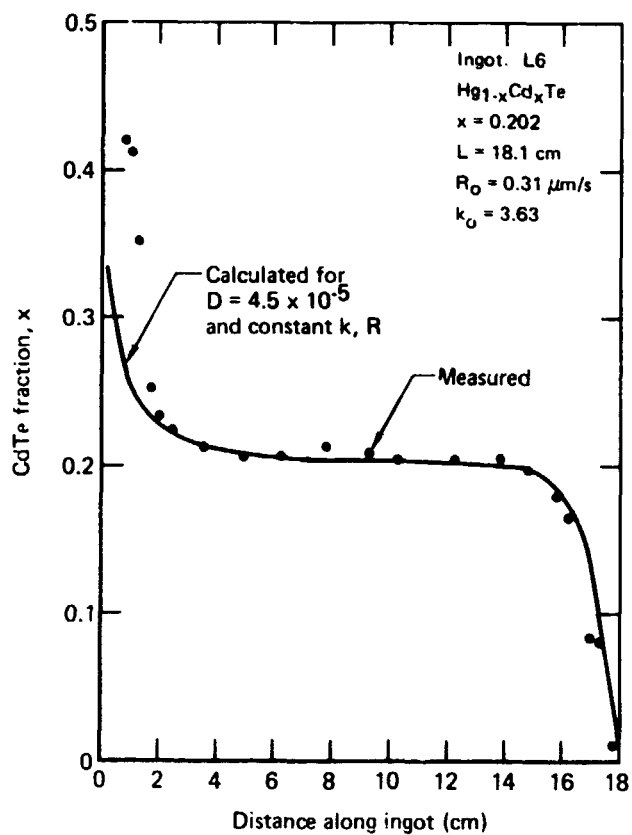
QP03-0750-56

Figure 34. A comparison between the experimental data for ingot L3 and calculated results for a diffusion coefficient of $6.0 \times 10^{-5} \text{ cm}^2/\text{s}$ and constant k, R .



GP03 0750-55

Figure 35. A comparison between the experimental data for ingot L4 and the calculated results for a diffusion coefficient of $6.0 \times 10^{-5} \text{ cm}^2/\text{s}$ and constant k, R .



GP03-0750 54

Figure 36. A comparison between the experimental data for ingot L6 and the calculated results for a diffusion coefficient of $4.5 \times 10^{-5} \text{ cm}^2/\text{s}$ and constant k, R .

5. THEORETICAL MODELING OF CHARGE-CARRIER CONCENTRATIONS AND ELECTRON MOBILITIES

Theoretical models and computer programs specific to $\text{Hg}_{1-x}\text{Cd}_x\text{Te}$ were developed for calculations of charge-carrier concentrations, Hall coefficients, Fermi energies, and electron mobilities as functions of x , temperature, and ionized-defect and neutral-defect concentrations. As in previous work on the HgCdSe alloy system,^{9,10} the Kane three-band model¹¹ is used to describe the $\text{Hg}_{1-x}\text{Cd}_x\text{Te}$ band structure for the energy range of interest, i.e., the lowest-lying conduction band (Γ_6) and the two highest-lying valence bands (Γ_8). Higher-band corrections considered in Reference 9 are neglected because such corrections are estimated to be small for the positive band-gap alloys that are of primary concern in this study. The electron mobilities are calculated in terms of a microscopic theory of electrical conduction derived from the solution of the Boltzmann equation for the perturbed steady-state electron distribution function.

5.1 Energy-Band Structure and Band Parameters

The secular equation describing the conduction, light-hole, and split-off-valence bands is¹¹

$$E^3 + (\Delta - E_g) E^2 - (E_g \Delta + P^2 k^2) E - \frac{2}{3} \Delta P^2 k^2 = 0, \quad (54)$$

where E is the band energy in terms of the crystal momentum wave vector \vec{k} , Δ is the Γ_{15} spin-orbit splitting, E_g is the $\Gamma_6 - \Gamma_8$ energy band-gap, and P is the momentum matrix element between the Γ_{15} valence-band and the Γ_1 conduction-band wave functions defined by Kane.¹¹ The energies are referred to the top of the valence bands. The conduction, c , band and the light-hole, lh , band densities of states are given by

$$\rho_i(E) = \frac{k^2}{\pi^2} \frac{dk}{dE} = \frac{1}{2\pi^2} \left(\frac{3}{2} \right)^{3/2} \frac{E_g^2}{P^3} \lambda_i \quad (i = c, lh), \quad (55)$$

where

$$\lambda_c(\xi) = \frac{3[2\delta^2\xi + \delta(3 - \delta)\xi^2 + \frac{4}{3}(1 - \delta)\xi - \frac{2}{3}] [\xi(\xi - 1)(\delta\xi + 1)]^{1/2}}{2(\frac{3}{2}\delta\xi + 1)^{5/2}}, \quad (56)$$

$$\lambda_{ch}(\xi) = \frac{3[2\delta^2\xi^3 - \delta(3 - \delta)\xi^2 + \frac{4}{3}(1 - \delta)\xi + \frac{2}{3}] [\xi(\xi + 1)(\delta\xi - 1)]^{1/2}}{2(\frac{3}{2}\delta\xi - 1)^{5/2}}, \quad (57)$$

$$\xi = E/E_g, \quad (58)$$

and

$$\delta = E_g/\Delta. \quad (59)$$

The crystal momentum as a function of energy is

$$k = (\frac{3}{2})^{1/2} \frac{E_g}{P} s(\xi), \quad (60)$$

where

$$s(\xi) = \left[\frac{\xi(\xi - 1)(\delta\xi + 1)}{(\frac{3}{2}\delta\xi + 1)} \right]^{1/2}. \quad (61)$$

The conduction-band wave functions are given by

$$|\vec{k}, c, \pm\rangle = e^{i\vec{k}\cdot\vec{r}} [a |1s\alpha_{\mp}\rangle \pm b |(X \mp iY) \alpha_{\pm}\rangle + c |2s\alpha_{\mp}\rangle], \quad (62)$$

where x , y , and z are the basis set of Γ_{15} referred to a coordinate system with the x -axis along \vec{k} , S is the Γ_1 wave function, α_{\pm} are Pauli spin functions for spin parallel (+) and anti-parallel (-) to \vec{k} , and a , b , and c are functions defined by

$$a = [\xi(\delta\xi + 1)(\delta\xi + \frac{2}{3})]^{1/2}/N, \quad (63)$$

$$b = \sqrt{2} (\xi - 1)^{1/2}/3N \quad (64)$$

and

$$c = (\xi - 1)^{1/2} (\delta\xi + \frac{2}{3})/N, \quad (65)$$

where

$$N = [\xi(\delta\xi + 1)(\delta\xi + \frac{2}{3}) + \frac{2}{9}(\xi - 1) + (\xi - 1)(\delta\xi + \frac{2}{3})^2]^{1/2}. \quad (66)$$

The heavy-hole, hh , band is represented by a simple parabolic band given by

$$E_{hh} = \frac{\hbar^2 k^2}{2m_0 \mu_v}, \quad (67)$$

where μ_v is the effective-mass ratio.

5.2 Calculation of the Temperature Dependence of the Carrier Concentrations

The Fermi energy, E_F , electron concentration, n_e , light-hole concentration, n_{lh} , and the heavy-hole concentration, n_{hh} , are calculated from the numerical solution of the charge neutrality equation,

$$n_e - n_{lh} - n_{hh} = N_D - N_A, \quad (68)$$

where

$$n_e = \frac{1}{2\pi^2} \left(\frac{3E_g k_B T}{2P^2} \right)^{3/2} \frac{1}{\beta^{1/2}} \int_{\beta^{-1}}^{\infty} dy \lambda_c(\beta y) f_o(y, z), \quad (69)$$

$$n_{eh} = \frac{1}{2\pi^2} \left(\frac{3E_g k_B T}{2P^2} \right)^{3/2} \frac{1}{\beta^{1/2}} \int_0^{\infty} dy \lambda_{eh}(\beta y) f_o(y, -z), \quad (70)$$

$$n_{hh} = \frac{1}{2\pi^2} \left(\frac{2\mu_{vo} k_B T}{h^2} \right)^{3/2} F_{1/2}(-z), \quad (71)$$

$$z = E_F / k_B T, \quad (72)$$

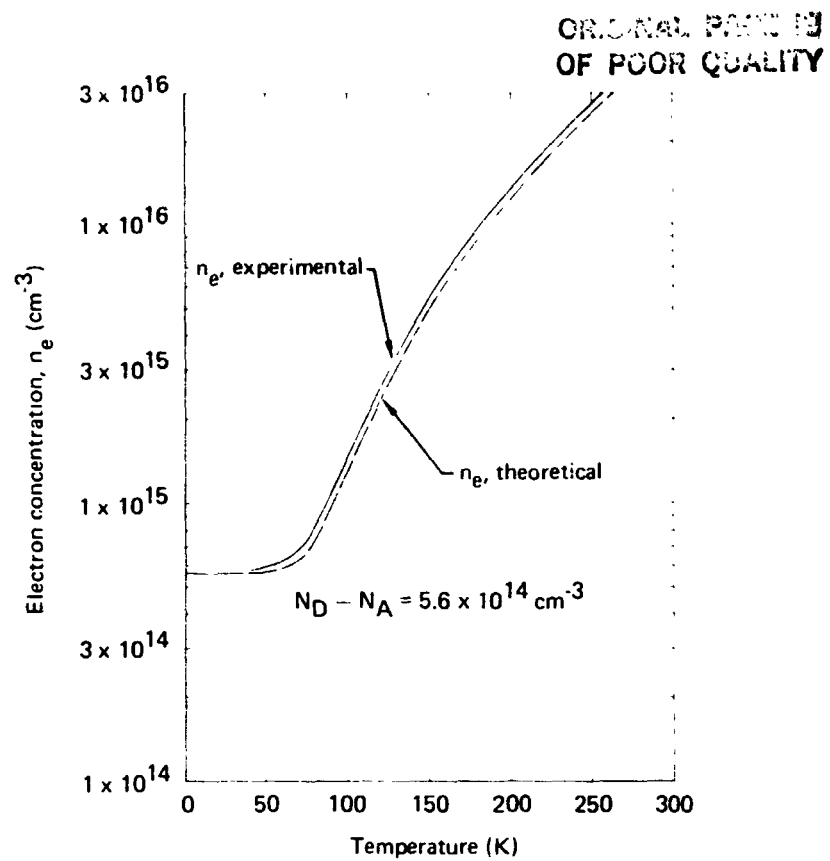
$$\beta = k_B T / E_g, \quad (73)$$

and

$$f_o(y, z) = (e^{y-z} + 1)^{-1}, \quad (74)$$

In Equation (71), $F_{1/2}(-z)$ is the Fermi function of order 1/2, N_A and N_D are respectively the number of acceptors and donors per unit volume, k_B is the Boltzmann constant, T is the absolute temperature, m_o is the free electron mass, and $y = E/k_B T$.

A literature search was performed to compile the best available band parameter values, and these band parameters along with the various material parameters required for the mobility calculations are summarized in Table 15. Using the values for the band parameters given in Table 15, the temperature and x dependences of the Fermi energies and carrier concentrations from 4.2 K to 300 K were calculated from Equations (67)-(70) for various net donor concentrations. The calculated results agree well with available data. A typical comparison between calculated and measured electron concentrations is shown in Figure 37 for an alloy composition of $x = 0.183$ and a net donor density $N_D - N_A = 5.6 \times 10^{14} \text{ cm}^{-3}$.



GP03-0750-47

Figure 37. Theoretical and experimental conduction-electron concentration for $\text{Hg}_{0.817}\text{Cd}_{0.183}\text{Te}$.

TABLE 15. PARAMETERS FOR ELECTRON-MOBILITY AND CHARGE-CARRIER-CONCENTRATION CALCULATION FOR $\text{Hg}_{1-x}\text{Cd}_x\text{Te}$ ALLOYS.

Parameters	Value	Reference [†]
Spin-orbit splitting ^(a)	$\Delta_0 = (-0.18x + 1.08) \text{ eV}$	(1)
Heavy-hole mass ^(b)	$m_{hh}^*/m_0 = 0.53$	(2)
Deformation potentials ^(c)	$E_0 = 11 \text{ eV}$ (longitudinal mode)	(3)
	$E_1 = 9.5 \text{ eV}$	(4)
	$E_2 = 3 \text{ eV}$ } (transverse modes)	
Longitudinal sound velocity ^(d)	$v_L = (2.52 + 0.54x) \times 10^5 \text{ cm/s}$	
Transverse sound velocity ^(d)	$v_T = (1.60 + 0.27x) \times 10^5 \text{ cm/s}$	
Hg mass	$m_{\text{Hg}} = 200.59 \text{ a.m.u.}$	
Cd mass	$m_{\text{Cd}} = 112.4 \text{ a.m.u.}$	
Te mass	$m_{\text{Te}} = 127.60 \text{ a.m.u.}$	
Lattice constant	$a_0 = (0.6460 + 0.0021x) \text{ nm}$	(5)
$\Gamma_6-\Gamma_8$ energy gap	$E_g = [-0.03 + 5 \times 10^{-4}T + (1.91 - 10^{-3}T)x] \text{ eV}$ ($0.135 \leq x \leq 0.203$)	(6)
	$E_g = [-0.303 + 1.73x + 5.6 \times 10^{-4}(1 - 2x)T + 0.25x^4] \text{ eV}$ ($0.23 \leq x \leq 0.61, 10 \text{ K} \leq T \leq 300 \text{ K}$)	(7)
	$E_g = [-0.25x + 1.59x + 5.233 \times 10^{-4}(1 - 2.08x)T + 0.327x^3] \text{ eV}$ ($0.13 \leq x \leq 0.6, 20 \text{ K} \leq T \leq 300 \text{ K}$)	(8)
Momentum matrix element coupling conduction and valence bands ^(e)	$P = 8.55x \times 10^{-8} \text{ eV} \cdot \text{cm}$	
Transverse effective charges	HgTe: $e_T/e^* = 2.96$ CdTe: $e_T/e^* = 2.35$	
Reduced masses	$m_{\text{HgTe}} = 1.295 \times 10^{-22} \text{ g}$ $m_{\text{CdTe}} = 9.923 \times 10^{-23} \text{ g}$	
Dielectric constants ^(f)	$\epsilon_0 = 20.206 - 15.153x + 6.59091x^2 - 0.951826x^3$ $\epsilon_\infty = 15.1077 - 13.8823x + 9.88928x^2 - 3.67133x^3$	(9)
HgTe LO phonon frequency	$\omega_{\text{HgTe LO}} = (139 - 9x) \text{ cm}^{-1}$	
HgTe TO phonon frequency	$\omega_{\text{HgTe TO}} = (118 + 12x) \text{ cm}^{-1}$	
CdTe LO phonon frequency	$\omega_{\text{CdTe LO}} = (154 + 16x) \text{ cm}^{-1}$	(9)
CdTe TO phonon frequency	$\omega_{\text{CdTe TO}} = (152 - 9x) \text{ cm}^{-1}$	

GP03-0750-16

ORIGINAL PAGE IS
OF POOR QUALITY

TABLE 15. (Concluded)

- (a) $\Delta_0 = \Gamma_8 - \Gamma_7$ at $k = 0$. A linear interpolation was made between the HgTe value and the CdTe value.
- (b) $x = 0$, zone center
- (c) The E_1 value is for CdTe (i.e., $x = 1$). The variation of E_1 with x has not been considered. The value of E_2 is estimated based on a hydrogenic approximation.
- (d) $v_L^2 = c_{11}/\rho$, $v_T^2 = c_{44}/\rho$, $\rho = (-2.3x + 8) \text{ g/cm}^3$ [This approximate equation was obtained using data from J. Blair and R. Newnham (10)]. The value of c_{11} for HgTe (300 K) is 50.8 GPa (11), while the value for CdTe is 53.5 GPa (12, 13). The assumption of a linear variation for c_{11} as a function of x yields the result. $c_{11} = (2.7x + 50.8) \text{ GPa}$. The value of c_{44} for HgTe (300 K) is 70.5 GPa (12), while the value for CdTe is 19.9 GPa (12). Assuming a linear variation for c_{44} as a function of x , $c_{44} = (-0.60x + 20.5) \text{ GPa}$. These values for ρ , c_{11} , and c_{44} yield the composition dependence for the velocities given in the table.
- (e) The value of P was calculated from the equation $\hbar^2/m_0^* = (2P^2/3) [2/E_g + 1/(E_g + \Delta)]$, where $x = 0.204$ and values of $m_0^* = 4.66 \times 10^{-3} m_0$, $E_g = 51.7 \times 10^{-3} \text{ eV}$, and $\Delta = 0.96 \text{ eV}$ were used (14)
- (f) These approximate equations were obtained using the referenced data.
1. A. Moritani, K. Taniguchi, and C. Hamaguchi, J. Phys. Soc. Jap. 34, 79 (1973).
 2. V.I. Ivanov-Omskii, B.T. Kolomiets, Yu. F. Markov, A. Sh. Mekhtiev, and K.P. Smekalova, Phys. Status Solidi 32, K83 (1969), Sov. Phys. Semicond. 1, 1203 (1967).
 3. A. Jedrzejczak and T. Dieff, Phys. Status Solidi B 76, 737 (1976)
 4. D. L. Rode, Phys. Rev. B 2, 4036 (1970)
 5. J.C. Woolley and B. Ray, J. Phys. Chem. Solids 13, 151 (1960)
 6. J.D. Wiley and R.N. Dexter, Phys. Rev. 181, 1181 (1969)
 7. M.W. Scott, J. Appl. Phys. 40, 4077 (1969).
 8. J.L. Schmit and E.L. Stelzer, J. Appl. Phys. 40, 4865 (1969).
 9. J. Boors and F. Sorger, Solid State Comm. 10, 875 (1972). F. Sorger, Dissertation, Universitat Freiburg (1972).
 10. J. Blair and R. Newnham, Metallurgy of Elemental and Compound Semiconductors (Wiley Interscience, 1967), p. 399
 11. J.G. Mavroides and D.F. Kolesar, Solid State Comm. 2, 363 (1964).
 12. D.G. Thomas, J. Appl. Phys. 32, 2298 (1961).
 13. H.J. McSkimin and D.G. Thomas, J. Appl. Phys. 33, 56 (1961)
 14. M.A. Kinch and D.D. Buss, The Physics of Semimetals and Narrow-Gap Semiconductors, Ed. by D.L. Carter and R.T. Bate, (Pergamon Press, 1971), p. 461.
- † A good compilation of data on the properties of $\text{Hg}_{1-x}\text{Cd}_x\text{Te}$ is given by R. Dornhaus and G. Nintz, Springer Tracts in Modern Physics, Solid State Physics, (Springer-Verlag, 1976) Vol. 78, p. 1 ff.

GP03-0750-17

5.3 Theoretical Modeling of the Electron Mobility

The electron mobility calculation includes the following scattering mechanisms: longitudinal-optical phonon (LO), longitudinal- and transverse-acoustical phonon (ac), heavy-hole (hh), and alloy disorder potential (dis.). The extrinsic scattering mechanisms include charged (ii) and neutral point-defects (nd). The current densities, conductivities, and mobilities are calculated from the perturbed electron distribution function $f(\vec{k})$ given by

$$f(\vec{k}) = f_0 - kc'(E) f'_0 \cos\psi, \quad (75)$$

where f_0 is the unperturbed distribution function and $f'_0 = \frac{df_0}{dE}$. The quantity ψ is the angle between the wavevector \vec{k} and the applied electric field. The perturbation function $c'(E)$ depends only on the energy. The current density is given by

$$J_x = \frac{e}{3\pi^2\hbar} \int_{E_g}^{\infty} k^2 c'(E) f'_0 dE, \quad (76)$$

where e is the electronic charge, \hbar is Planck's constant, and $c'(E)$ is given by the solution of the Boltzmann equation,

$$\frac{\partial f(\vec{k})}{\partial t} = \sum_i \left(\frac{\partial f}{\partial t} \right)_i + \left(\frac{\partial f}{\partial t} \right)_F \quad (i = \text{LO, ac, eh, dis., ii, nd}). \quad (77)$$

The sum, $\sum_i \left(\frac{\partial f}{\partial t} \right)_i$, is the rate of change of the distribution function caused by the various scattering mechanisms, and $\left(\frac{\partial f}{\partial t} \right)_F$ is the rate of change of the distribution function caused by the application of a static electric field. For the steady-state,

$$\frac{\partial f(\vec{k})}{\partial t} = 0 \quad (78)$$

and

$$\sum_i \left(\frac{\partial f}{\partial t} \right)_i = - \left(\frac{\partial f}{\partial t} \right)_F. \quad (79)$$

ORIGINAL PAGE IS
OF POOR QUALITY

The field term is given by

$$\left(\frac{\partial f}{\partial t} \right)_F = \frac{e e}{\hbar} f'_0 \cos \psi, \quad (80)$$

where e is the applied electric field. The scattering term is given by²⁸

$$\sum_i \left(\frac{\partial f}{\partial t} \right)_i = - \frac{1}{k_B T} \sum_i \int V_1(k, k') [k c'(E) - k' c'(E')] d\mathbf{k}' \cos \psi, \quad (81)$$

where

$$V_1(k, k') = W_1(k', k) f_0(k') [1 - f_0(k)] = V_1(k', k). \quad (82)$$

$W_1(k', k)$ is the transition probability per unit time per unit volume and is given by

$$W_1(k', k) = \left| H_1(\mathbf{k}', \mathbf{k}) \right|^2 \left(\frac{1}{4\pi^3 \hbar^2} \right) \Omega(E_{\mathbf{k}'} - E_{\mathbf{k}} \pm E_S), \quad (83)$$

where $H_1(\mathbf{k}', \mathbf{k})$ is the matrix element for scattering from state \mathbf{k} to \mathbf{k}' for a given scattering process, Ω is a delta function, and E_S is the energy absorbed or emitted in the scattering process.

Equation (79) reduces to a linear finite-difference equation in $c'(E)$, and the conductivity is determined from Equation (76) by using the variational method of Kohler²⁸ as modified by Howarth and Sondheimer²⁷ and Ehrenreich.²⁹ The perturbation function is expanded in a complete set of trial functions,

$$c'(E) = \sum_{n=0}^{\infty} c_n \phi_n(E), \quad (84)$$

and the c_n are determined by the requirement that $c'(E)$ be a stationary point²⁸ of a certain conserved integral.

The various scattering mechanisms and their contributions to the Boltzmann equation are summarized in Appendix A. The computer program for calculating the Fermi energy, the charge-carrier concentrations, and the electron mobilities is given in Appendix B.

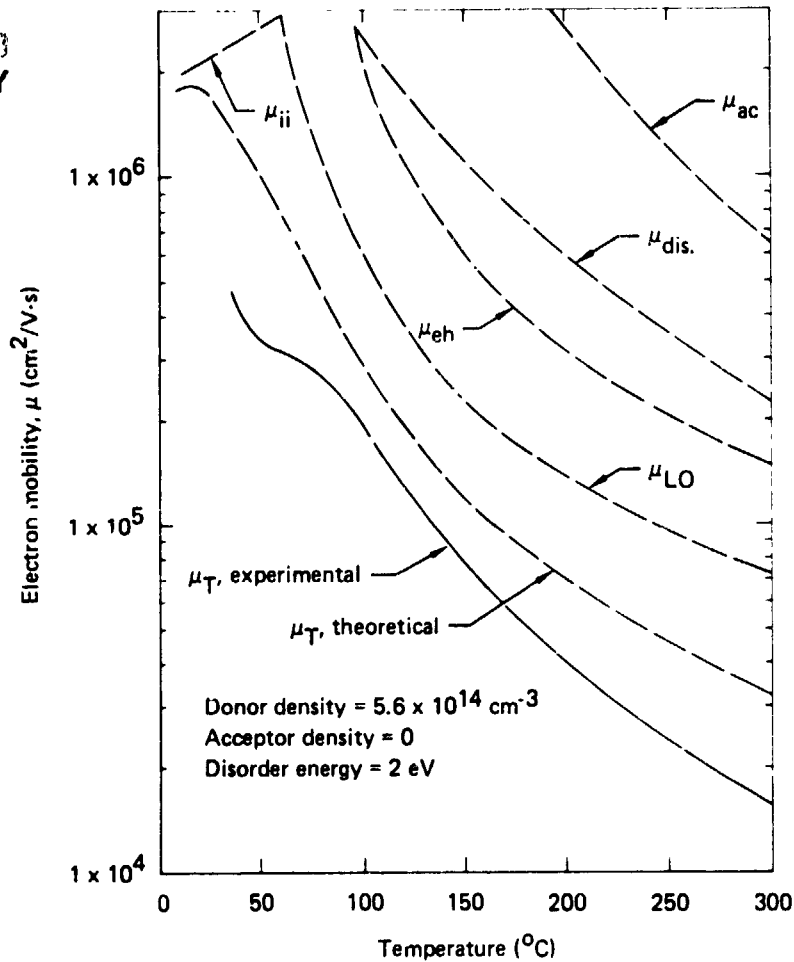
5.4 Calculations of the Temperature Dependence of the Electron Mobility

Calculations were performed to ascertain the relative contributions of the various scattering mechanisms to the conduction electron mobility as functions of temperature from 4.2 K to 300 K for alloy compositions near $x = 0.2$. The material parameters used in the calculations are given in Table 15. Figures 38 and 39 show the calculated results for the sample described in Figure 37. The curves designated by the symbols μ_{LO} , μ_{ac} , $\mu_{dis.}$, μ_{eh} , and μ_{ii} correspond to the calculated mobilities for the individual scattering mechanisms. The calculations shown in Figure 38 were made assuming that all ionized defects are donors, i.e., the donor density is equal to the residual conduction-electron density at low temperatures ($T \lesssim 50$ K). The calculated results in Figure 39 assumed a donor density of $N_D = 7.6 \times 10^{14} \text{ cm}^{-3}$ and an acceptor density of $2.0 \times 10^{14} \text{ cm}^{-3}$. The calculated results indicate that for alloy compositions of $x \approx 0.2$, longitudinal optical-phonon scattering is the dominant mobility-limiting mechanism at high temperatures ($\gtrsim 75$ K), while ionized-defect scattering is the dominant mechanism at low temperatures ($\lesssim 75$ K).

The agreement between the temperature dependence of the calculated total mobility, μ_T , and the experimental data is reasonably good. However, as the temperature increases, the calculated and measured mobilities systematically diverge until at 300 K the calculated mobilities are about a factor of two higher than experimental values. A probable reason for this discrepancy is an overestimate of the screening of the electron-LO-phonon interaction. The approximate screening function used in the calculations treats the electrons as always screening and ignores the possible antiscreening effects considered by Ehrenreich³⁰ for small momentum transfers. The calculations also neglect possible scatterings by neutral point-defects and by line-defects. These,

combined with the uncertainties in the various material parameters, could explain the differences between the calculated and measured results.

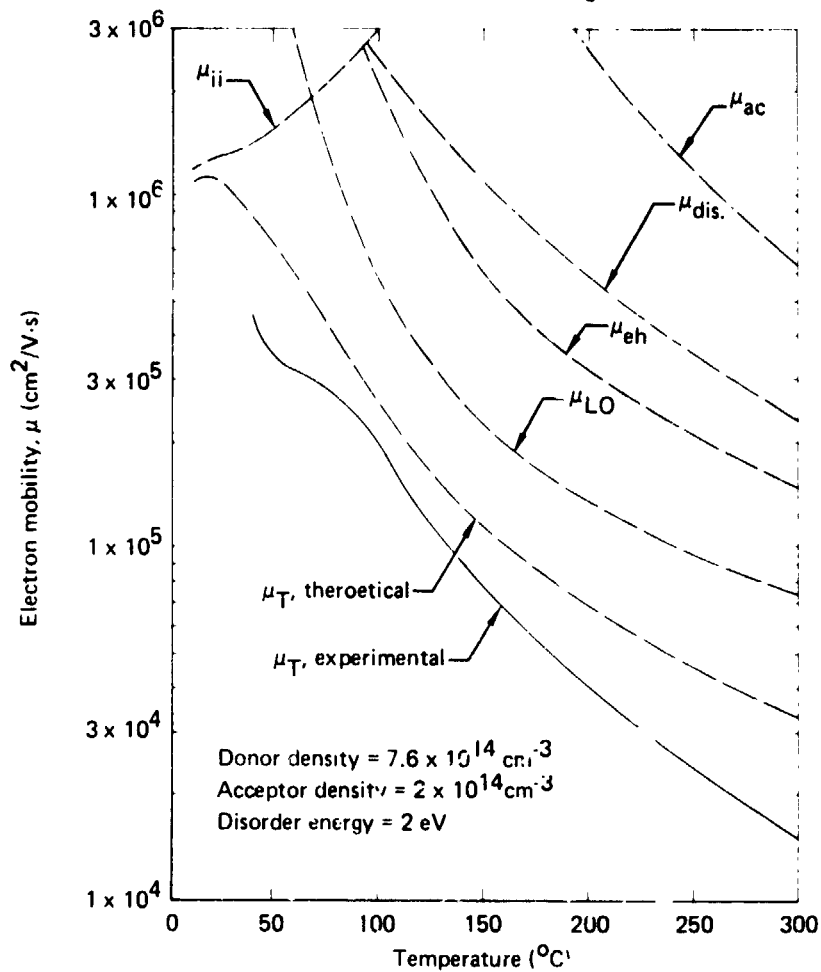
ORIGINAL PAGE IS
OF POOR QUALITY



GP03-0750-48

Figure 38. A comparison of the temperature dependence of the calculated and measured conduction-electron mobilities for an alloy composition of $x = 0.183$. The calculated results are for a donor concentration equal to the residual electron concentration in Figure 37.

ORIGINAL PAGE IS
OF POOR QUALITY



C-1-0750-49

Figure 39. A comparison of the temperature dependence of the calculated and measured conduction-electron mobilities for an alloy composition of $x = 0.183$. The calculations assumed a donor concentration of $7.6 \times 10^{14} \text{ cm}^{-3}$ and an acceptor concentration of $2 \times 10^{14} \text{ cm}^{-3}$.

REFERENCES

1. A. S. Jordan, "A Theory of Regular Associated Solutions Applied to the Liquidus Curves of the An-Te and Cd-Te Systems," *Met. Trans.* 1, 239 (1970).
2. S. Szapiro, "Solid-Liquid Equilibria in Ternary Regular Associated Solutions," *J. Electron. Mat.* 5, 223 (1976).
3. A. J. Strauss, M.I.T. Lincoln Lab., private communication.
4. B. M. Kulwicki, Ph.D. Dissertation, Univ. of Michigan (1963).
5. M. R. Lorenz, "Phase Equilibria in the System Cd-Te," *J. Phys. Chem. Solids* 23, 939 (1962).
6. Jacques Steininger, Alan J. Strauss, and Robert F. Brebrick, "Phase Diagram of the Zn-Cd-Te Ternary System," *J. Electrochem. Soc.: Solid State Sci.* 117, 1305 (1970).
7. Jacques Steininger, "Hg-Cd-Te Phase Diagram Determination by High Pressure Reflux," *J. Electronic Mat.* 5, 299 (1976).
8. V. G. Smith, W. A. Tiller, and J. W. Rutter, "A Mathematical Analysis of Solute Redistribution During Solidification," *Can. J. Phys.* 33, 723 (1953).
9. S. L. Lehoczky, J. G. Broerman, D. A. Nelson, and C. R. Whitsett, "Temperature-Dependent Electrical Properties of HgSe," *Phys. Rev. B* 9, 1598 (1974).
10. D. A. Nelson, J. G. Broerman, C. J. Summers, and C. R. Whitsett, "Electrical Transport in the $Hg_{1-x}Cd_xSe$ Alloy System," *Phys. Rev. B* 18, 1658 (1978).
11. E. C. Kane, "Band Structure of Indium Antimonide," *J. Phys. Chem. Solids* 1, 249 (1957).
12. Methods of Testing Thermocouples and Thermocouple Materials, National Bureau of Standard Circular 590, 1958.
13. Standard Reference Material 44f, Aluminum, freezing point 660.3°C on the International Practical Temperature Scale (1968). Standard Reference Material 44d, Copper, 1084.8°C. The International Practical Temperature Scale of 1968 is described in *Metrologia* 5, 35 (1969).
14. J. P. Schwartz, "A Thermodynamic Investigation of the Ternary Alloy $(Hg_{1-x}Cd_x)_yTe_{1-y}$ Using Vapor Phase Spectroscopy," Ph.D. Dissertation, Marquette University (1977); available from University Microfilms International, Ann Arbor, MI, UMI-78-10294.

15. R. F. Brebnick and A. J. Strauss, "Partial Pressures of Hg(g) and $\text{Te}_2(\text{g})$ in Hg-Te System from Optical Densities," J. Phys. Chem. Solids 26, 989 (1965).
16. ASTM Standard E220-72.
17. B. Ray and P. M. Spencer, "Phase Diagram of the Alloy System HgTe-CdTe," Phys. Stat. Sol. 22, 371 (1967).
18. J. Blair and R. Newnham, "Preparation and Physical Properties of Crystals in the HgTe-CdTe Solid Solution Series", Metallurgy of Elemental and Compound Semiconductors, R. O. Grubel (ed.), (Interscience, 1961), p. 393.
19. T. C. Harman, "Properties of Mercury Chalcogenides," Physics and Chemistry of II-VI Compounds, M. Aren and J. S. Prener (eds.), (North Holland/Wiley/Interscience, 1967), p. 767.
20. J. L. Schmit and C. J. Speerschneder, "Phase Diagram of $\text{Hg}_{1-x}\text{Cd}_x\text{Te}$," Infrared Phys. 8, 247 (1968).
21. J. H. Hildebrand and R. L. Scott, The Solubility of Non-Electrolytes, (Reinhold Publishing Corp., New York, 1950).
22. E. A. Guggenheim, "The Statistical Mechanics of Regular Solutions," Proc. Roy. Soc. A148, 304 (1935).
23. A. S. Jordan and R. R. Zupp, "Calculation of the p-T Diagrams of CdTe," J. Electrochem. Soc. 116, 1285 (1969).
24. J. C. Woolley and B. Ray, "Solid Solutions in $\text{A}^{\text{II}}\text{B}^{\text{VI}}$ Tellurides," J. Phys. Chem. Solids 13, 151 (1960).
25. H. A. Bowman, R. M. Schooner, and M. W. Jones, "Procedure for High Precision Density Determinations by Hydrostatic Weighing," J. Res. Natl. Bur. Std. (U.S.) 71C, 179 (1967).
26. W. G. Pfann, "Calculation of the Minimum Pressure p-Type Diagrams and Solidus of Zinc Telluride," Trans. AIME 194, 747 (1952).
27. D. J. Howarth and E. M. Sondheimer, "The Theory of Electronic Conduction in Polar Semiconductors," Proc. Roy. Soc. A219, 53 (1953).
28. M. Kohler, "Transporterscheinungen Mim Electronengas" Z. Phys. 125, 679, (1949).

29. H. Ehrenreich, "Electron Scattering in InSb", J. Phys. Chem. Solids 2, 131 (1957).
30. H. Ehrenreich, "Screening Effects in Polar Semiconductors," J. Phys. Chem. Solids 8, 130 (1959).

APPENDIX A: ELECTRON SCATTERING MECHANISMS AND THE SOLUTION TO THE BOLTZMANN EQUATION.

The mathematical expressions used for the various scattering mechanisms are essentially the same as those used for the calculations of electron mobilities in the HgCdSe alloys described in References 9 and 10. Some of the pertinent mathematical details are included as part of this report to aid in interpretation of the computer programs.

A.1 Longitudinal-Optical (LO) Phonon Scattering Mechanism

The strength of the LO-phonon/electron interaction is proportional to the Callen effective charge, e_c^* , associated with relative displacements of atoms in a unit cell. The Callen effective charge is related to the Sziget effective charge, e_s^* , and the total transverse charge, e_T^* , by the relations

$$e_c^* = \left[\frac{\epsilon_\infty + 2}{3 \epsilon_\infty} \right] e_s^* \quad (A1)$$

and

$$e_s^* = \frac{e_T^*}{\epsilon_\infty}, \quad (A2)$$

where ϵ_∞ is the high-frequency dielectric constant. The interaction is assumed to be screened by the dielectric function given by

$$\epsilon(\omega_L, q) = \epsilon_\infty + \frac{(k_{FT}^e)^2 + (k_{FT}^{lh})^2}{q^2}, \quad (A3)$$

where ω_L is the longitudinal-phonon frequency, q is the phonon wave vector, and k_{FT}^e and k_{FT}^{lh} are the electron and light-hole Fermi-Thomas momenta given by

$$(k_{FT}^e)^2 = \frac{2e^2}{\pi} \left(\frac{2\mu' m_o}{\hbar^2} \right)^{3/2} \left(\frac{k_B T}{\beta} \right)^{1/2} \int_{\beta^{-1}}^{\infty} dy \lambda_c(y) \frac{e^{y-z}}{(e^{y-z} + 1)^2} \quad (A4)$$

and

$$(k_{FT}^{lh})^2 = \frac{2e^2}{\pi} \left(\frac{2\mu' m_o}{\hbar^2} \right)^{3/2} \left(\frac{k_B T}{\beta} \right)^{1/2} \int_0^{\infty} dy \lambda_{lh}(y) \frac{e^{y+z}}{(e^{y+z} + 1)^2}, \quad (A5)$$

where

$$\mu' = 3\hbar^2 E_g / 4m_o p^2, \quad (A6)$$

and the other parameters have been defined in Sections 5.1 and 5.2. The scattering term of the Boltzmann equation for the LO-phonon-electron interaction is given by

$$\left(\frac{\partial f(\vec{k})}{\partial t} \right)_{LO} = - \frac{e^2 \mu' m_o k_B T (F_1 + F_2)}{\hbar^2 \omega_L \lambda_c s E_g \epsilon_{\infty}^2} \mathcal{L}_{LO}(c') f'_o \cos \psi, \quad (A7)$$

where

$$F_i = \frac{4\pi N_i e_{Ti}^{*2}}{\bar{M}_i} \quad (i = 1 = \text{HgTe}, i = 2 = \text{CdTe}), \quad (A8)$$

N_i is the number of unit cells of the i^{th} type per unit volume, \bar{M}_i is the reduced mass of the i^{th} unit cell, and

$$\mathcal{L}_{LO}(c') = \beta^{-1} \left[\left(f_+/f_o \right) (n_p + 1) (c'_+ R_+ - c'_+ S_+) + (f_-/f_o) n_p (c'_- R_- - c'_- S_-) \right]. \quad (A9)$$

The subscripts (\pm) refer to the evaluation of the function at $y \pm \theta$, where

ORIGINAL PAGE IS
OF POOR QUALITY

$y = E/k_B T$ and $\theta = \hbar\omega_L/k_B T$.

The function, n_p , is the phonon occupation number given by

$$n_p = (e^\theta - 1)^{-1}. \quad (A10)$$

The functions R_\pm and S_\pm are defined as follows:

$$R_\pm(y, \theta) = F_\lambda(y) F_\lambda(y \pm \theta) (s_\pm^2 + s^2) \sum_{n=0}^2 \rho_n^\pm(y, \theta) v_{n+1}^\pm(y, \theta), \quad (A11)$$

$$S_\pm(y, \theta) = F_\lambda(y) F_\lambda(y \pm \theta) s^2 (s_\pm^2 + s^2) \sum_{n=0}^2 \rho_n^\pm(y, \theta) v_n^\pm(y, \theta), \quad (A12)$$

$$F_\lambda(y) = \frac{3 \left[2\delta^2 \beta^3 y^3 + \delta(3 - \delta) \beta^2 y^2 + \frac{4}{3} (1 - \delta) \beta y - \frac{2}{3} \right]}{2 \left(\frac{3}{2} \delta \beta y + 1 \right)^2}, \quad (A13)$$

$$b_1 = [\sqrt{2}/3N(\beta y)] \left[\left(\frac{3}{2} \delta \beta y + 1 \right) / \beta y (\delta \beta y + 1) \right]^{1/2}, \quad (A14)$$

$$c_1 = [(\delta \beta y + \frac{2}{3})/N(\beta y)] \left[\left(\frac{3}{2} \delta \beta y + 1 \right) / \beta y (\delta \beta y + 1) \right]^{1/2}, \quad (A15)$$

$$\begin{aligned} \rho_o^\pm(y, \theta) = & (aa_\pm)^2 - bb_\pm [bc_\pm + cb_\pm] / \sqrt{2} \\ & + \frac{1}{2} (bc_\pm + cb_\pm)^2 + \frac{1}{4} (bb_\pm)^2, \end{aligned} \quad (A16)$$

$$\rho_1^\pm(y, \theta) = 2aa_\pm (b_1 b_{1\pm} + c_1 c_{1\pm}), \quad (A17)$$

ORIGINAL PAGE IS
OF POOR QUALITY

$$\rho_2^\pm(y, \theta) = \frac{3}{4} (b_1 b_{1\pm})^2 + b_1 b_{1\pm} [(b_1 c_{1\pm} + c_1 b_{1\pm})/\sqrt{2}]$$

(A18)

$$+ 2b_1 b_{1\pm} c_1 c_{1\pm} - \frac{1}{2} (b_1 c_{1\pm} + c_1 b_{1\pm})^2 + (c_1 c_{1\pm})^2,$$

$$v_0^\pm(y, \theta) = -\frac{1}{q_\pm} \left(\frac{2g_\infty^2 r_\pm^2}{p_\pm^2 - 4r_\pm^2} + \frac{1}{2} \ln \left| \frac{p_\pm - 2r_\pm}{p_\pm + 2r_\pm} \right| \right),$$

(A19)

$$v_1^\pm(y, \theta) = r_\pm \left(\frac{p_\pm}{p_\pm^2 - 4r_\pm^2} - \frac{1}{q_\pm} - \frac{p_\pm^2}{q_\pm(p_\pm^2 - 4r_\pm^2)} \right)$$

(A20)

$$+ \frac{1}{4} \left(1 - \frac{2p_\pm}{q_\pm} \right) \ln \left| \frac{p_\pm - 2r_\pm}{p_\pm + 2r_\pm} \right|,$$

$$v_2^\pm(y, \theta) = \frac{1}{4} \left\{ r_\pm \left[1 - \frac{2p_\pm}{q_\pm} + \left(1 - \frac{p_\pm}{q_\pm} \right) \frac{p_\pm^2}{p_\pm^2 - 4r_\pm^2} \right] \right.$$

(A21)

$$\left. + \frac{p_\pm}{2} \left(2 - \frac{3p_\pm}{q_\pm} \right) \ln \left| \frac{p_\pm - 2r_\pm}{p_\pm + 2r_\pm} \right| \right\},$$

$$v_3^\pm(y, \theta) = -\frac{r_\pm^3}{3q_\pm} + \frac{p_\pm r_\pm}{2} \left(1 - \frac{3p_\pm}{2q_\pm} + \frac{p_\pm^2}{2(p_\pm^2 - 4r_\pm^2)} \right.$$

(A22)

$$\left. - \frac{p_\pm^3}{2q_\pm(p_\pm^2 - 4r_\pm^2)} \right) + \frac{p_\pm^2}{16} \left(3 - \frac{4p_\pm}{q_\pm} \right) \ln \left| \frac{p_\pm - 2r_\pm}{p_\pm + 2r_\pm} \right|,$$

$$q_\pm = s_\pm^2 + s^2,$$

(A23)

$$p_{\pm} = q_{\pm} + g_{\infty}^2, \quad (\text{A24})$$

$$r_{\pm} = ss_{\pm}, \quad (\text{A25})$$

and

$$g_{\infty}^2 = \frac{\hbar^2}{2\mu'_m E_o \epsilon_{\infty}} [(k_{FT}^e)^2 + (k_{FT}^h)^2]. \quad (\text{A26})$$

The symbols a , b , and c have been defined in Section 5.1. In the above, R_- and S_- are zero for $y - \theta - \beta^{-1} < 0$.

A.2 Acoustical Phonon (ac) Scattering Mechanism

The longitudinal and transverse acoustical-phonon/electron interactions are characterized by three deformation potentials: E_o for the longitudinal mode and E_1 and E_2 for the transverse modes. The acoustical-phonon contribution to the Boltzmann equation is given by

$$\left(\frac{\partial f(\vec{k})}{\partial t} \right)_{ac} = \frac{2k_B T E_o^2}{\pi \hbar^5 \rho_m v_L^2} (\mu'_m)^2 E_g \lambda_c s \quad (\text{A27})$$

$$\times \left[F_L + \left(\frac{v_L}{v_T} \right)^2 F_T \right] f_o' \cos \psi c'(E),$$

where ρ_m is the mass density of the material, and v_L and v_T are the longitudinal and transverse velocities of sound, respectively.

The longitudinal and transverse scattering functions, F_L and F_T , are given by

$$F_L = A_1^2 + \frac{2}{3} (A_1 A_2 + A_4) - \frac{1}{2} (2A_1 A_3 + A_2^2 - A_4) + \frac{4}{5} A_2 A_3 + \frac{1}{3} A_3^2 \quad (\text{A28})$$

and

$$F_T = (E_1^2/E_0^2) (B_1 + \frac{2}{3} B_2 + \frac{1}{2} B_3 + \frac{2}{5} B_4 + \frac{1}{3} B_5 + B_6), \quad (A29)$$

where

$$A_1 = a^2 + (E_1/E_0) (\frac{1}{2} b^2) + (E_2/E_0) (c^2 + \frac{1}{2} b^2), \quad (A30)$$

$$A_2 = - (E_1/E_0) (c^2 + \frac{1}{2} b^2) + (E_2/E_0) (5c^2 + \frac{1}{2} b^2), \quad (A31)$$

$$A_3 = 4(E_2/E_0) (c^2 - \frac{1}{2} b^2), \quad (A32)$$

$$A_4 = (E_1/E_0)^2 b^2 c^2, \quad (A33)$$

$$B_1 = \frac{1}{4} b^4, \quad (A34)$$

$$B_2 = -b^2 [b(b + \sqrt{2} c) + \frac{1}{4} b^2 - (b + c/\sqrt{2})^2], \quad (A35)$$

$$B_3 = b^2 [(b + \sqrt{2} c)^2 + b(b + \sqrt{2} c) - 2(b + c/\sqrt{2})(b + \sqrt{2} c) \quad (A36)$$

$$- (b + c/\sqrt{2})^2],$$

$$B_4 = 2b^2 (b + c/\sqrt{2})(b + \sqrt{2} c), \quad (A37)$$

$$B_5 = -b^2(b + \sqrt{2}c)^2, \quad \text{ORIGINAL PAPER OF POOR QUALITY} \quad (A38)$$

and

$$B_6 = \frac{1}{2} [b^2 c^2 + \frac{1}{3} (c^2 - \frac{1}{2} b^2)^2]. \quad (A39)$$

A.3 Ionized Impurity (ii) Scattering Mechanism

The electron/ionized-defect interaction is assumed to be screened by the dielectric function

$$\epsilon(q) = \epsilon_0 + \frac{1}{2} \frac{1}{q} [(k_{FT}^e)^2 + (k_{FT}^{lh})^2 + (k_{FT}^{nh})^2], \quad (A40)$$

where k_{FT}^{hh} is the heavy-hole Fermi-Thomas momentum, given by

$$(k_{FT}^{hh})^2 = \frac{e^2}{\pi} \left(\frac{2\mu_v m_0}{\hbar^2} \right)^{3/2} (k_{BT})^{1/2} F_{-1/2}(-z), \quad (A41)$$

ϵ_0 is the low-frequency dielectric constant, and $F_{-1/2}$ is the Fermi function of order $-1/2$.

The contribution to the Boltzmann equation from ionized-impurity scattering is

$$\left(\frac{\partial f(\vec{k})}{\partial t} \right)_{ii} = \frac{\pi (N_D Z_D^2 + N_A Z_A^2) e^4 \lambda_c}{\hbar \epsilon_0^2 E_g^3} \phi_{ii} f'_0 \cos \psi c'(E), \quad (A42)$$

where N_D and N_A are the donor and acceptor concentrations, respectively, and Z_D and Z_A are their charges in electron-charge units. The scattering function, ϕ_{ii} , is given by

ORIGINAL DESIGN
OF POOR QUALITY

$$\phi_{11} = \sum_{n=0}^2 \pi_n \phi_n, \quad (A43)$$

where

$$\phi_0 = \ln[(g_0^2 + 4s^2)/g_0^2] - 4s^2/(g_0^2 + 4s^2), \quad (A44)$$

$$\phi_1 = \frac{g_0^2 + s^2}{s^2} \ln\left(\frac{g_0^2 + 4s^2}{g_0^2}\right) - \frac{4(g_0^2 + 3s^2)}{(g_0^2 + 4s^2)}, \quad (A45)$$

$$\begin{aligned} \phi_2 = \frac{g_0^2}{2s^2} \left[-\frac{4(g_0^2 + s^2)}{g_0^2} + \frac{(g_0^2 + 2s^2)(3g_0^2 + 2s^2)}{2s^2 g_0^2} \right. \\ \left. \times \ln\left(\frac{g_0^2 + 4s^2}{g_0^2}\right) - \frac{2(g_0^2 + 2s^2)^2}{g_0^2 (g_0^2 + 4s^2)} \right], \quad (A46) \end{aligned}$$

$$\pi_0 = a^4 + \frac{1}{4} b^4 - \sqrt{2} b^3 c + 2b^2 c^2, \quad (A47)$$

$$\pi_1 = 2a^2(b^2 + c^2), \quad (A48)$$

$$\pi_2 = \frac{3}{4} b^4 + \sqrt{2} b^3 c + c^4, \quad (A49)$$

with

$$g_0^2 = \frac{\hbar^2 [(k_{FT}^e)^2 + (k_{FT}^{lh})^2 + (k_{FT}^{hh})^2]}{2\mu^* m_0 E_g \epsilon_0} \quad (A50)$$

A.4 Electron-Hole (eh) Scattering Mechanism

The contribution to the Boltzmann equation from electron-hole scattering is

$$\left(\frac{\partial f(\vec{k})}{\partial t} \right)_{eh} = \frac{\pi n_{hh} e^4 \lambda_c}{\hbar \epsilon_\infty^2 E_g s^3} \phi_{eh} f'_0 \cos \psi c'(E), \quad (A51)$$

where ϕ_{eh} is the same as ϕ_{ii} for ionized defect scattering except that g_0 is replaced by g_∞ , i.e.,

$$g_\infty^2 = \frac{\hbar^2 [(k_{FT}^e)^2 + (k_{FT}^{lh})^2 + (k_{FT}^{hh})^2]}{2\mu^* m_0 E_g \epsilon_\infty} \quad (A52)$$

A.5 Compositional-Disorder (dis.) Scattering Mechanism

Electron scattering by the random short-range potentials resulting from alloy compositional disorder is treated as scattering by a random distribution of square-well scattering centers, which have unit-cell dimensions and depths approximately equal to the difference in band gaps between CdTe and HgTe. The contribution to the Boltzmann equation from this process is given by

$$\left(\frac{\partial f(\vec{k})}{\partial t} \right)_{dis.} = \frac{E_g}{\pi \hbar^5} (\mu^* m_0)^2 s \lambda_c \frac{x(1-x) E_{dis.}^2}{N_a} \phi_{dis.} c' f'_0 \cos \psi, \quad (A53)$$

where N_a is the number of unit cells per unit volume, $E_{dis.}$ is the disorder potential, approximately equal to the difference in CdTe and HgTe band gaps, and $\phi_{dis.}$ is a wave-function-overlap integral given by

ORIGINAL PAGE IS
OF POOR QUALITY

$$\phi_{\text{dis.}} = 2a^4 + b^4 + \frac{2}{3}c^4 - \frac{4}{3}\sqrt{2}b^3c + 4b^2c^2 - \frac{4}{3}a^2(b^2 + c^2). \quad (\text{A54})$$

A.6 Neutral-Defect (nd) Scattering Mechanism

The scattering of electrons by neutral point-defects is also described in terms of scattering by a random distribution of square-well potentials. Thus the contribution of neutral point-defects to the Boltzmann equation is also given by Equation (A53) with $x(1-x) E_{\text{dis.}}^2 / N_a$ replaced by $N_n \mu_n^2 E_n^2$, where N_n is the density of neutral point-defects, μ_n is the volume of the potential well, and E_n is the strength.

A.7 Calculation of the Electron Mobility

The total scattering contribution to the Boltzmann equation from the scattering mechanisms considered is

$$\sum_i \left(\frac{\partial f(\vec{k})}{\partial t} \right)_i = - \frac{e^2 \mu_o' m_o k_B T (F_1 + F_2)}{\hbar^2 \omega_L \lambda_c s E_g \epsilon_\infty^2} \mathcal{L}(c') f_o' \cos \psi, \quad (\text{A55})$$

where

$$\begin{aligned} \mathcal{L}(c') = \mathcal{L}_{LO}(c') - & \left\{ a_{ac} \lambda_c^2 s^2 \left[F_L + \left(\frac{v_L}{v_T} \right)^2 F_T \right] + a_{ii} \frac{\lambda_c^2}{s^2} \phi_{ii} \right. \\ & \left. + a_{eh} \frac{\lambda_c^2}{s^2} \phi_{eh} + (a_{\text{dis.}} + a_n) \lambda_c^2 s^2 \phi_{\text{dis.}} \right\} c'(E), \end{aligned} \quad (\text{A56})$$

with the following defined quantities:

$$a_{ac} = \frac{2E_0^2 \mu' m_0 E_g \omega_L \epsilon_\infty^2}{\pi \hbar^3 \rho_m v_L^2 e^2 (F_1 + F_2)}, \quad (A57)$$

$$a_{ii} = \frac{\pi \hbar^2 \omega_L \epsilon_\infty^2}{\mu' m_0 k_B T (F_1 + F_2) \epsilon_0^2} \left(Z_D^2 N_D + Z_A^2 N_A \right), \quad (A58)$$

$$a_{eh} = \frac{\pi \hbar e^2 \omega_L n_{hh}}{\mu' m_0 k_B T (F_1 + F_2)}, \quad (A59)$$

$$a_{dis.} = \frac{E_g^2 \mu' m_0 \omega_L \epsilon_\infty^2 E_{dis.}^2 x (1-x)}{\pi \hbar^3 e^2 k_B T N_a (F_1 + F_2)}, \quad (A60)$$

and

$$a_n = \frac{E_g^2 \mu' m_0 \omega_L \epsilon_\infty^2 N_n n_n^2 E_n^2}{\pi \hbar^3 e^2 k_B T (F_1 + F_2)}. \quad (A61)$$

The substitution of Equation (A55) into the steady-state Boltzmann equation, Equation (79), yields the following linear finite-difference equation:

$$\mathcal{L}(c') = \frac{2^{1/2} \pi^2 \omega_L \epsilon_\infty^2}{e (\mu' m_0)^{3/2} (F_1 + F_2)} (k_B T)^{1/2} \frac{s^2}{\beta^{3/2}}. \quad (A62)$$

To obtain a solution, the perturbation function, $c'(E)$, is expanded in a complete set of trial functions,

$$c'(E) = \sum_{n=0}^{\infty} c_n \phi_n(E). \quad (A63)$$

and the c_n are determined by the requirement that $c'(E)$ be a stationary point²⁸ of a certain conserved integral. The set,

$$\phi_n = (y - \beta^{-1})^n, \quad (\text{A64})$$

is used for the trial functions, and the expansion is carried to third order (i.e., $n = 2$). The current density J_x , Equation (75), is given by

$$J_x = \frac{4\epsilon_\infty^2 \omega_L (k_B T)^2}{3\pi^2 \hbar^2 (F_1 + F_2)} \left\{ \frac{L^{(0)2}}{F_{00}} + \frac{[(\mathcal{L}, \ell)_1]^2}{\mathcal{L}_2 \mathcal{L}_1} + \frac{[(\mathcal{L}, \ell)_2]^2}{\mathcal{L}_3 \mathcal{L}_2} + \dots \right\}, \quad (\text{A65})$$

where

ORIGINAL PAGE IS
OF POOR QUALITY

$$\mathcal{L}_{n+1} = \begin{vmatrix} F_{00} & \dots & F_{01} & \dots & F_{0n} \\ F_{10} & \dots & \dots & \dots & \dots \\ \vdots & & \vdots & & \vdots \\ \vdots & & \vdots & & \vdots \\ \vdots & & \vdots & & \vdots \\ \vdots & & \vdots & & \vdots \\ F_{n0} & \dots & \dots & \dots & F_{nn} \end{vmatrix}, \quad (\text{A66})$$

$$(\mathcal{L}, \ell)_n = \begin{vmatrix} F_{00} & \dots & F_{0,n-1} & L^{(0)} \\ \vdots & & \vdots & \vdots \\ \vdots & & \vdots & \vdots \\ \vdots & & \vdots & \vdots \\ F_{n,0} & \dots & \dots & L^{(n)} \end{vmatrix}, \quad (\text{A67})$$

$$F_{mn} = \int_{\beta^{-1}}^{\infty} \phi_m \mathcal{L}(\phi_n) f'_0 dy, \quad (\text{A68})$$

and

$$L^{(n)} = \int_{\beta^{-1}}^{\infty} \phi_n f'_0 \frac{s^3}{\beta^{3/2}} dy. \quad (\text{A69})$$

The electrical conductivity, σ , is given by the relation

$$\sigma = J_x / \mathcal{E}, \quad (\text{A70})$$

and the electron mobility is given by

$$\mu = \sigma / n_e e. \quad (\text{A71})$$

APPENDIX B: COMPUTER PROGRAMS FOR CALCULATION OF CHARGE CARRIER
CONCENTRATIONS AND ELECTRON MOBILITIES

B.1 Description of Symbols - Main Program

Line no.	Comments
00330	Input parameters: TMIN = minimum temperature (K), TMAX = maximum temperature (K), DELT = temperature increment, DONOR DENSITY (cm^{-3}), ACCEPTOR DENSITY (cm^{-3}), PROPORTION OF CdTe IN ALLOY (at.%), DISORDER ENERGY IN (eV).
00500	ES = electron charge in c.g.s. units.
00510	HB = Planck's constant (erg-s).
00520	K = Boltzmann's constant (erg/K).
00530	MO = free electron mass (g).
00540	PI = π .
00550	CEVE = units conversion factor (eV to ergs).
00560	FFCTS is an external program for evaluating Fermi functions. A separate data file of the values of Fermi functions is required.
00705	X2 = at.% of CdTe in alloy, x.
00706	X1 = at.% of HgTe in alloy, $1 - x$.
00741	HCSPOL is an external program used for determining a number of parameters used in the calculations.
00790	TMIN = minimum temperature (K).
00800	TMAX = maximum temperature (K).
00810	DELT = temperature increment.
00820	ND = donor density.
00840	NA = acceptor density.
00880	DEV = spin-orbit splitting (in eV) as a function of x.
00885	D = spin-orbit splitting (in ergs) as a function of x.
00890	UV = heavy hole mass (in electron mass units)
00960 to 00980	E0EV, E1EV, and E2EV are deformation potentials in eV.
00990	VL = longitudinal sound velocity as a function of x.
01000	VT = transverse sound velocity as a function of x.
01030	M00 = Te mass in amu
01040	M1 = Hg mass in amu
01050	M2 = Cd mass in amu
01060	PHI = mass density
01070	AL = lattice constant as a function of x.
01110	EDISEV = disorder energy in eV.
01120	EDIS = disorder energy in ergs.
01140 to 01160	EPHI0, EPHI1, EPHI2 are deformation potentials in ergs.

GP03-0750-03

Line no.	Comments
01170	E1S = optical phonon scattering contribution.
01180	E2S = optical phonon scattering contribution.
01190	M1B = reduced mass.
01200	M2B = reduced mass.
01210	VA = the lattice constant cubed divided by 4.
01220	WL1 = longitudinal optical (LO) phonon frequency (HgTe), $k_B \theta_{\ell_1} / \hbar$, where θ_{ℓ_1} = LO phonon temperature.
01230	WL2 = longitudinal optical phonon frequency (CdTe), $k_B \theta_{\ell_2} / \hbar$, where θ_{ℓ_2} = LO phonon temperature.
01280	EG = E_g (ergs) as a function of x and T (temperature).
01285	P = momentum matrix element coupling conduction and valence bands (eV-cm) as a function of x.
01290	DELTA = E_g divided by the spin-orbit splitting.
01330	SECULAR = an external program for finding the limit $E = E(k)$ at the zone boundary.
01370	$CON = \frac{2e^2}{\pi} \left(\frac{2\mu' m_0}{\hbar^2} \right)^{3/2} \left(\frac{k_B T}{\beta} \right)^{1/2}$, a factor that enters into Fermi-Thomas momenta expressions, i.e., $(k_{FT}^e)^2$, $(k_{FT}^{\ell h})^2$, and $(k_{FT}^{hh})^2$.
01780	SIMP = an external program for evaluating integrals.
01790	KFTE2 = electron Fermi-Thomas momentum.
01810	KFTLH2 = light-hole Fermi-Thomas momentum.
01820	KFTHH2 = heavy-hole Fermi-Thomas momentum.
01840	THETA1 = θ_{ℓ_1} / T (see line no. 01220).
01850	THETA2 = θ_{ℓ_2} / T (see line no. 01230).
01860	GINF2 = g_{∞}^2 , a parameter involving Fermi-Thomas momenta.
01870	GO2 = g_0^2 , a parameter involving Fermi-Thomas momenta.
01890	A1 = longitudinal optical (LO) phonon scattering contribution.
01910	A2 = acoustic phonon (ac) scattering contribution.
01930	A3 = ionized impurity (ii) scattering contribution.
01950	A4 = electron-hole (eh) scattering contribution.
01960	A5 = disorder scattering (dis.) contribution.
01980	NP1 = phonon occupation number.
01990	NP2 = phonon occupation number.
02150	Q1 = \mathcal{L}_1 (matrix element).
02160	Q2 = \mathcal{L}_2 (matrix element).

GP03-0750-84

Line no.	Comments
02170	$Q3 = \mathcal{L}_3$ (matrix element).
02200	$QL1 = (\mathcal{L}, l)_1$ (matrix element).
02210	$QL2 = (\mathcal{L}, l)_2$ (matrix element).
02260	SIGMA = conductivity.
02270	UH = Hall mobility.
02280	EGOPT = $k_B T / \text{BETA}$.

GP03-0750-65

B.2 Description of Symbols - Subroutine Programs

ORIGINAL PAGE IS
OF POOR QUALITY

Line no.	Comments
A.	SECULAR - The program used to find the roots (E_1, E_2, E_3) of the cubic secular equation describing the conduction band, light-hole band, and split-off valence band.
02520	CUBE - A subroutine for finding the roots of a cubic equation $x^3 + c_2x^2 + c_1x + c_0 = 0$.
B.	FUNC - The program used to find the carrier concentration (electrons, light-holes, and heavy-holes) as a function of temperature.
02700	SIMP - A subroutine used for evaluating a certain class of integrals.
02710	NE = electron concentration.
02780	NLH = light-hole concentration.
02800	NHH = heavy-hole concentration.
C.	FV - The program used to obtain the Fermi distribution function
D.	FUNC1 - The program used to obtain the product FV and LAMDA.
03000	LAMDA - A function used to calculate the conduction band density-of-states.
E.	FUNC2 - The program used to obtain the product of FV and LAMDAV.
03080	LAMDAV - A function used to calculate the light-hole density-of-states.
F.	FVP - This program evaluates the function $\exp(y+z)/[\exp(y+z)+1]^2$.
G.	FUNC3 - This program evaluates the function $\lambda_c \exp(y-z)/[\exp(y-z)+1]^2$.
H.	FUNC4 - This program evaluates the function $\lambda_{lh} \exp(y-z)/[\exp(y-z)+1]^2$.
I.	LAMDA = λ_c , an expression used in calculating the conduction-band density-of-states.
J.	LAMDAV = λ_{lh} , an expression used in calculating the light-hole density-of-states.
K.	S - This program evaluates a function used in determining the crystal momentum.
L.	L1 - This program evaluates $L^{(n)}$.
N.	NABC - This program evaluates the function $F_\lambda(y)$, which appears in the LO-phonon scattering operator \mathcal{L}_{LO} .
O.	RSL - This program evaluates functions appearing in the LO-phonon scattering operator.
04390	ROP1 = $\rho_0^+(y, \theta_1)$
04410	ROP2 = $\rho_0^+(y, \theta_2)$
04440	ROM1 = $\rho_0^-(y, \theta_1)$
04470	ROM2 = $\rho_0^-(y, \theta_2)$
04530	R1P1 = $\rho_1^+(y, \theta_1)$
04540	R2P1 = $\rho_2^+(y, \theta_1)$
04590	R1P2 = $\rho_1^+(y, \theta_2)$
04600	R2P2 = $\rho_2^+(y, \theta_2)$
04660	R1M1 = $\rho_1^-(y, \theta_1)$
04670	R2M1 = $\rho_2^-(y, \theta_1)$
04730	R1M2 = $\rho_1^-(y, \theta_2)$

QP03-0750-06

Line no.	Comments
04740	$R2M2 = \rho_2^-(y, \theta_2)$
04760	$SY2 = s^2$
04770	$Q1P = q_1^+$
04780	$Q2P = q_2^+$
04800	$Q1M = q_1^-$
04820	$Q2M = q_2^-$
04840	$P1P = P_1^+$
04850	$P2P = P_2^+$
04870	$P1M = P_1^-$
04890	$P2M = P_2^-$
04910	$V1P = r_1^+$
04920	$V2P = r_2^+$
04940	$V1M = r_1^-$
04960	$V2M = r_2^-$
05000	$V0P1 = V_0^+(y, \theta_1)$
05010	$V1P1 = V_1^+(y, \theta_1)$
05020	$V2P1 = V_2^+(y, \theta_1)$
05040	$V3P1 = V_3^+(y, \theta_1)$
05090	$V0P2 = V_0^+(y, \theta_2)$
05100	$V1P2 = V_1^+(y, \theta_2)$
05110	$V2P2 = V_2^+(y, \theta_2)$
05130	$V3P3 = V_3^+(y, \theta_2)$
05190	$V0M1 = V_0^-(y, \theta_1)$
05200	$V1M1 = V_1^-(y, \theta_1)$
05210	$V2M1 = V_2^-(y, \theta_1)$
05230	$V3M1 = V_3^-(y, \theta_1)$
05290	$V0M2 = V_0^-(y, \theta_2)$
05300	$V1M2 = V_1^-(y, \theta_2)$
05310	$V2M2 = V_2^-(y, \theta_2)$
05330	$V3M2 = V_3^-(y, \theta_2)$
05390	$RP1 = R_+(y, \theta_1)$
05400	$SP1 = S_+(y, \theta_1)$
05430	$RP2 = R_+(y, \theta_2)$
05440	$SP2 = S_+(y, \theta_2)$
05480	$RM1 = R_-(y, \theta_1)$

ORIGINAL PAGE IS
OF POOR QUALITY

GP03-0750-07

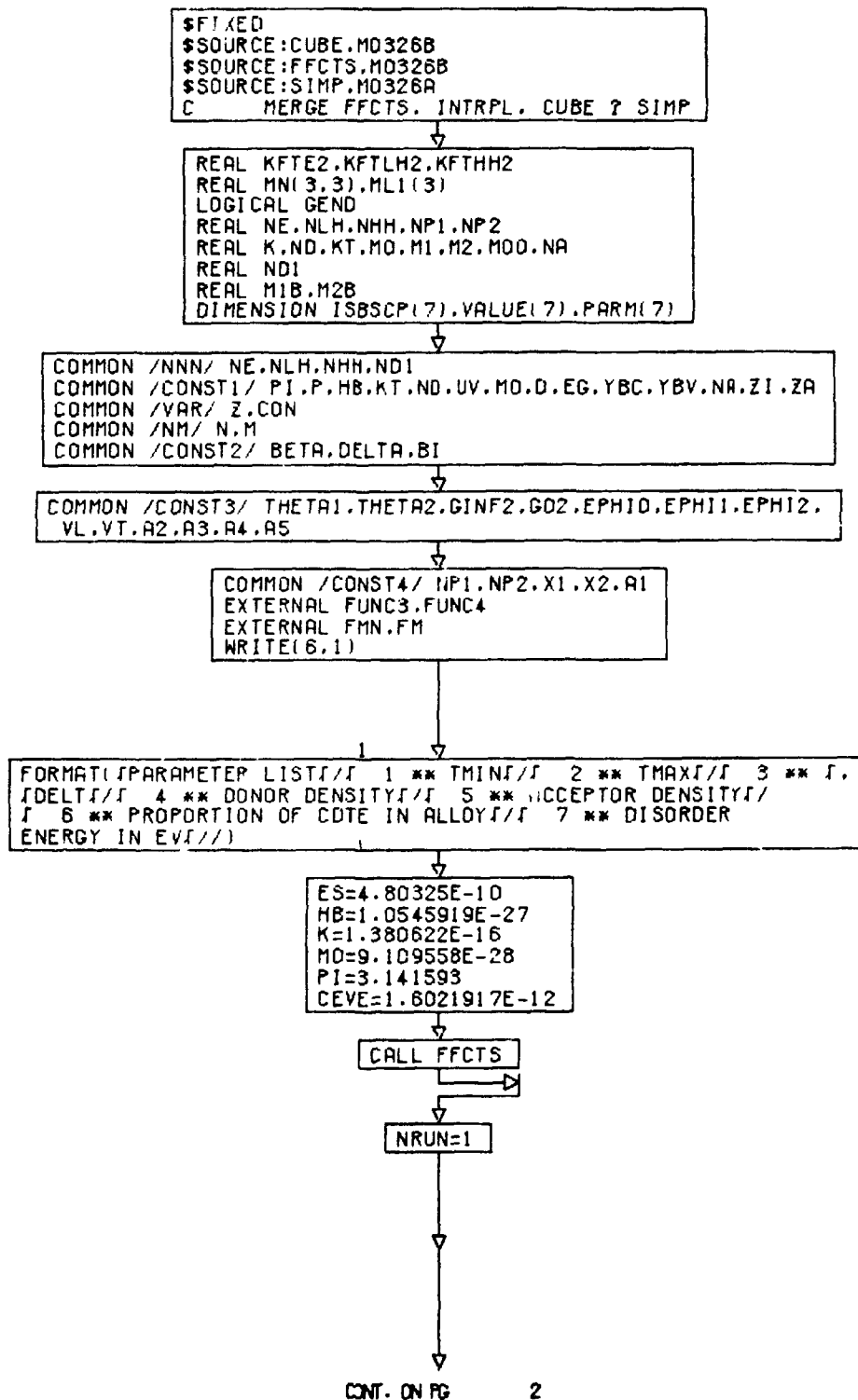
Line No.	Comments
05490	SM1 = S ₋ (y, θ_1)
05560	RM2 = R ₋ (y, θ_2)
05570	SM2 = S ₋ (y, θ_2)
05620	PI0 = π_0 (y)
05640	PI2 = π_2 (y)
05690	PHI0 = ϕ_0 (y)
05710	PHI1 = ϕ_1 (y)
05730	PHI2 = ϕ_2 (y)
05770	PHI = Φ
05810	A1 = A ₁ (y)
05820	A2 = A ₂ (y)
05830	A3 = A ₃ (y)
05840	A4 = A ₄ (y)
05850	B1 = B ₁ (y)
05880	B2 = B ₂ (y)
05890	B3 = B ₃ (y)
05900	B4 = B ₄ (y)
05910	B5 = B ₅ (y)
05930	B6 = B ₆ (y)
05940	FLY = F _L (y)
05960	FTY = F _T (y)
06010	LB = L _B (y)
P.	ROOT - This program calculates limits.
Q.	INTEG - This program evaluates integrals.
R.	FMN - This program calculates the elements of the determinant F _{mn} (y).
S.	FM - This program evaluates a function involving FVP and L1.
T.	HCSPOL - This program calculates as a function of x, the TO and LO phonon temperature, the transverse effective charges, the Callen effective charges, and the dielectric constants ϵ_0 and ϵ_∞ .
07520	ESTR1 = HgTe transverse charge.
07530	ESTR2 = CdTe transverse charge.
07531	XM1 = HgTe reduced mass in g.
07532	XM2 = CdTe reduced mass in g.
07533	A = lattice constant as a function of x.
07540	EPS1 = ϵ_∞ as a function of x.
07550	EPS0 = ϵ_0 as a function of x.

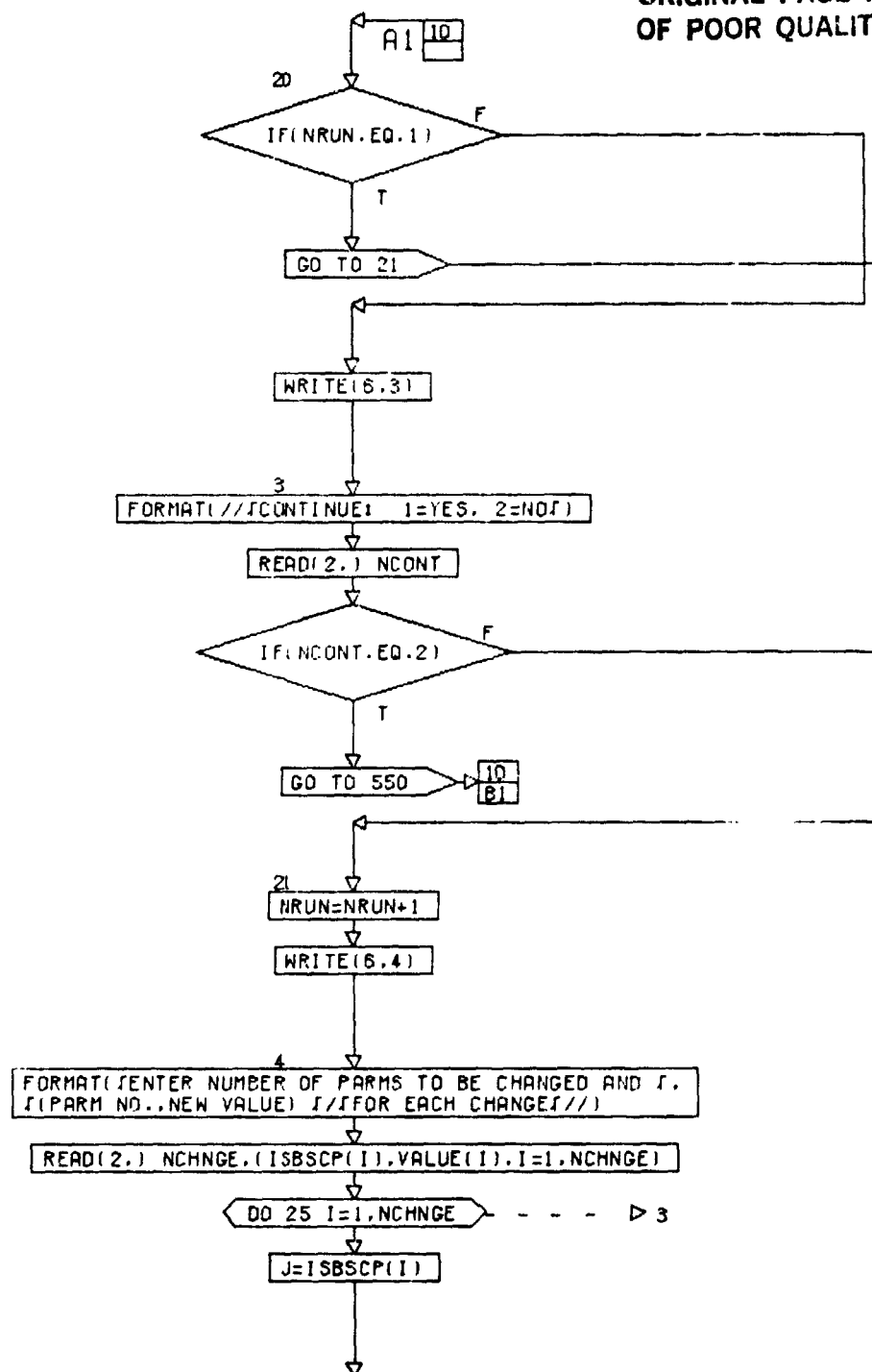
GP03-0750-88

Line No.	Comments
07560	WT2 = ω_T (CdTe) as a function of x.
07570	WT1 = ω_T (HgTe) as a function of x.
07630	THT1 = HgTe TO - phonon temperature.
07640	THT2 = CdTe TO - phonon temperature.
07791	THL1 = HgTe LO - phonon temperature.
07782	THL2 = CdTe LO - phonon temperature
07860	EC1 = Callen effective charge for HgTe.
07870	EC2 = Callen effective charge for CdTe.

GP03-0750-69

B.3 Computer Program Flow Charts



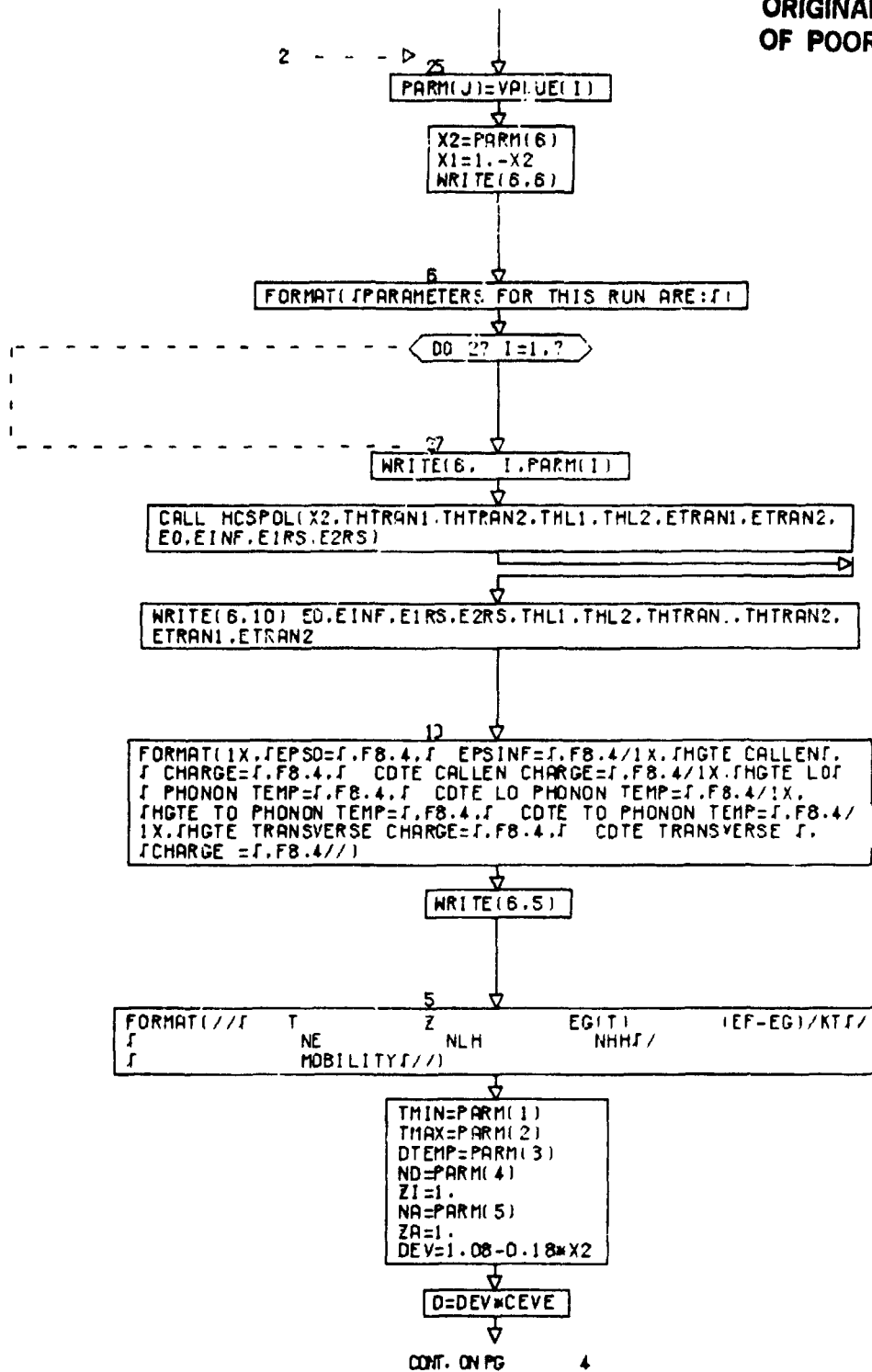


CONT. ON PG 3

PG 2 OF 10

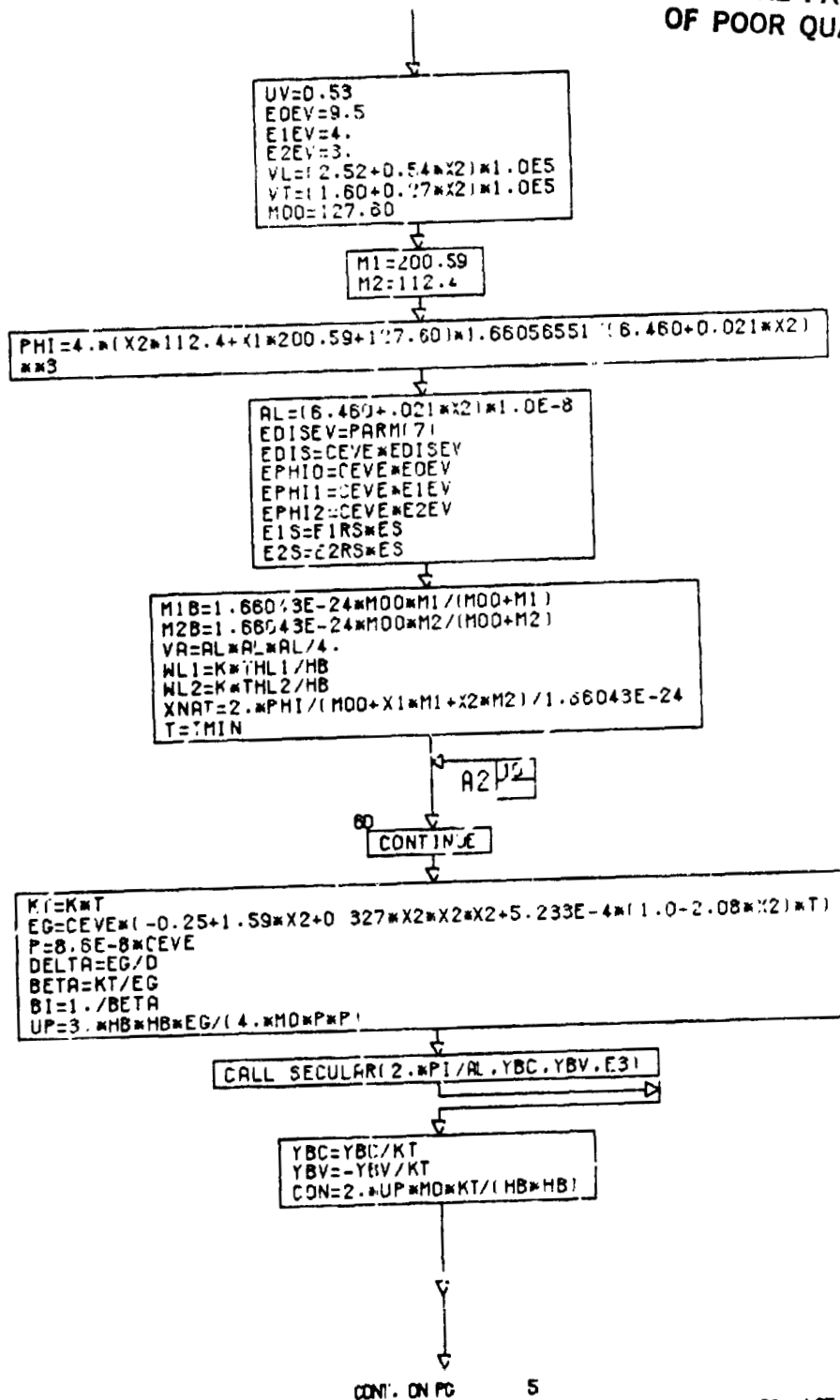


ORIGINAL PAGE IS
OF POOR QUALITY

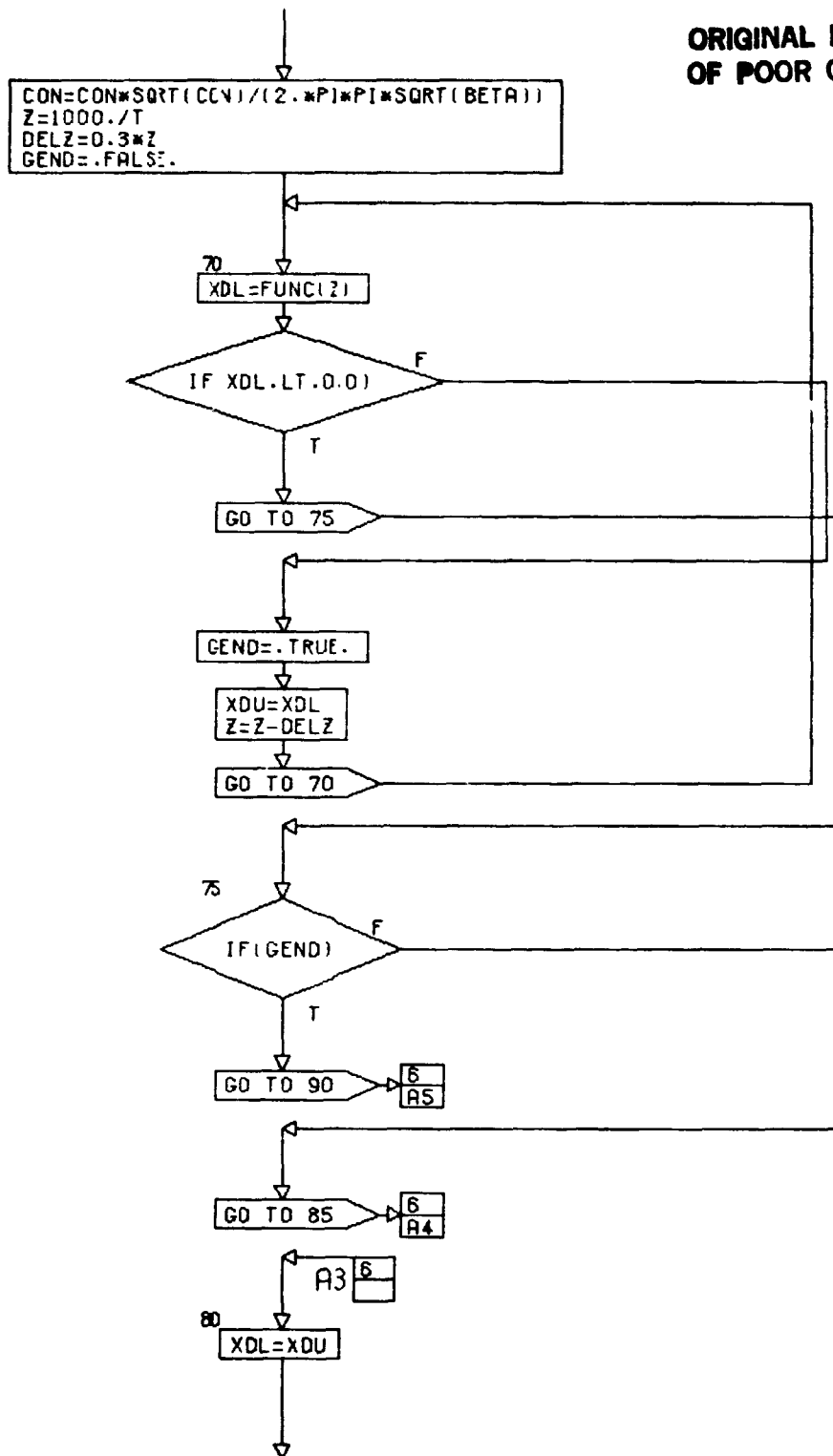


PG 3 OF 10

ORIGINAL PAGE IS
OF POOR QUALITY



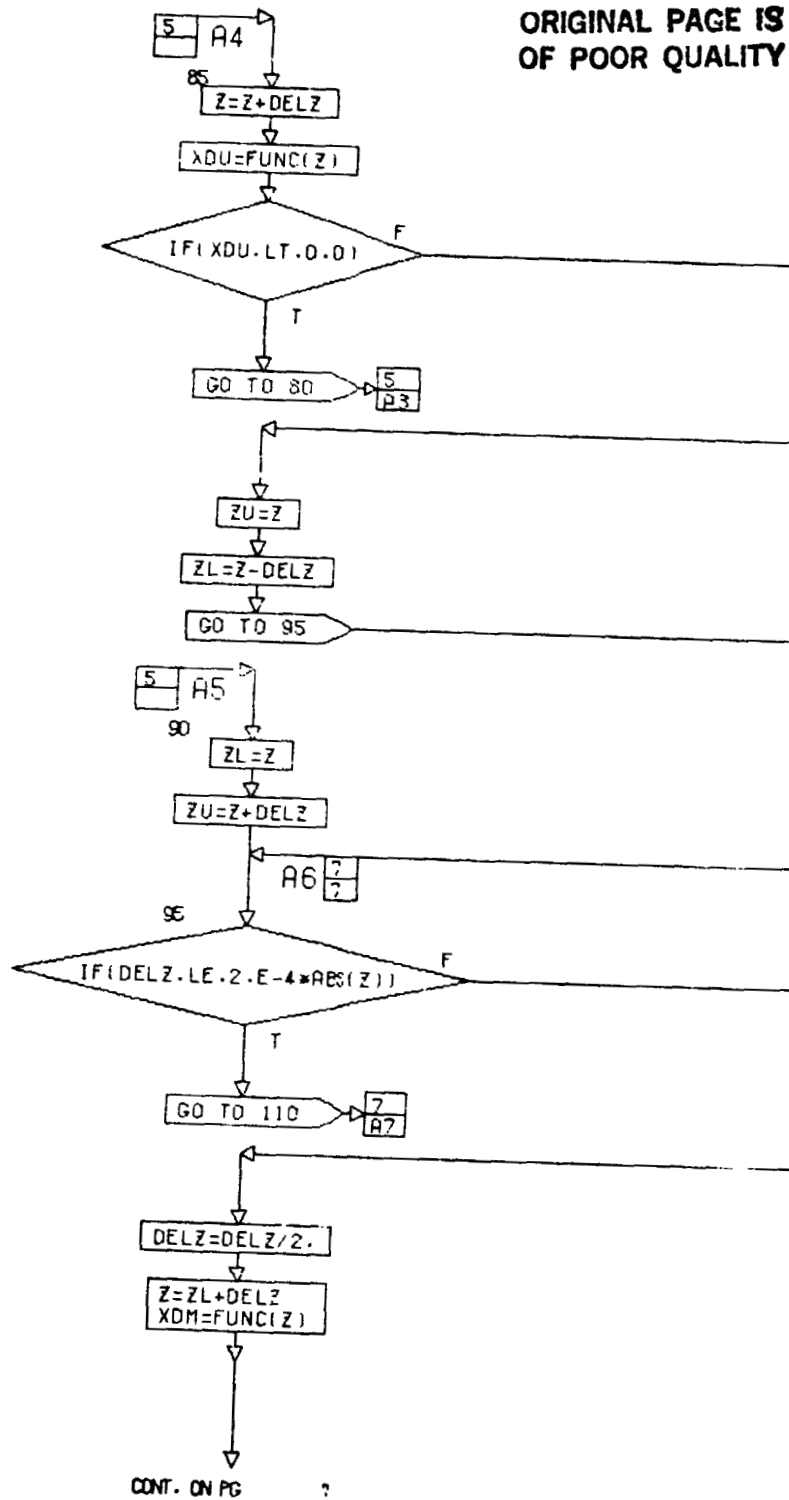
ORIGINAL PAGE IS
OF POOR QUALITY



CONT. ON PG 6

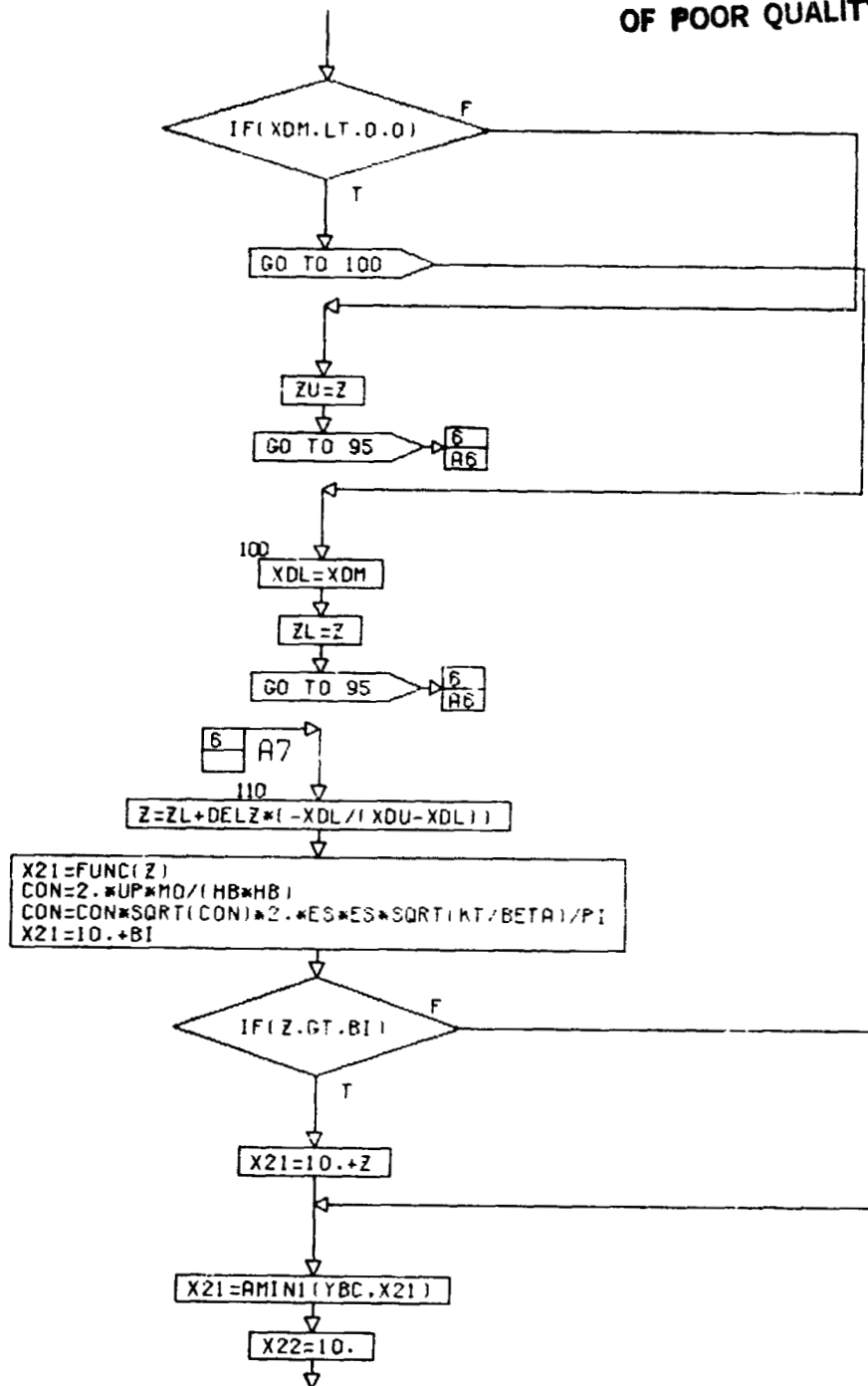
PG 5 OF 10

ORIGINAL PAGE IS
OF POOR QUALITY



PG 6 OF 10

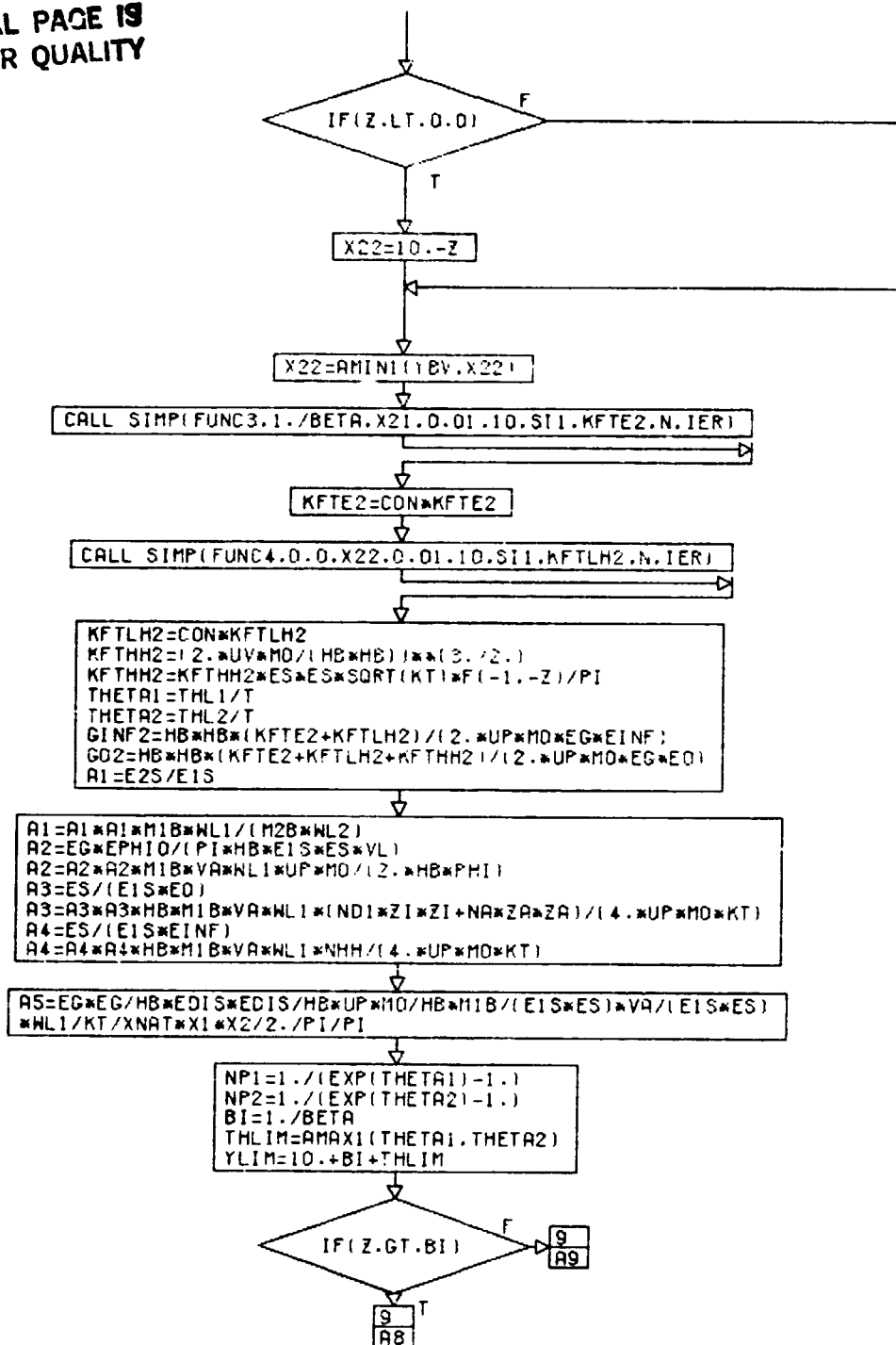
ORIGINAL PAGE 19
OF POOR QUALITY



CONT. ON PG 8

PG 7 OF 10

ORIGINAL PAGE IS
OF POOR QUALITY

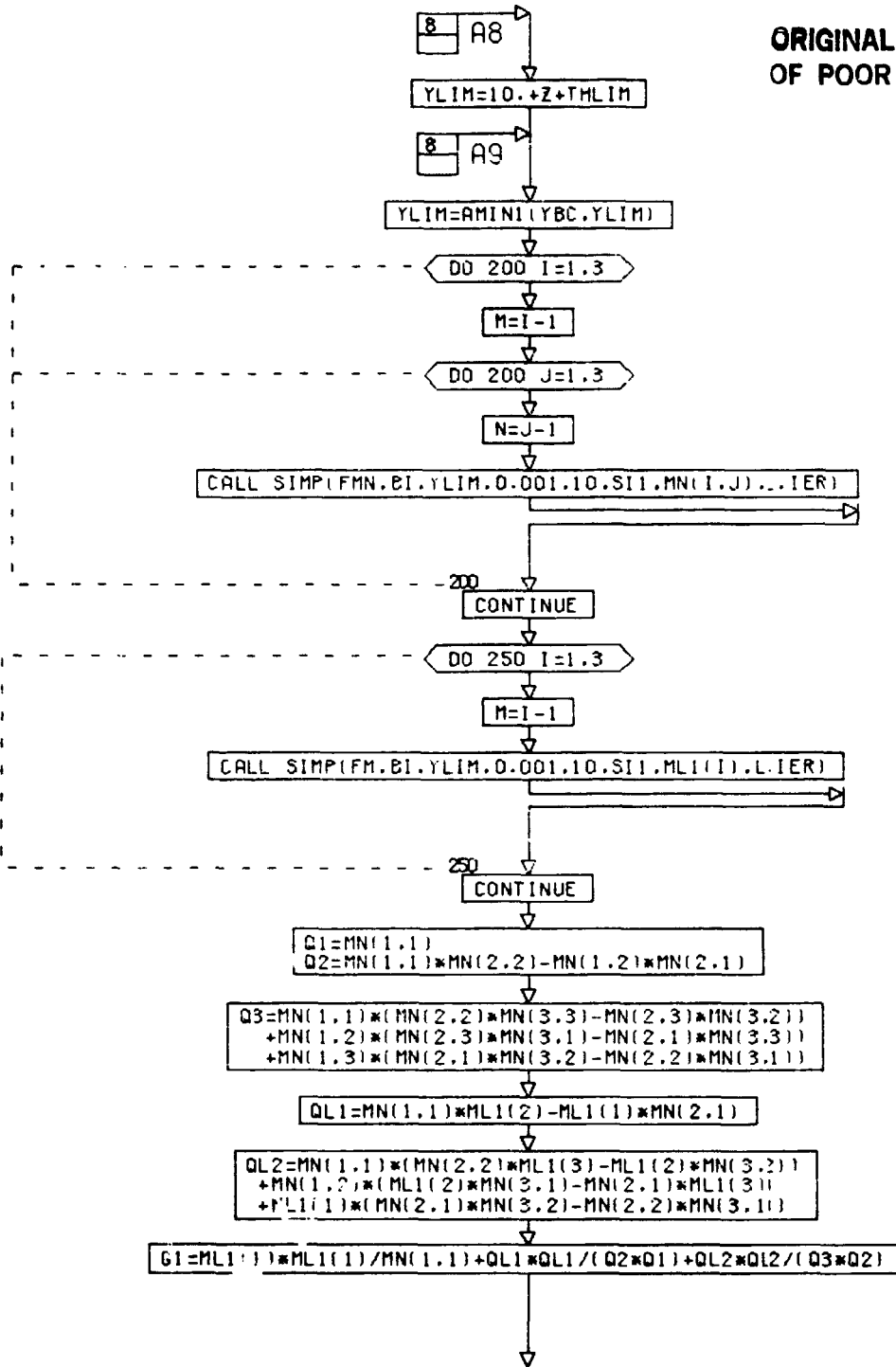


CONT. ON PG

9

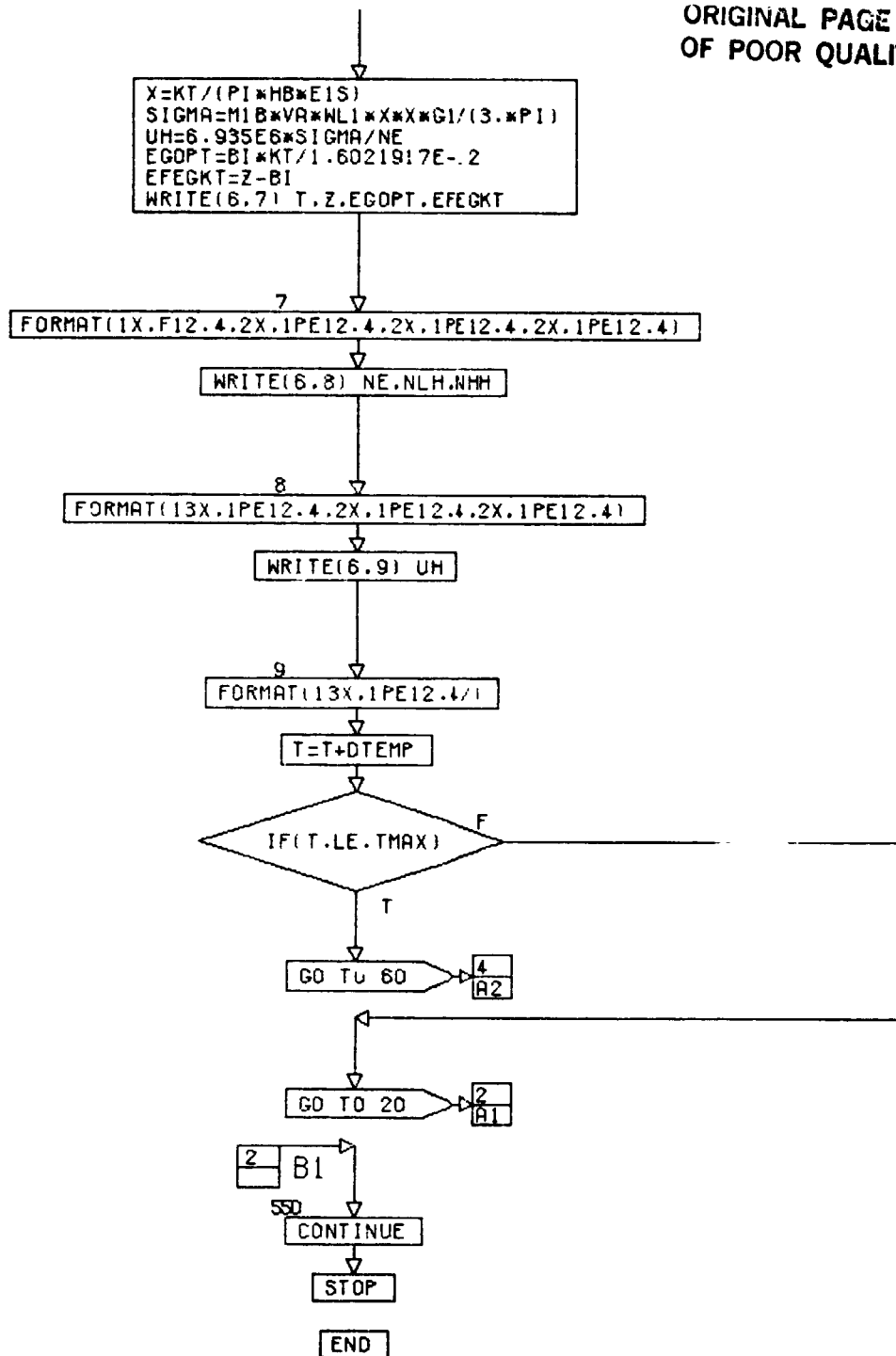
PG 8 OF 10

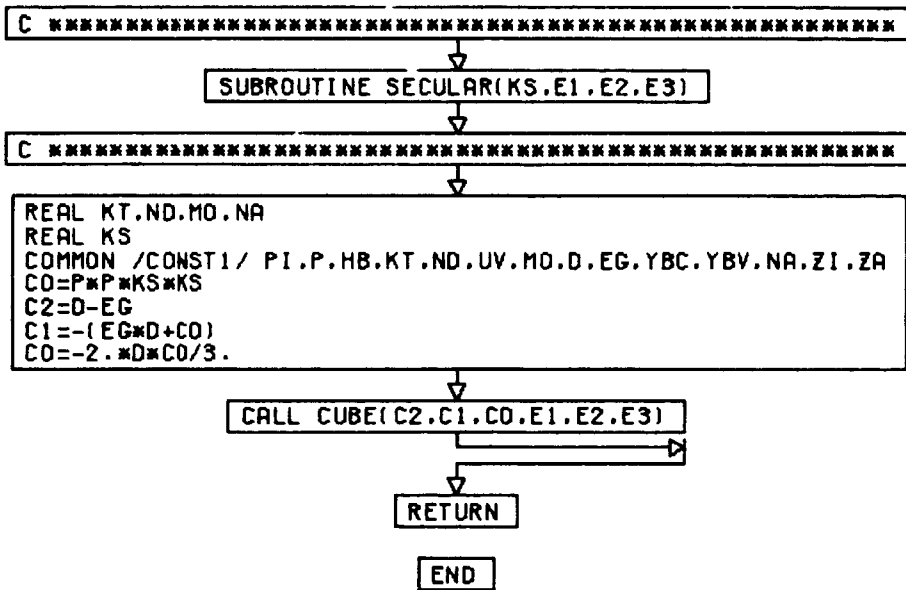
ORIGINAL PAGE IS
OF POOR QUALITY



CONT. ON PG 10

PG 9 OF 10

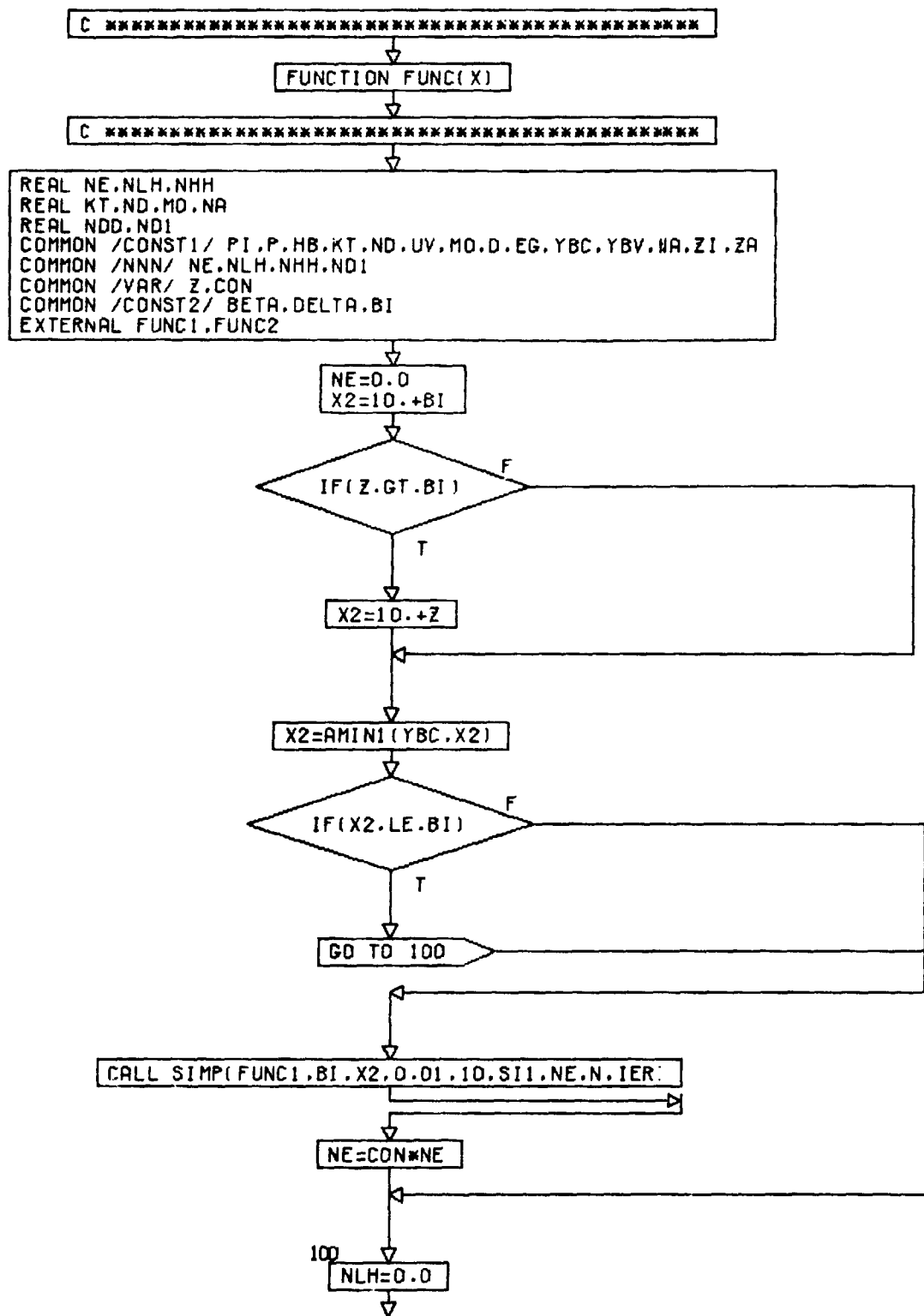




ORIGINAL PAGE IS
OF POOR QUALITY

PG 1 FINI

(+)

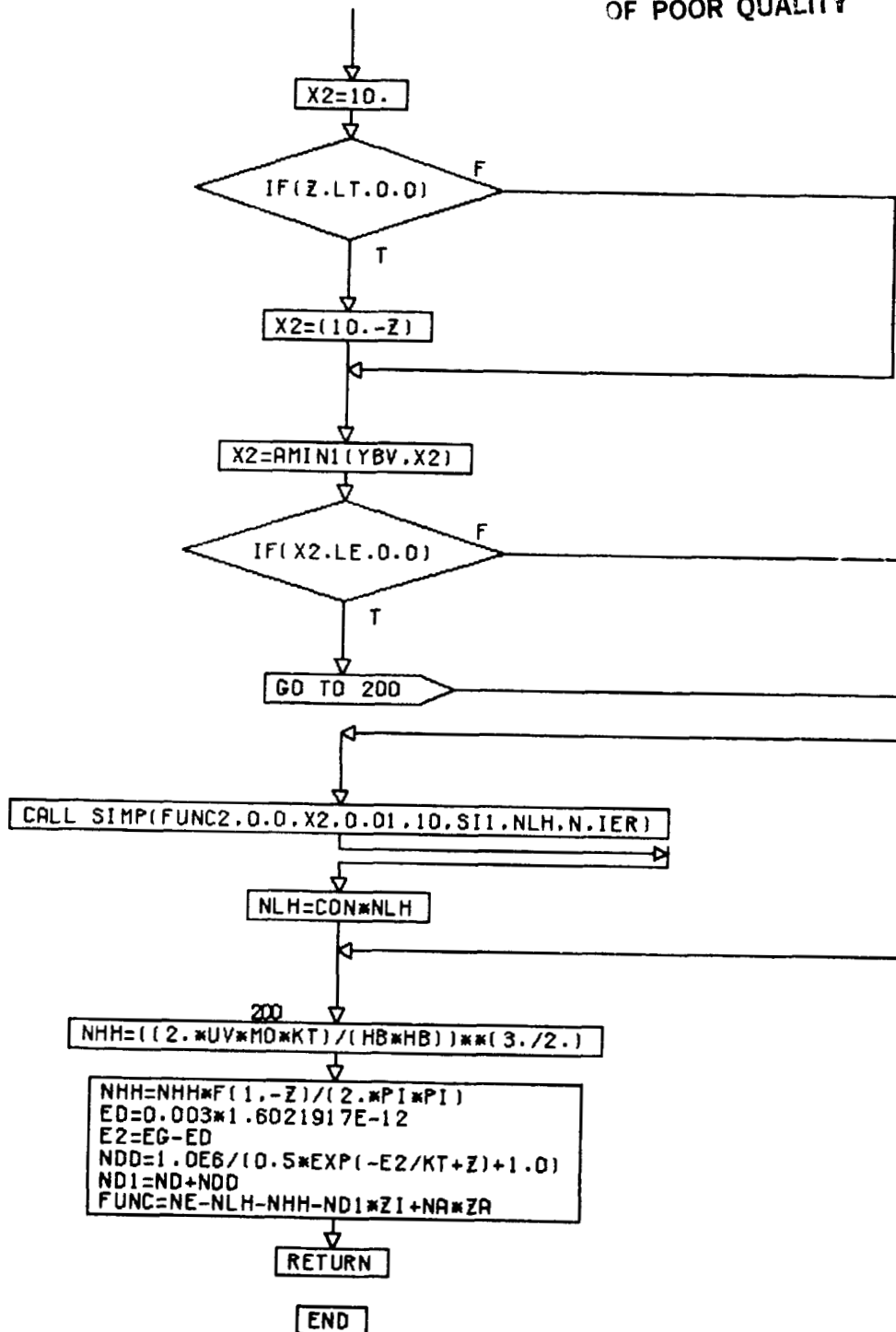


CONT. ON PG

2

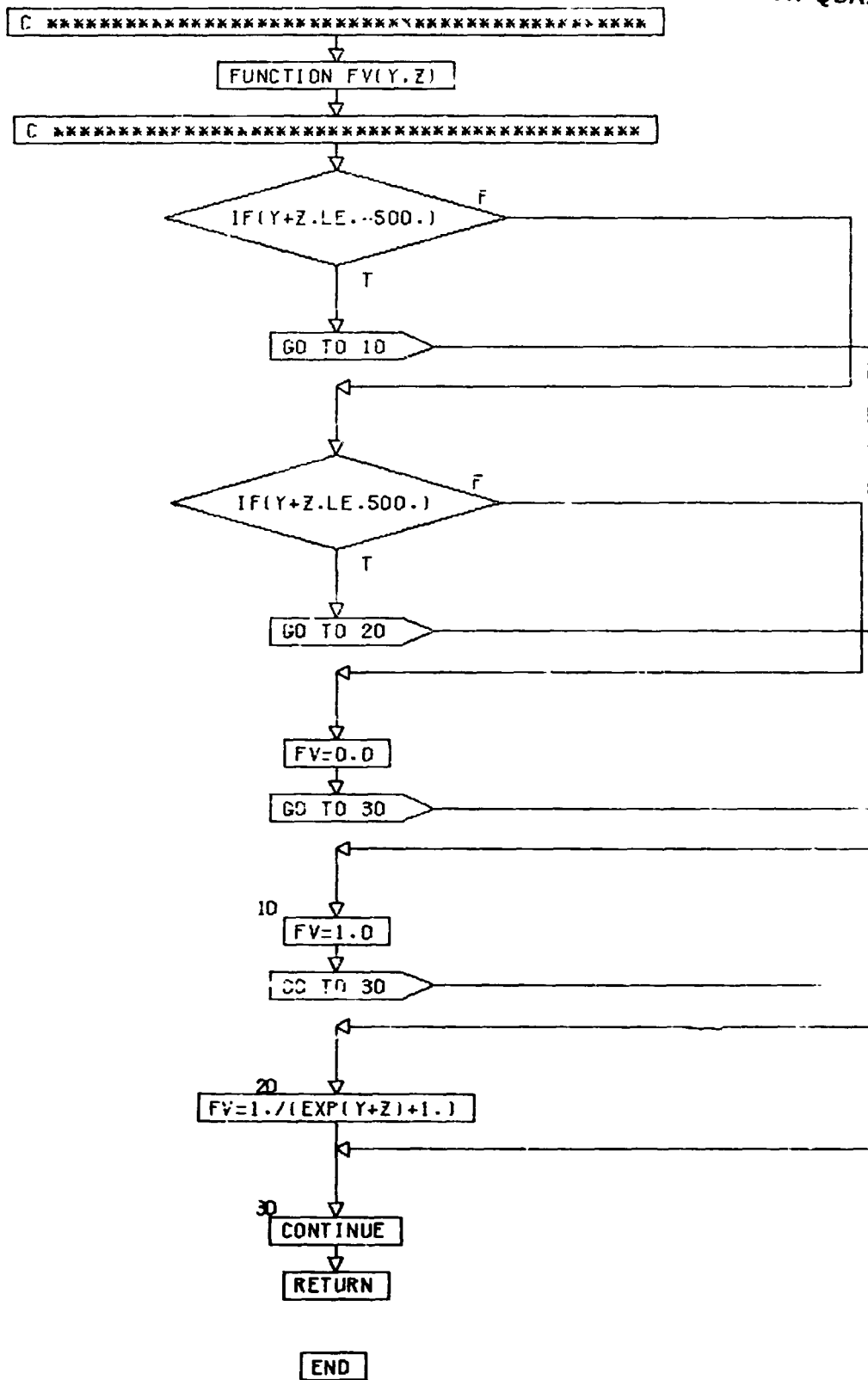
PG 1 OF 2

ORIGINAL PAGE 19
OF POOR QUALITY

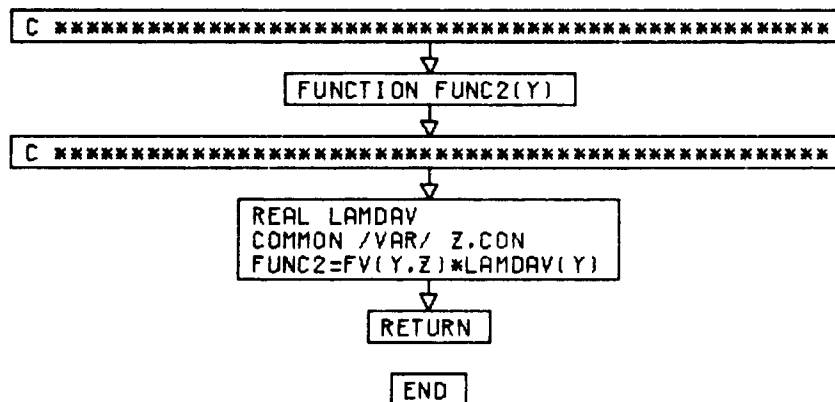
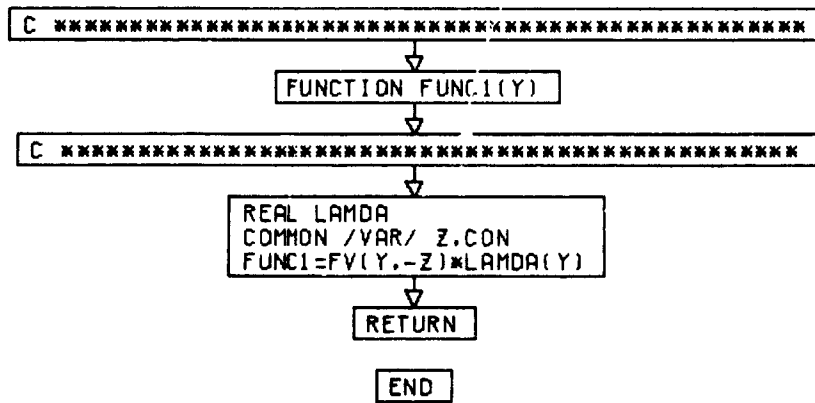


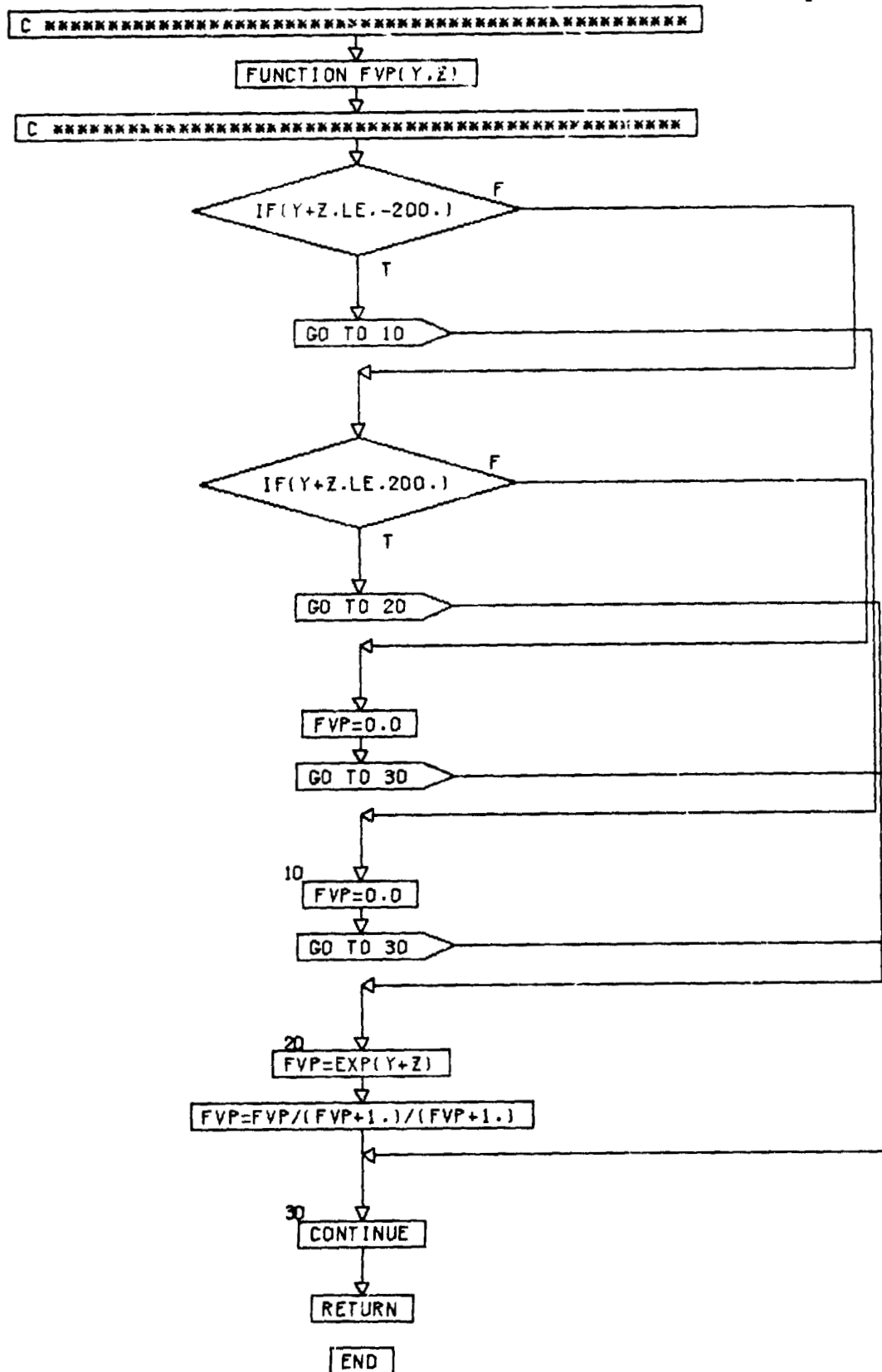
PG 2 FINE

ORIGINAL PAGE IS
OF POOR QUALITY

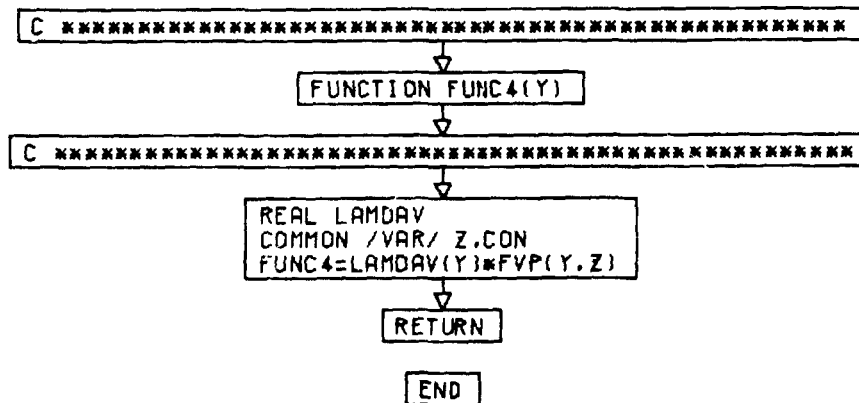
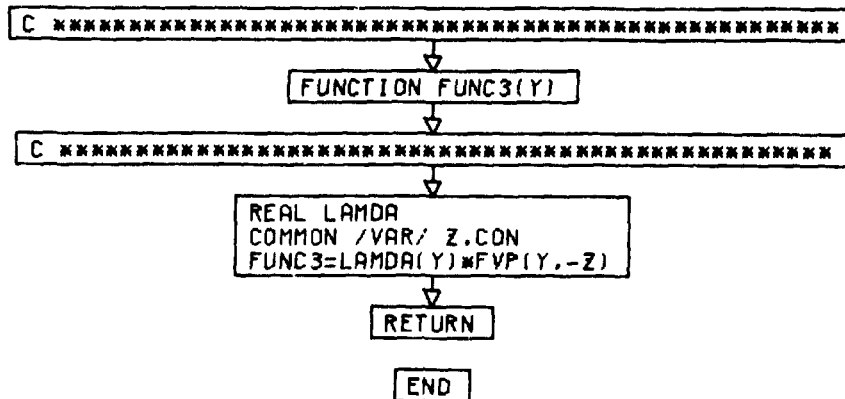


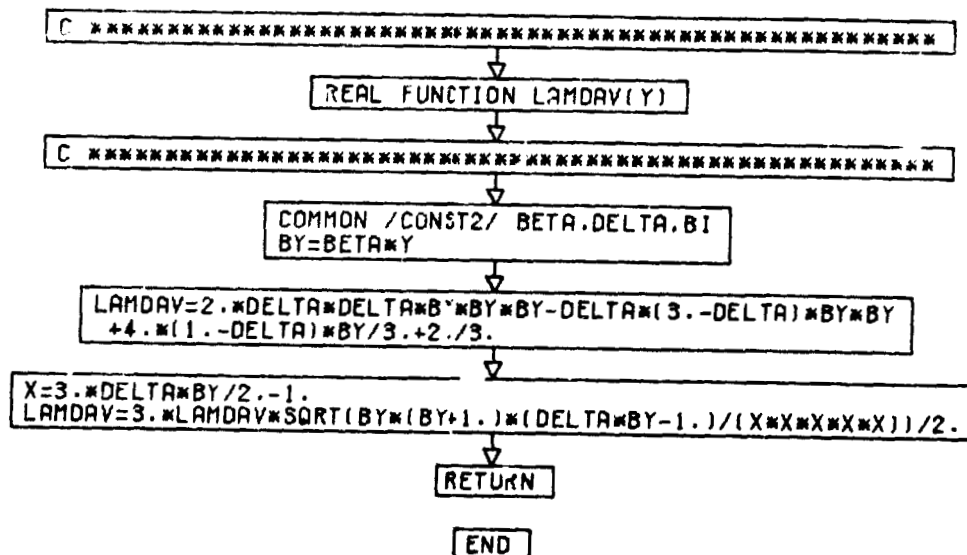
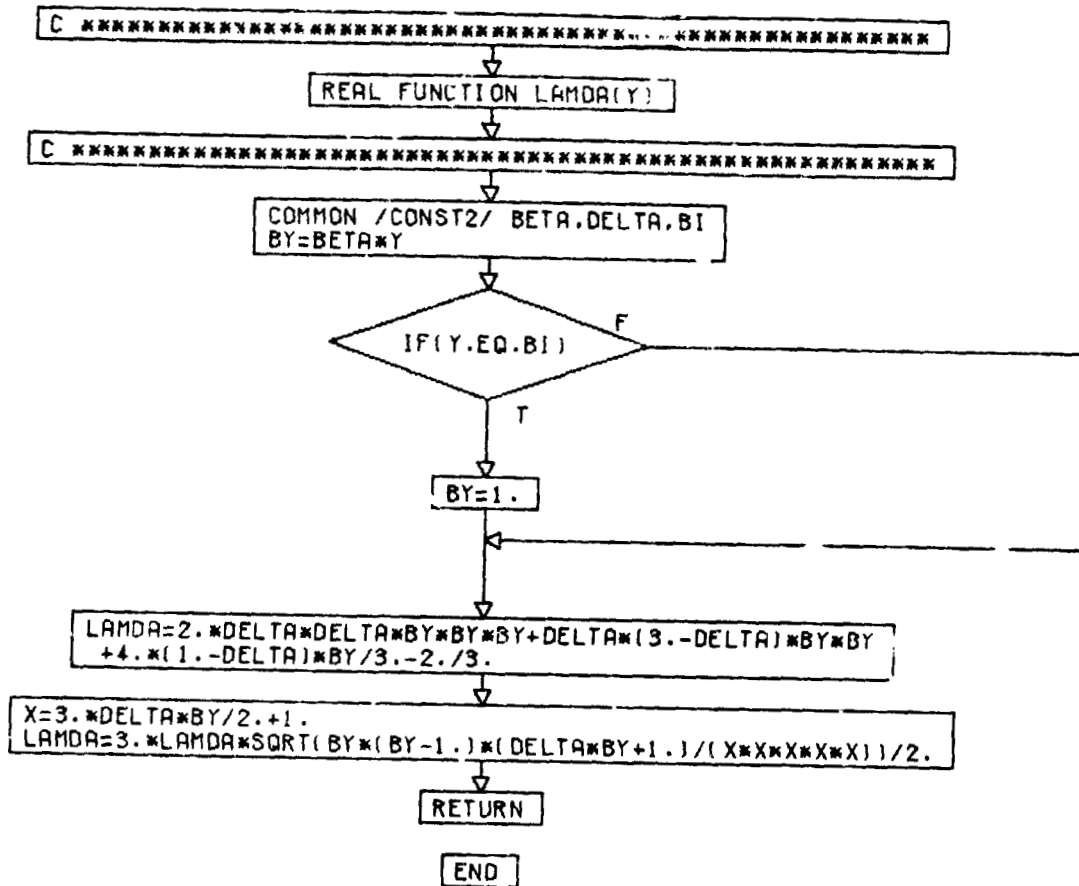
ORIGINAL PAGE IS
OF POOR QUALITY

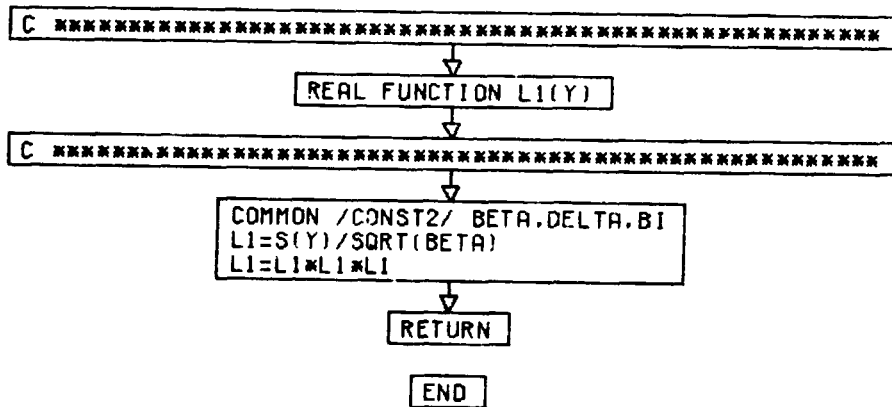
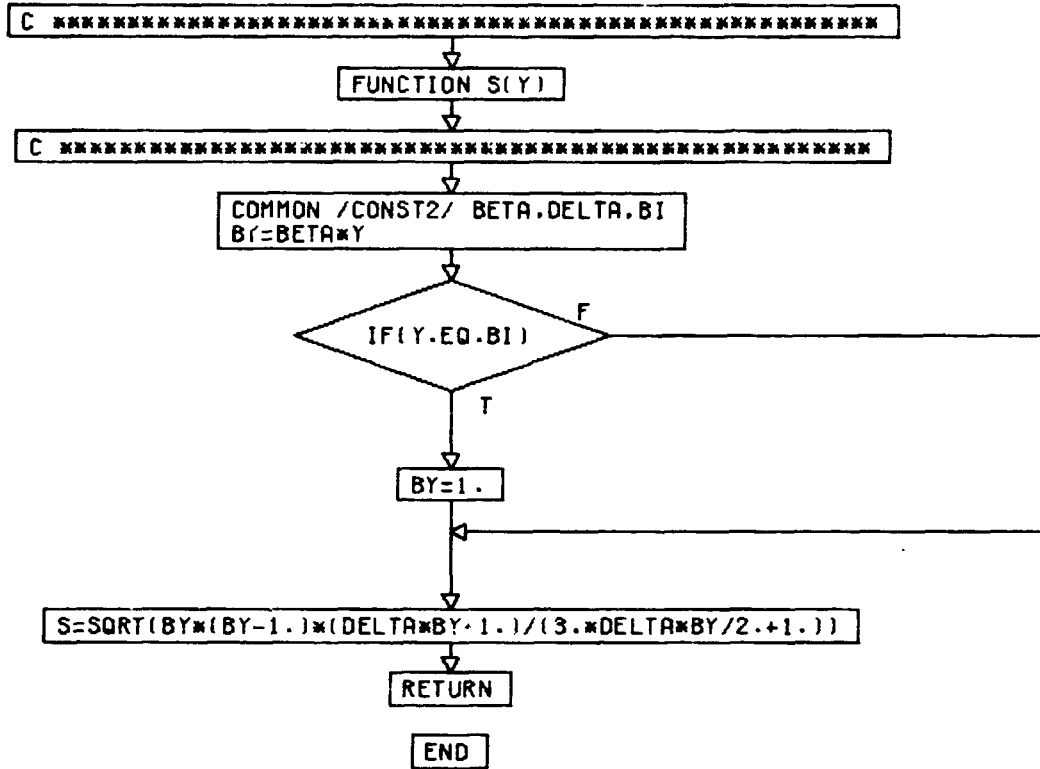




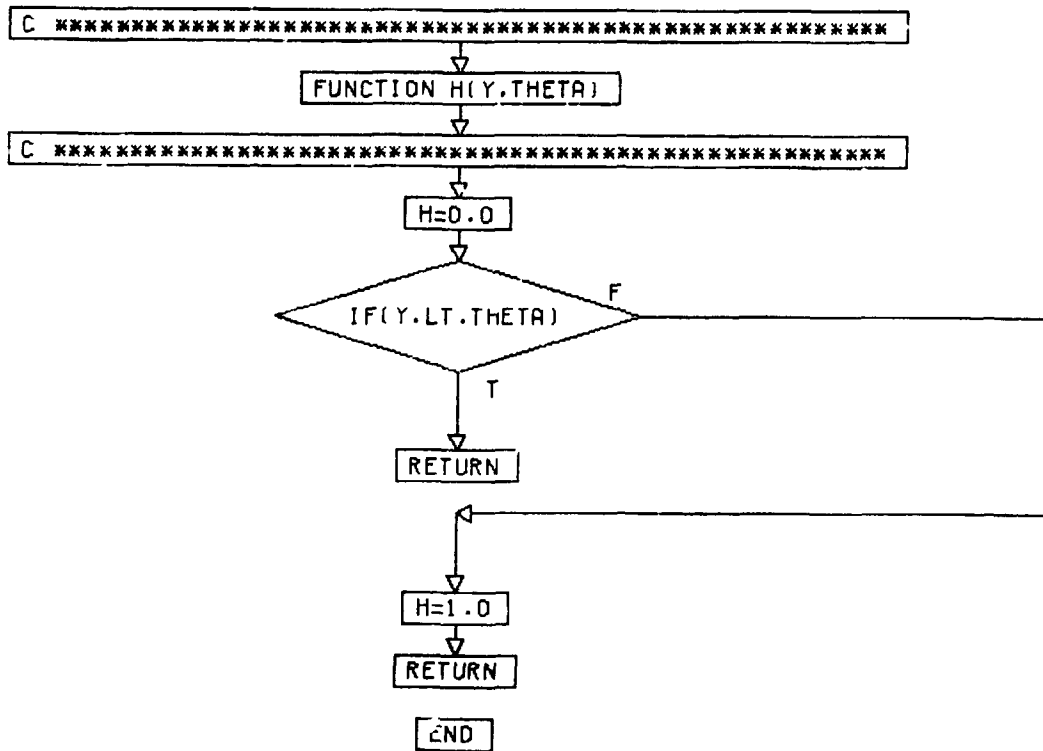
ORIGINAL PAGE IS
OF POOR QUALITY



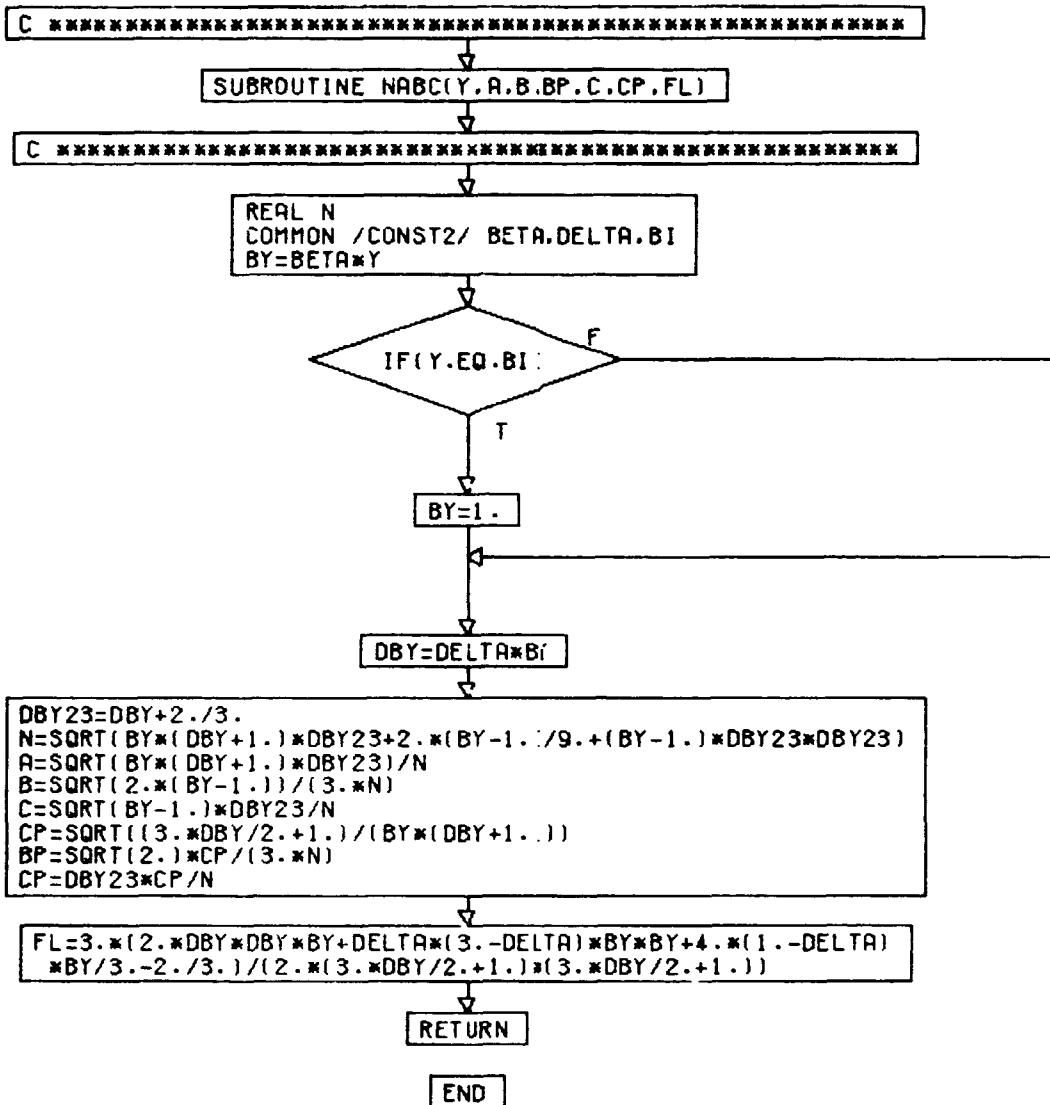




ORIGINAL PAGE IS
OF POOR QUALITY



PG 1. FINE



ORIGINAL PAGE IS
OF POOR QUALITY

PG 1 FINI

C *****

SUBROUTINE RSL(Y,RP1,RP2,RM1,RM2,SP1,SP2,SM1,SM2,LB)

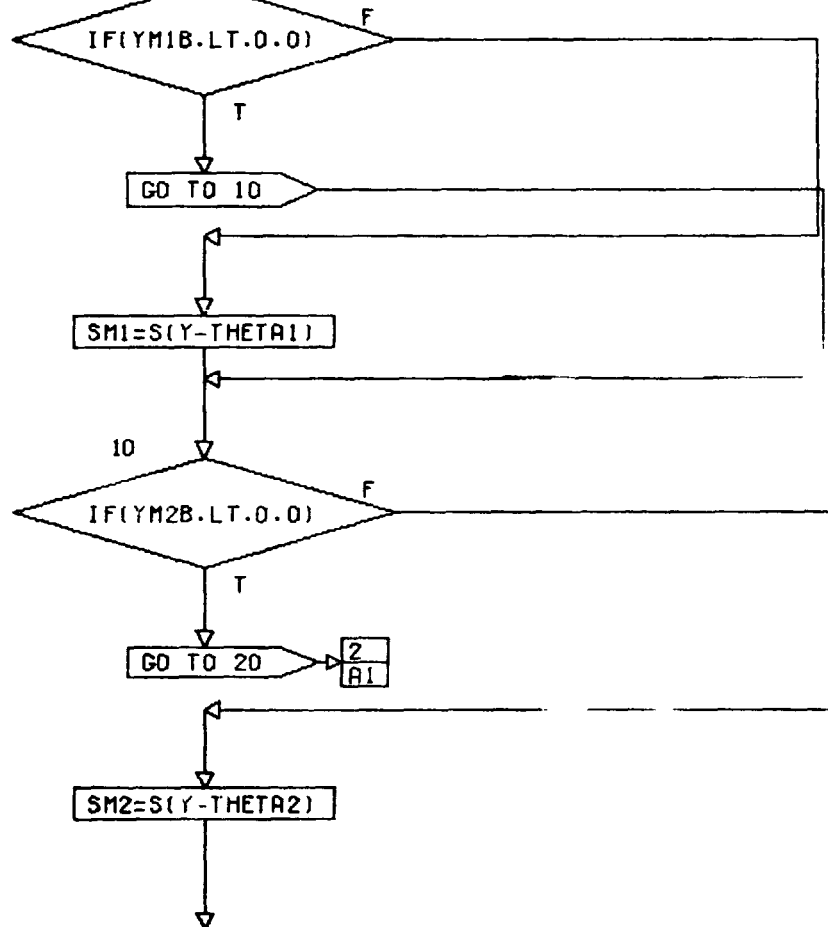
C *****

REAL LAMDA
REAL LB
COMMON /CONST2/ BETA,DELTA,BI

COMMON /CONST3/ THETA1,THETA2,GINF2,G02,EPHI0,EPHI1,EPHI2,
VL,VT,SA2,SA3,SA4,SA5

YM1B=Y-THETA1-BI
YM2B=Y-THETA2-BI
SY=S(Y)
SP1=S(Y+THETA1)
SP2=S(Y+THETA2)

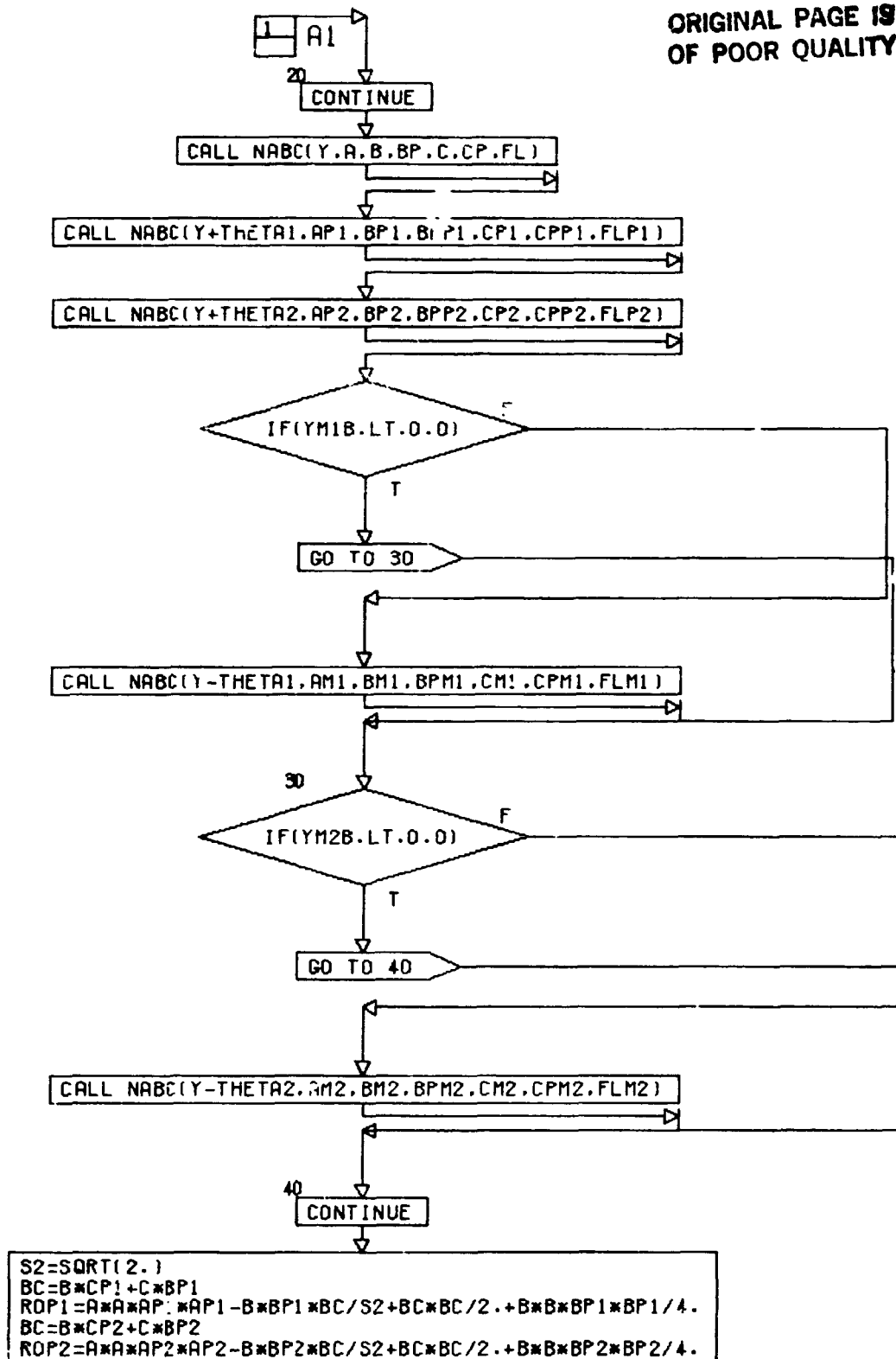
ORIGINAL PAGE IS
OF POOR QUALITY



CONT. ON PG 2

PG 1 OF 11

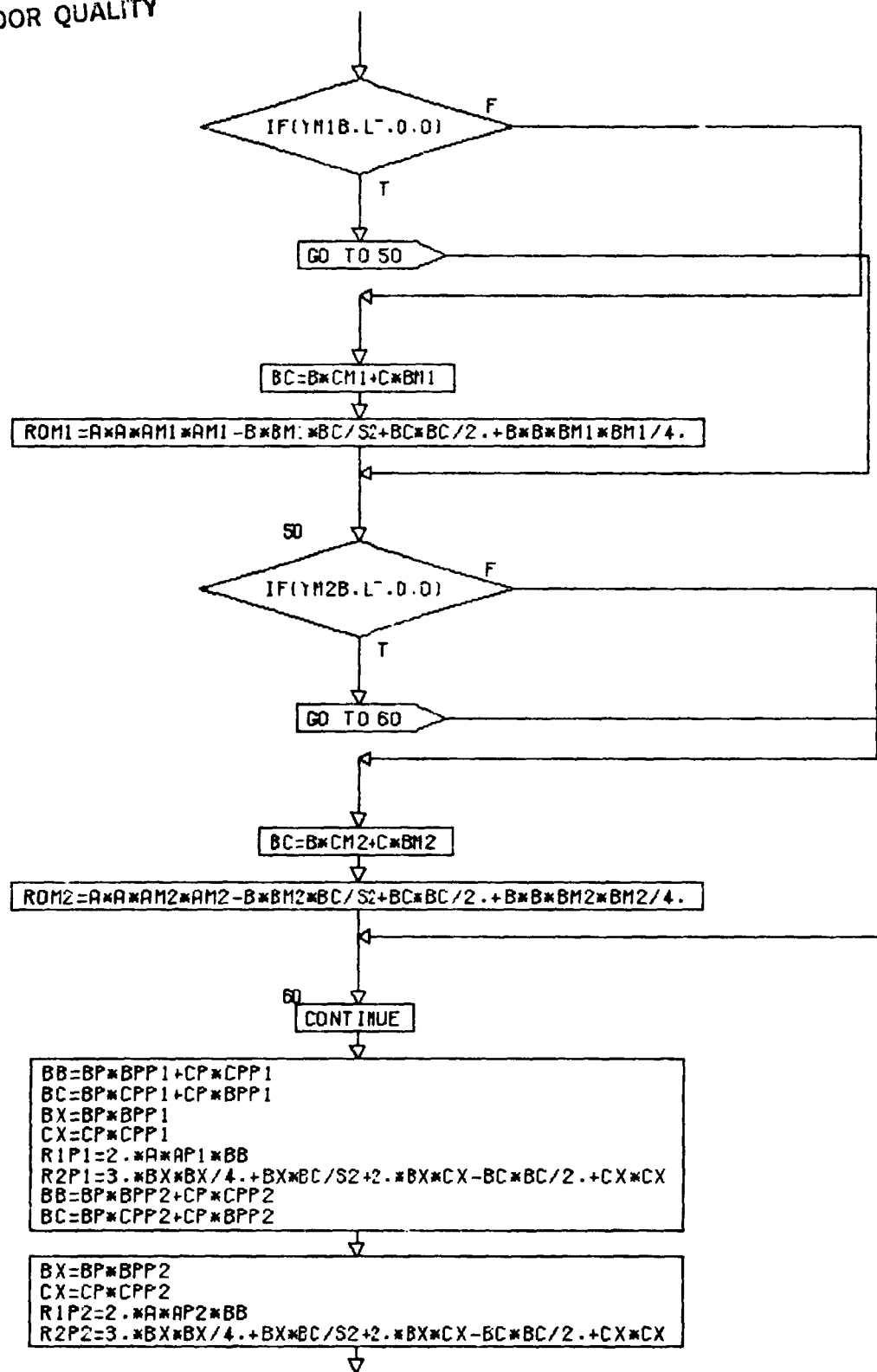
ORIGINAL PAGE 19
OF POOR QUALITY



CONT. ON PG 3

PG 2 OF 11

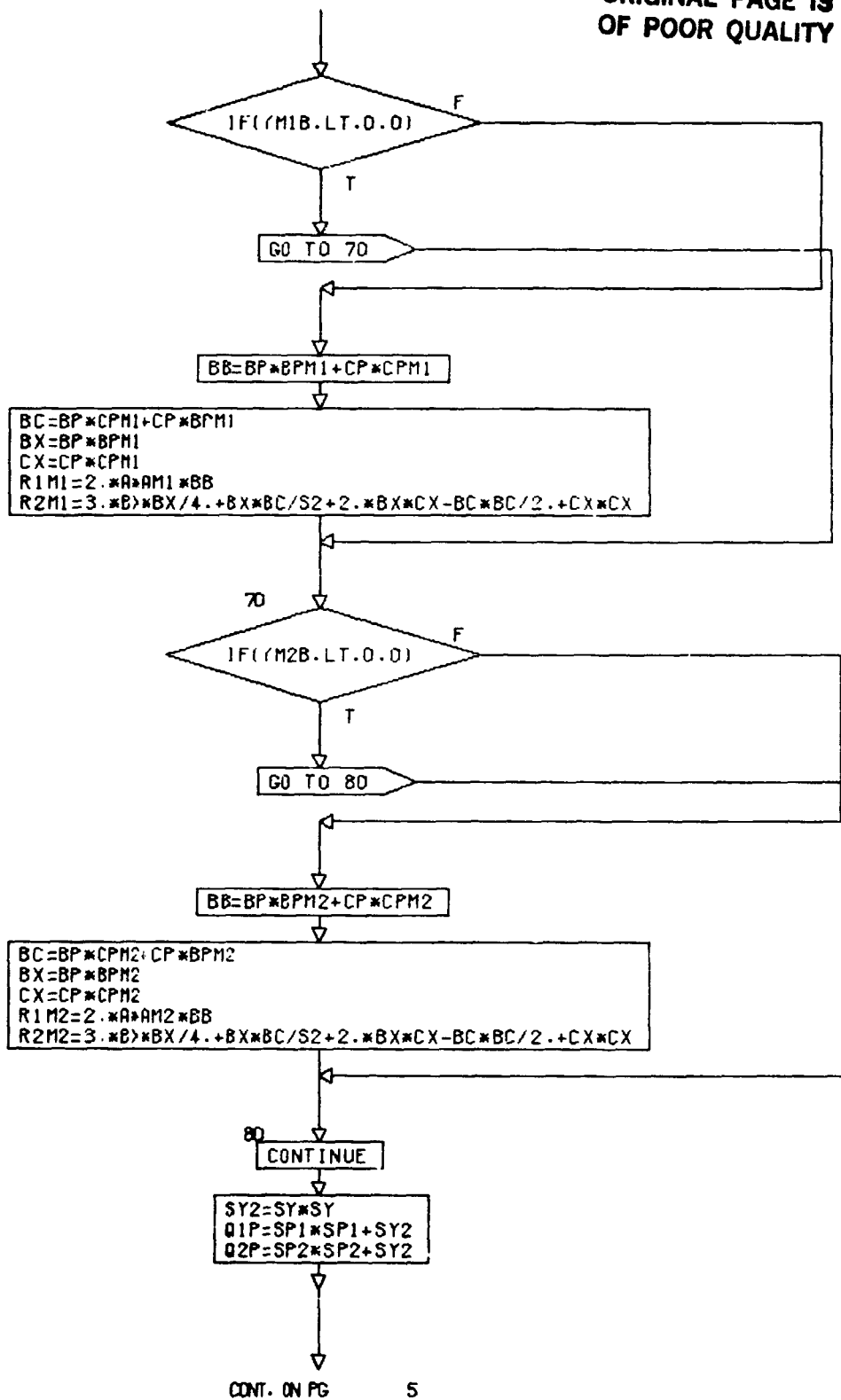
ORIGINAL PAGE IS
OF POOR QUALITY



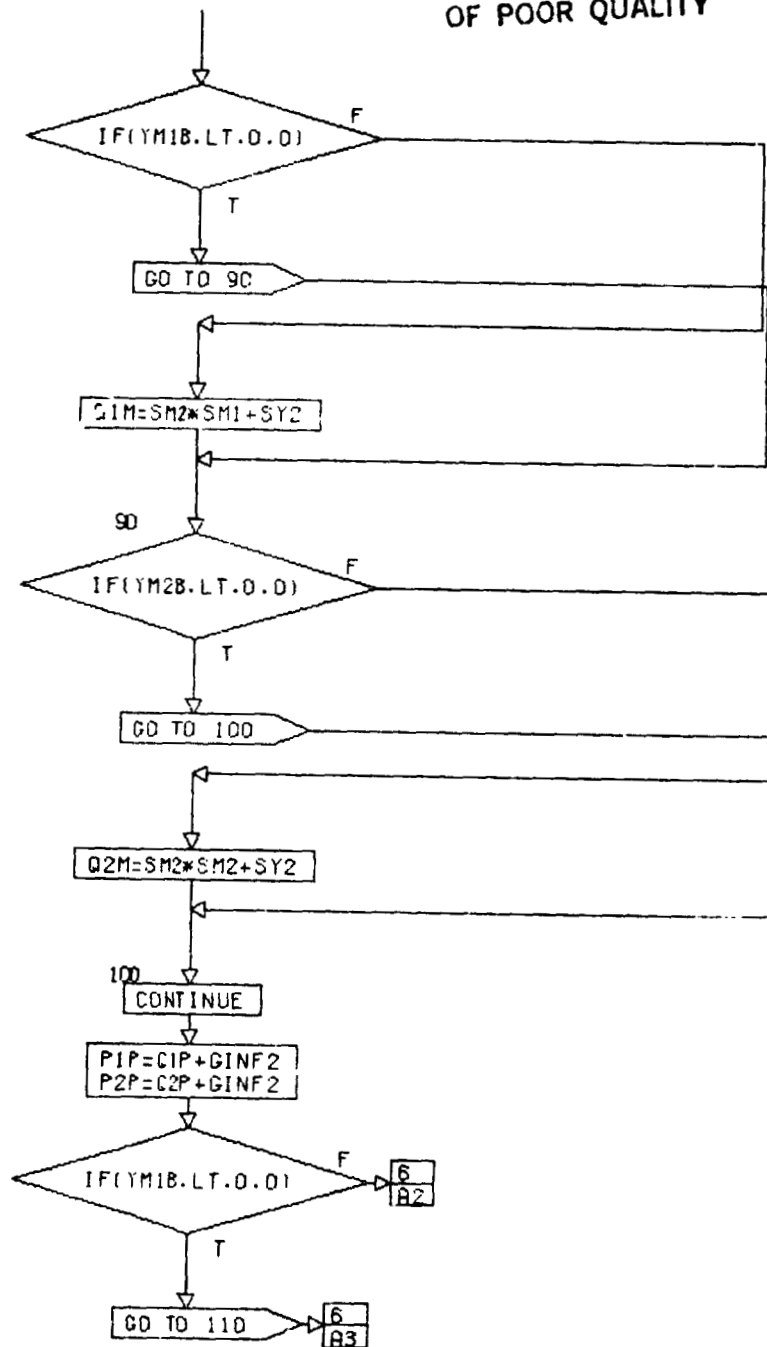
CONF. ON PG 4

PG 3 OF 11

ORIGINAL PAGE 19
OF POOR QUALITY



ORIGINAL PAGE IS
OF POOR QUALITY



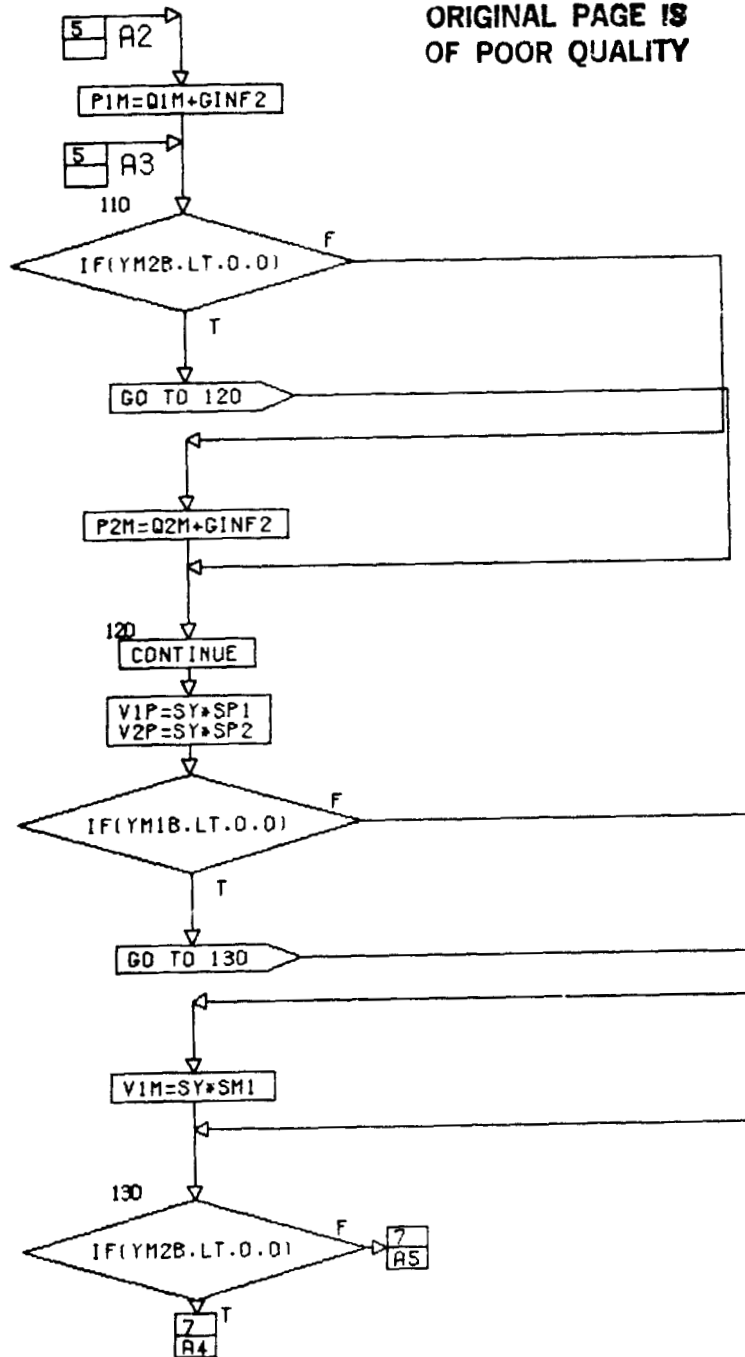
CONT. ON PG

6

PG 5 OF 11

(+)

ORIGINAL PAGE IS
OF POOR QUALITY

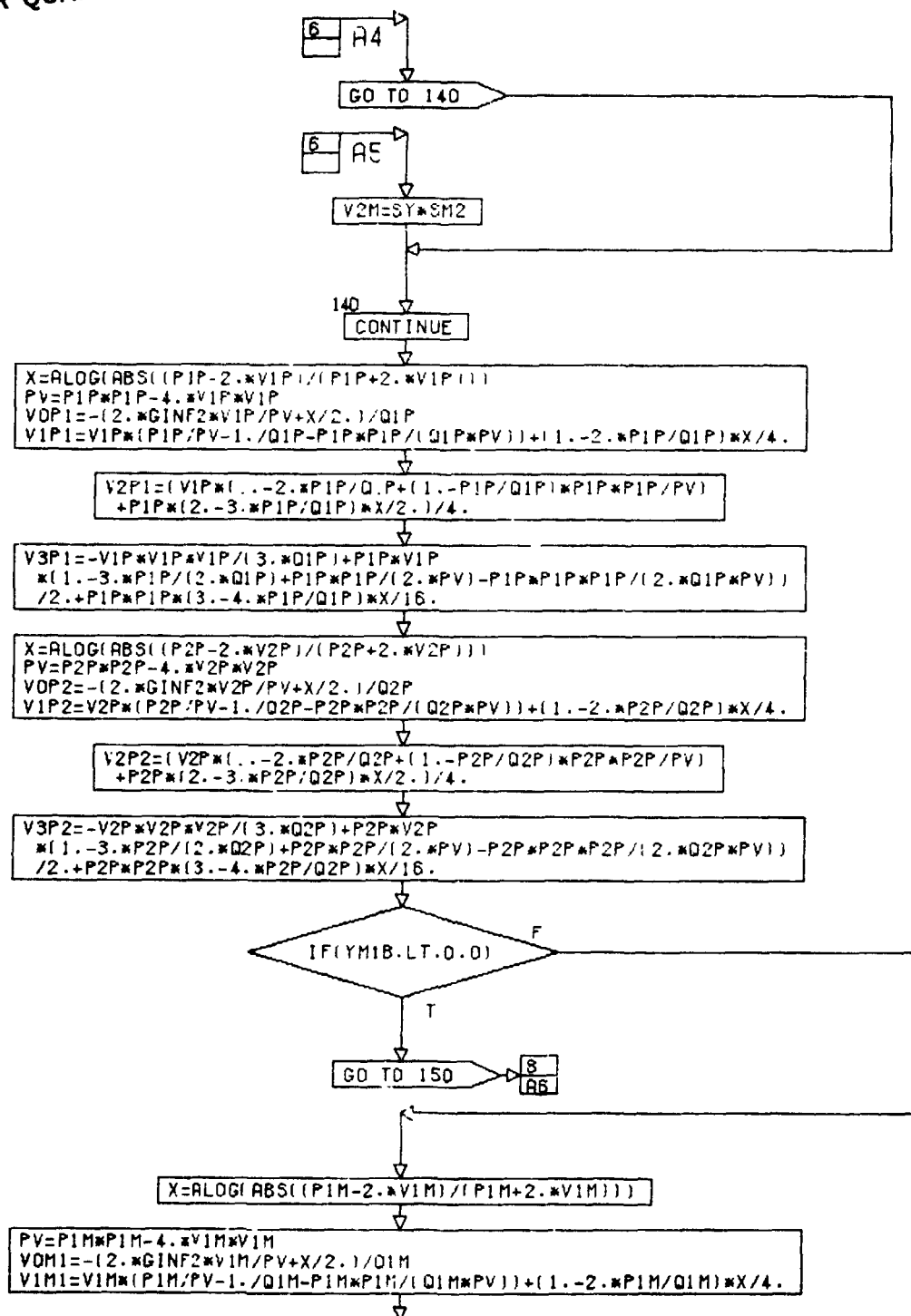


CONT. ON PG

7

PG 6 OF 11

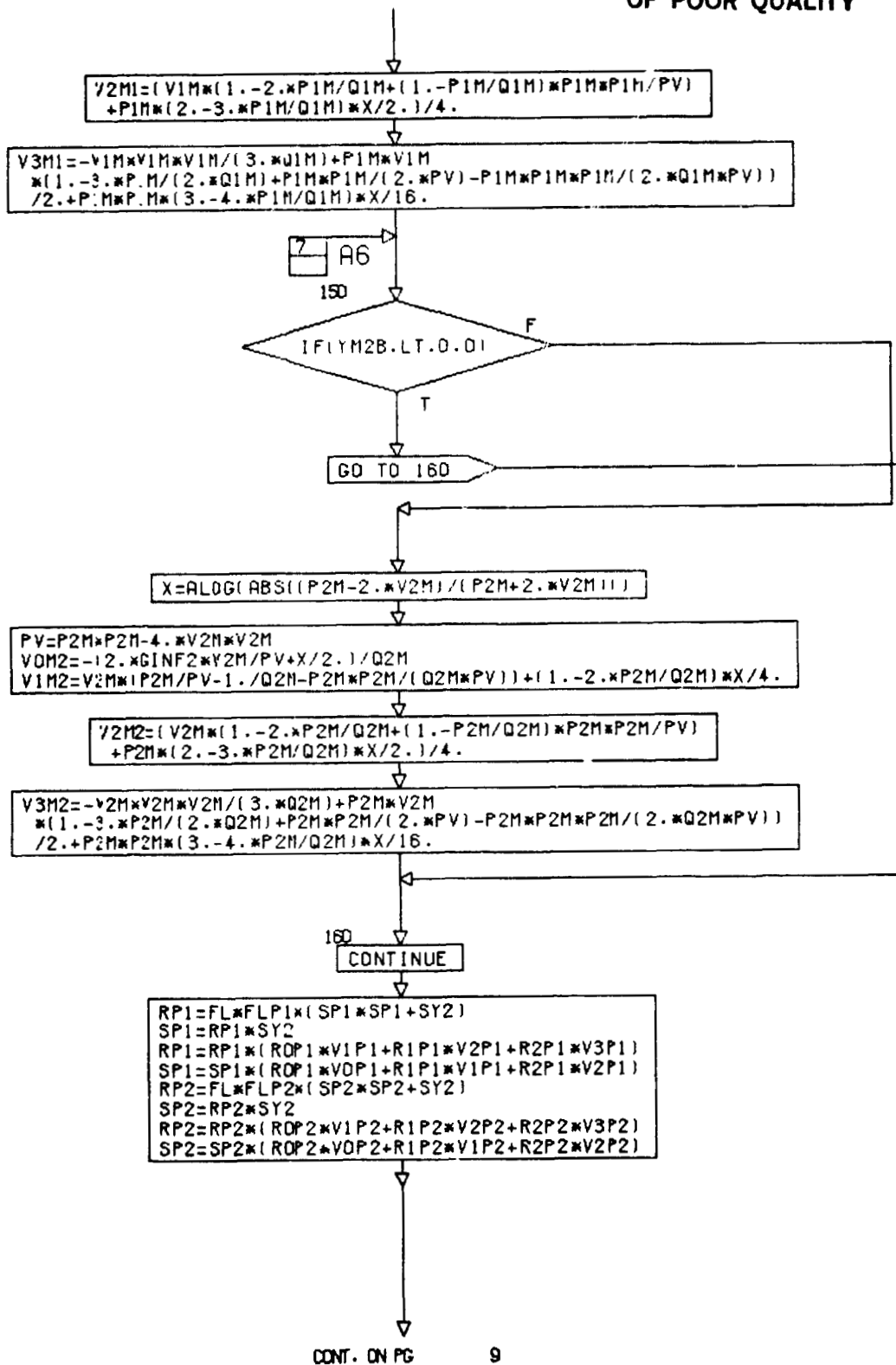
ORIGINAL PAGE IS
OF POOR QUALITY



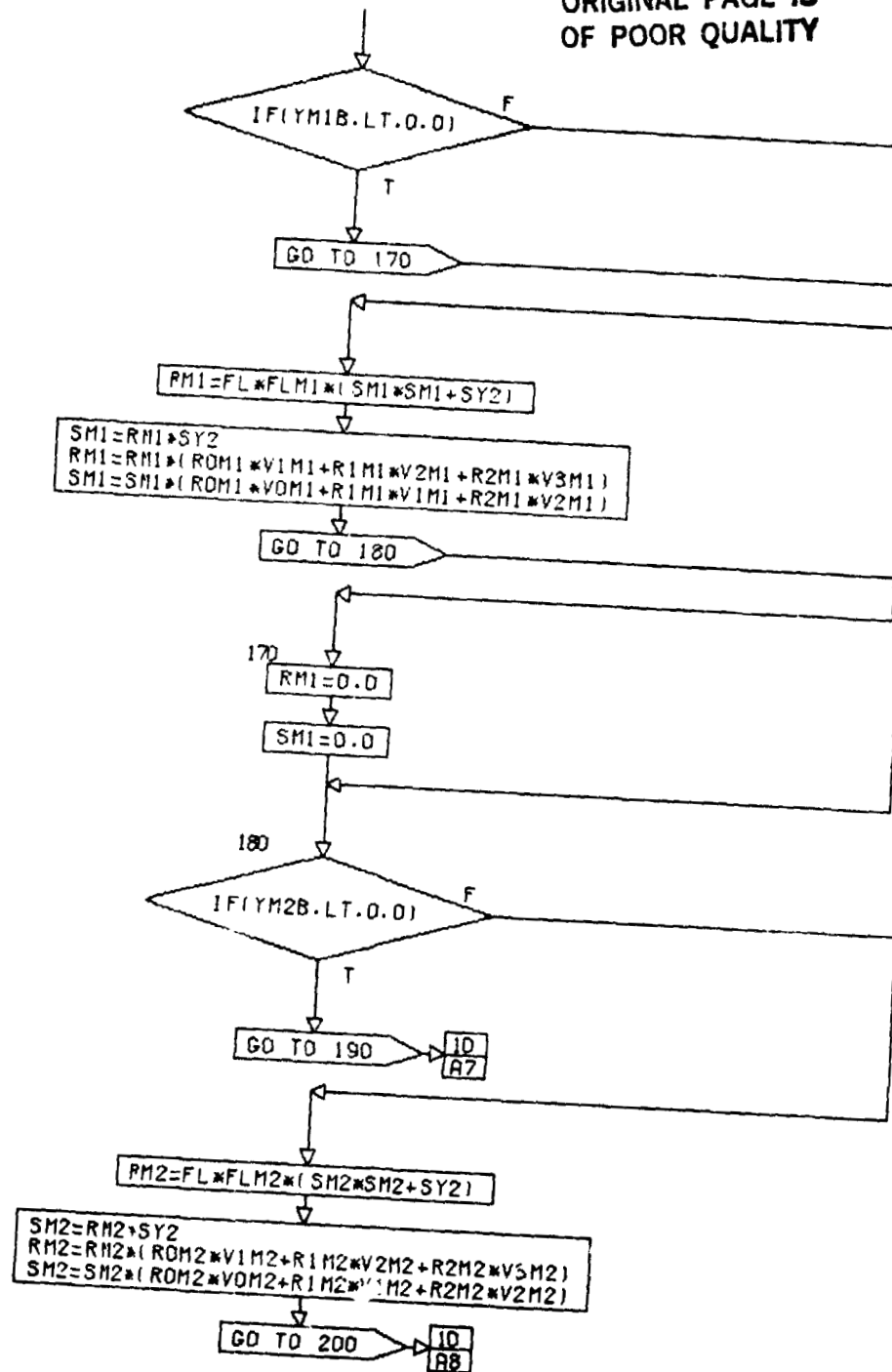
CONT. ON PG 8

PG 7 OF 11

ORIGINAL PAGE 19
OF POOR QUALITY



ORIGINAL PAGE IS
OF POOR QUALITY



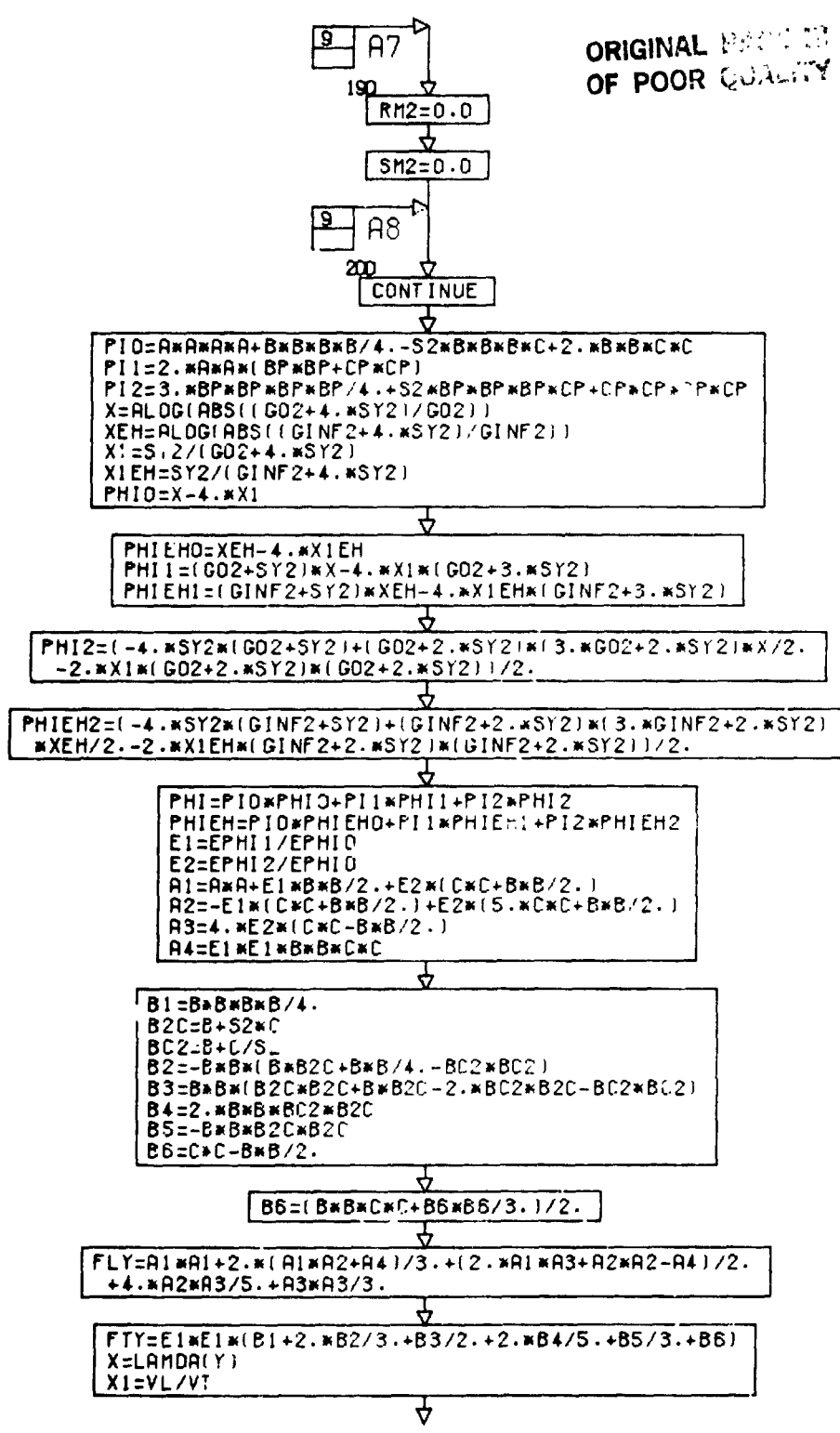
CONT. ON PG

10

PG 9 OF 11

(+)

ORIGINAL PAGE IS
OF POOR QUALITY



CONT. ON PG

11

PG 100F 11

ORIGINAL PAGE IS
OF POOR QUALITY

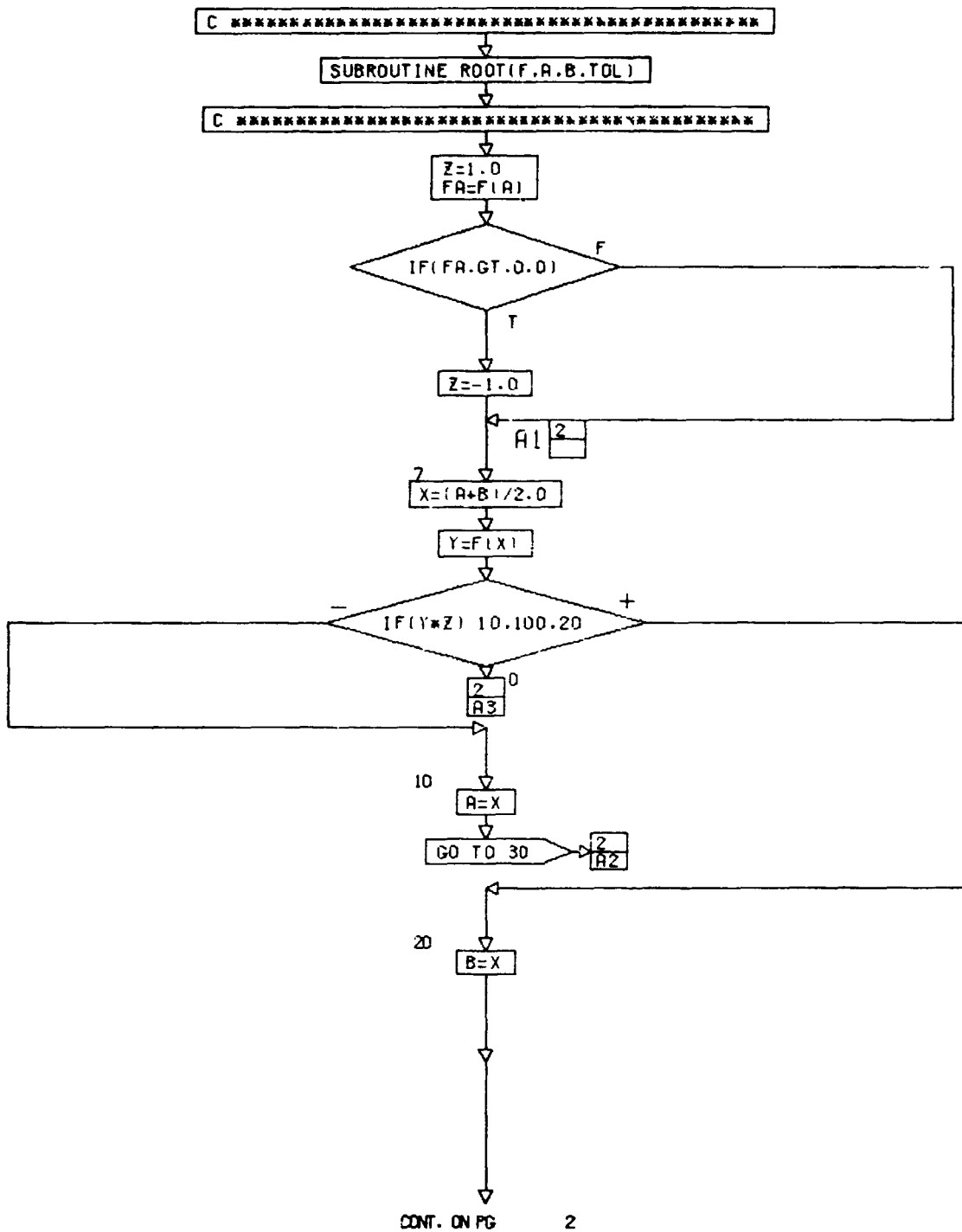
PHIDIS=2.*A**4.+B**4.+2./3.*C**4.-4.*SQRT(2.)/3.*B**3.*C
+4.*(B*C)**2.-4./3.*A**2.*(B**2.+C**2.)

LB=SA2***X*SY2*.FLY+X1*X1*FTY)+FL*FL*(SA3*PHI+SA*PHIEM)
+SA5*X**X*SI2*PHIDIS

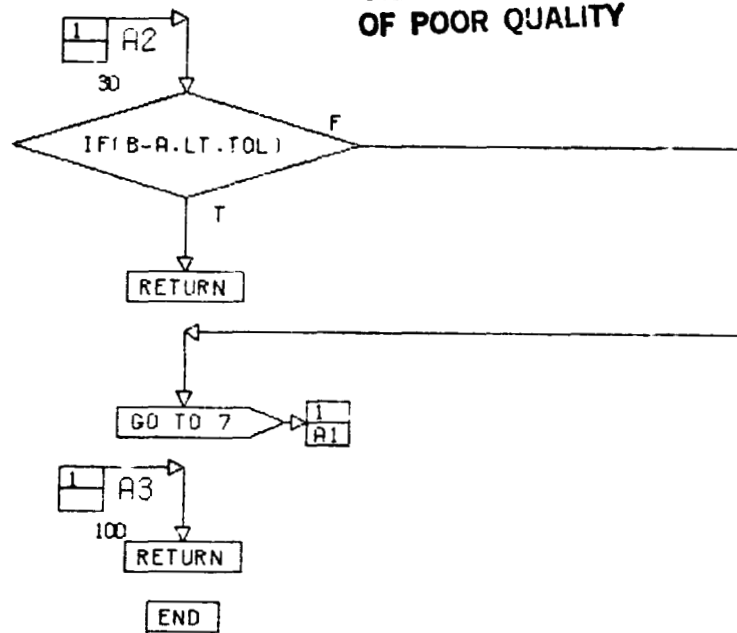
RETURN

END

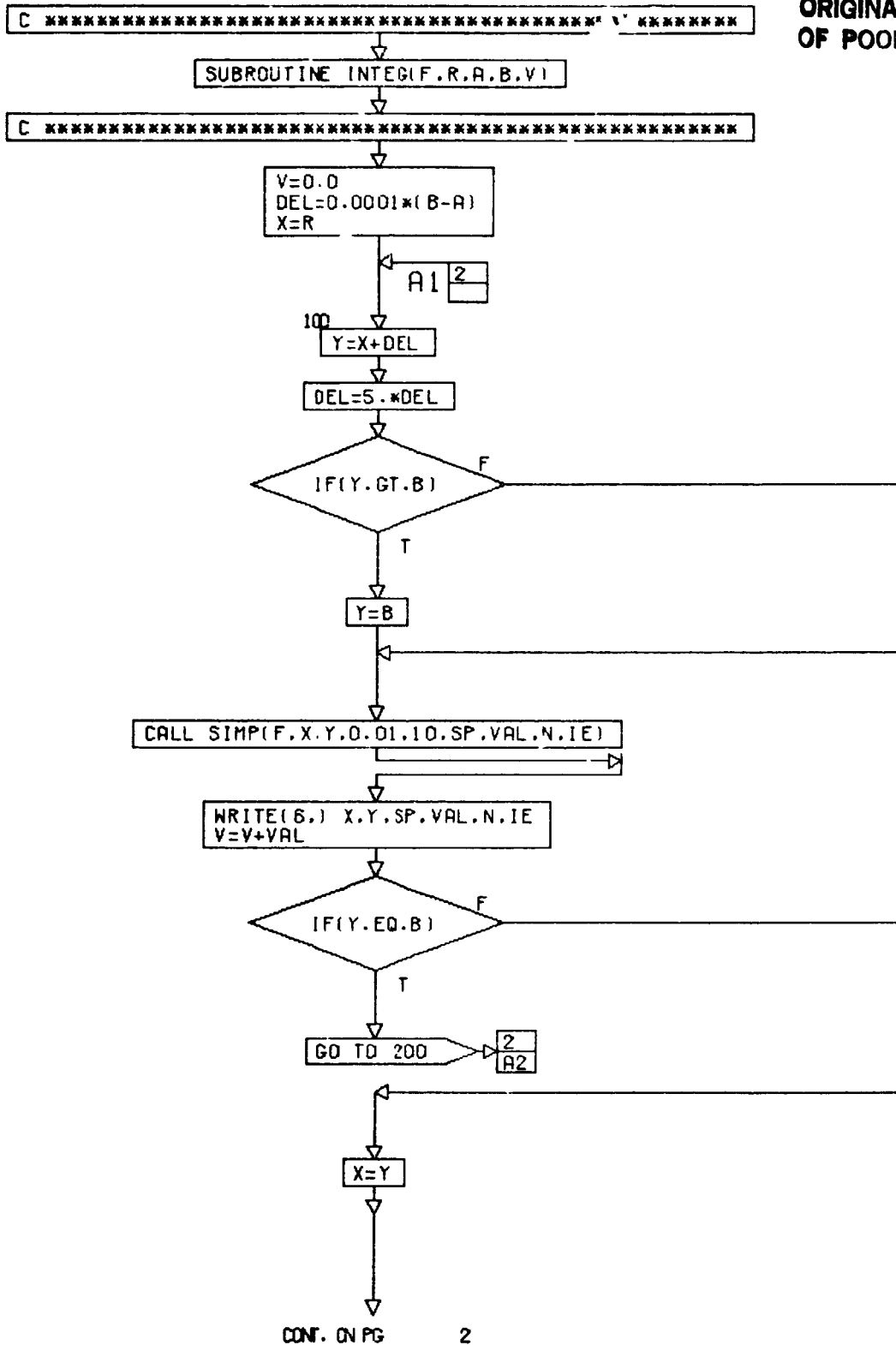
PG. 11 FINE



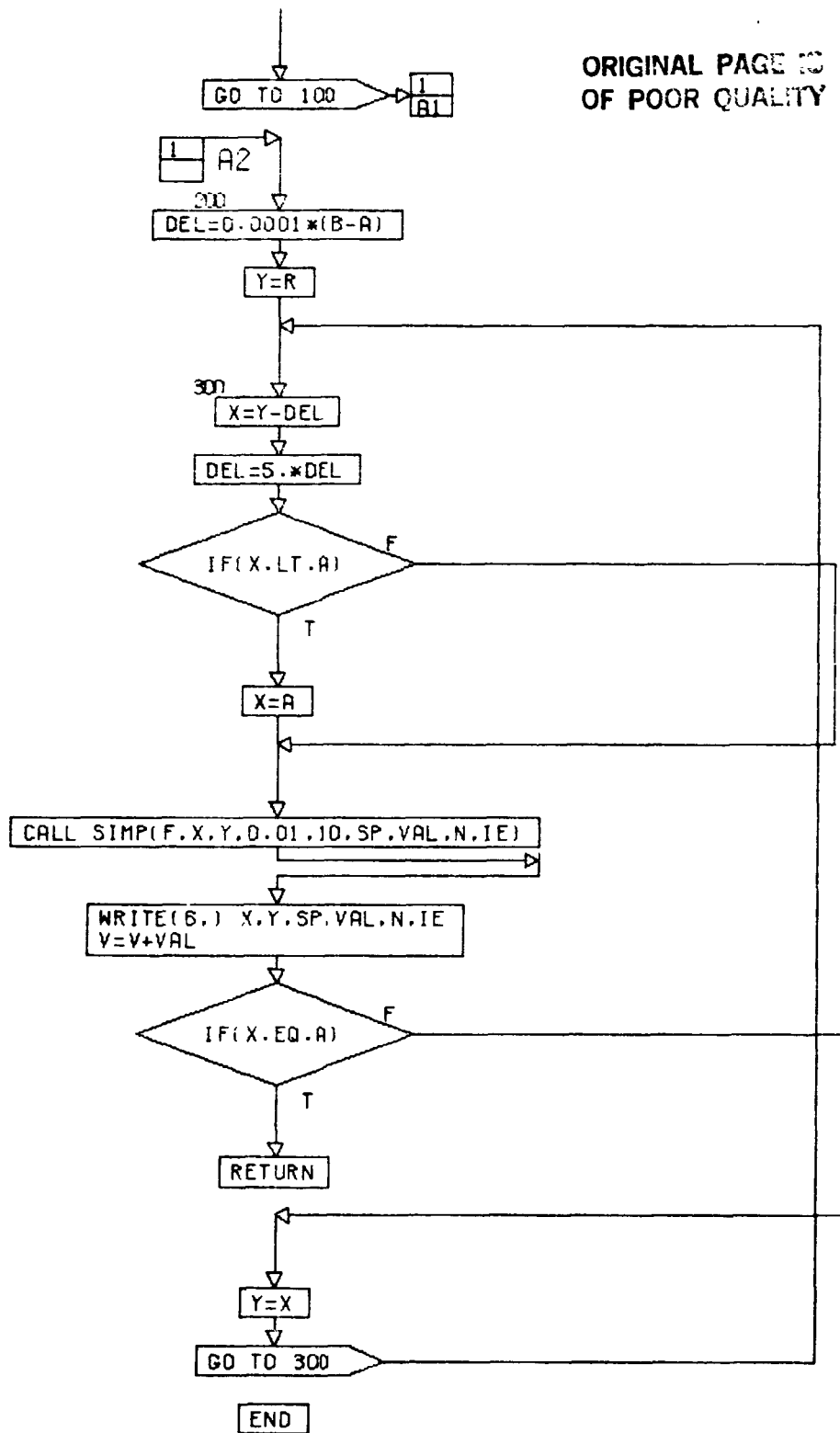
ORIGINAL PAGE IS
OF POOR QUALITY



PG 2 FINI



ORIGINAL PAGE IS
OF POOR QUALITY



PG 2 FINAL

C *****

FUNCTION FMN(Y)

C *****

REAL LB,NP1,NP2
COMMON /VAR/ Z,CON
COMMON /NM/ N,M
COMMON /CONST2/ BETA,DELTA,BI

COMMON /CONST3/ THETA1,THETA2,GINF2,G02,EPHI0,EPHI1,EPHI2,
VL,VT,A2,A3,A4,A5

COMMON /CONST4/ NP1,NP2,X1,X2,A1
X=Y-BI

CALL RSL(Y,RP1,RP2,RM1,RM2,SP1,SP2,SM1,SM2,LB)

XM=0.0
XN=0.0

IF(X.EQ.0.0)

GO TO 10

XM=X**M

XN=X**N

10
XMN=XM*XN

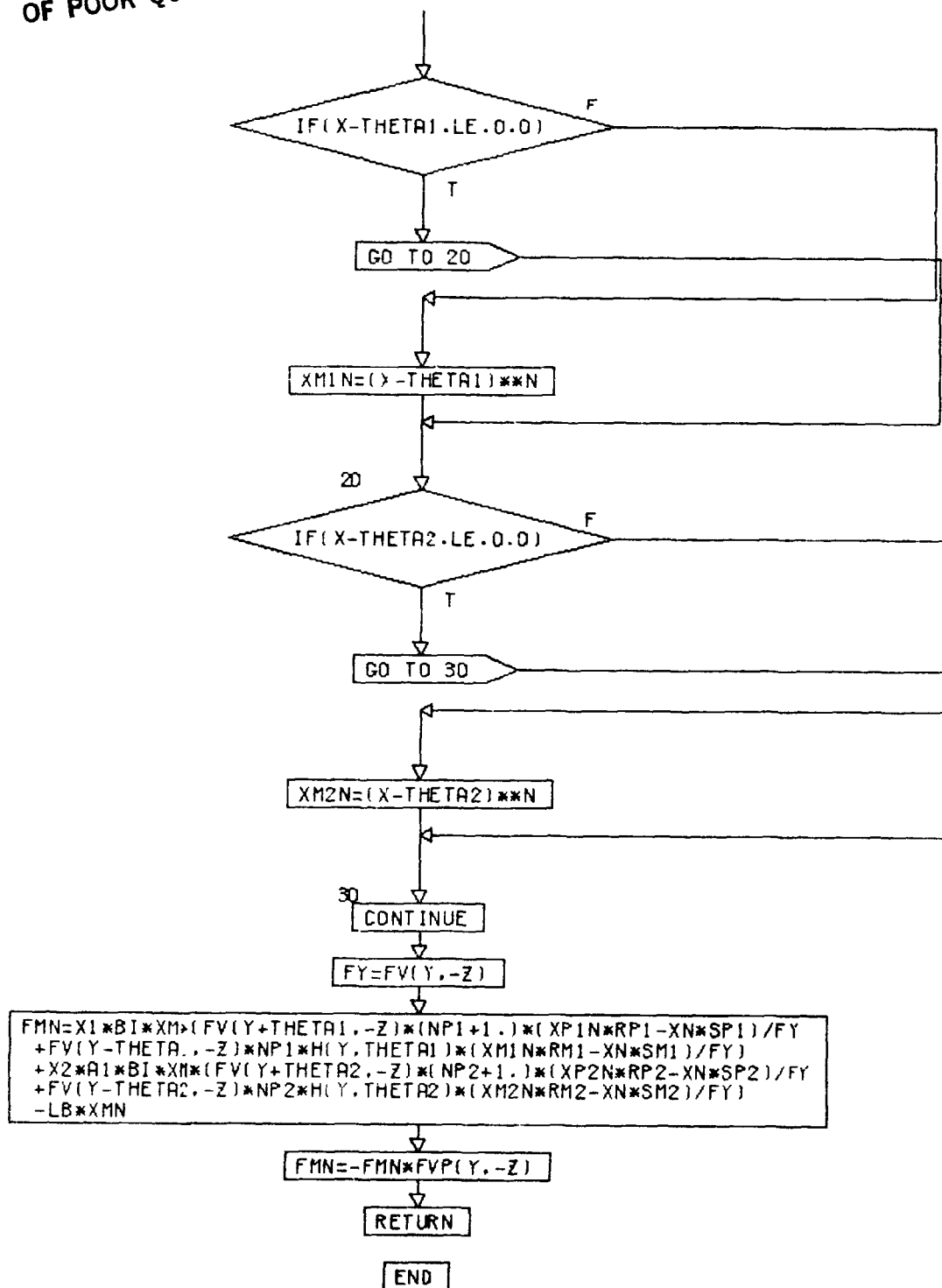
XP1N=(X+THETA1)**N
XP2N=(X+THETA2)**N
XM1N=0.0
XM2N=0.0

CONT. ON PG 2

ORIGINAL PAGE IS
OF POOR QUALITY

PG 1 OF 2

ORIGINAL PAGE 19
OF POOR QUALITY



PG. 2 FINAL

C *****

ORIGINAL PAGE 19
OF POOR QUALITY

FUNCTION FM(Y)

C *****

```
REAL L1
COMMON /VAR/ Z,CON
COMMON /NM/ N,M
COMMON /CONST2/ BETA,DELTA,BI
X=Y-BI
XM=0.0
```

IF(X.EQ.0.0)

F

T

GO TO 10

XM=X**M

10

CONTINUE

FM=-FVP(Y,-Z)*L1(Y)*XM

RETURN

END

PG 1 FINL

ORIGINAL PAGE IS
OF POOR QUALITY

SUBROUTINE HCSPOL(X,THT1,THT2,THL1,THL2,ESTR1,ESTR2,EPSO,
EPSI,EC1,EC2)

ESTR=.296
ESTR2=.235
XM1=.29505E-22
XM2=9.92339E-23
A=(6.460+0.21*X)*1.0E-8
EPSI=15.1077-13.8823*X+9.88928*X*X-3.67133*X*X*X
EPSO=20.286-15.1531*X+6.59091*X*X-0.951326*X*X*X
WT2=.52-0.9*X

WT1=118.0+12.0*X
ES=4.80325E-10
HB=1.0545919E-27
BK=1.380622E-16
PI=3.141593
C=2.9979250E10
THT1=2.*PI*C*HB/BK*WT1
THT2=2.*PI*C*HB/BK*WT2

OMT1=BK*THT1/HB
OMT2=BK*THT2/HB
F1=4.*PI/(A**3./4.)*ESTR1**2./XM1*(1.->)*ES**2.
F2=4.*PI/(A**3./4.)*ESTR2**2./XM2*X*ES**2.
S1=F1/OMT1**2.
S2=F2/OMT2**2.

THLM2=1./2./EPSI*(EPSI*(THT1**2.+THT2**2.)+S1*THT1**2.
+S2*THT2**2.-SQRT((EPSI*(THT2**2.-THT1**2.)+S2*THT2**2.
-S1*THT1**2.))**2.+4.*THT1**2.*THT2**2.*S1*S2))

THLP2=1./2./EPSI*(EPSI*(THT1**2.+THT2**2.)+S1*THT1**2.
+S2*THT2**2.+SQRT((EPSI*(THT2**2.-THT1**2.)+S1*THT2**2.
-S1*THT1**2.))**2.+4.*THT1**2.*THT2**2.*S1*S2))

THLO=SQRT((EPSI+S1)/EPSI)*TH1
THL12=THLM2
THL22=THLP2

IF(THT2.GT.THLO)

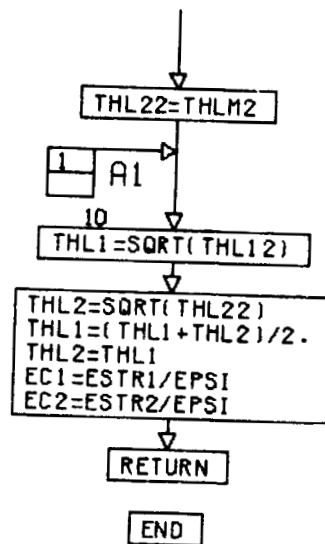
GO TO 10

THL12=THLP2

CONT. ON PG 2

PG 1 OF 2

ORIGINAL PAGE IS
OF POOR QUALITY



PG 2 FINI

ORIGINAL PAGE IS
OF POOR QUALITY

B.4 Computer Program

```

00100$FIXED
00110$SOURCE:CUHE,M0326B
00120$SOURCE:FFCTS,M0326B
00130$SOURCE:SIMP,M0326A
00140C MERGE FFCTS,INTRPL,CUBE & SIMP
00150 REAL KFTE2,KFTLH2,KFTHH2
00160 REAL MN(3,3),ML1(3)
00170 LOGICAL GEND
00180 REAL NE,NLH,NHH,NP1,NP2
00190 REAL K,ND,KT,M0,M,M2,M00,NA
00191 REAL NU1
00200 REAL M1B,M2B
00210 DIMENSION ISBSCP(7),VALUE(7),PARM(7)
00220 COMMON /NNN/ NE,NLH,NHH,ND1
00230 COMMON /CONST1/ P1,P,HB,KT,ND,UV,M0,D,EG,YBC,YBV,NA,Z1,ZA
00240 COMMON /VAR/ Z,CON
00250 COMMON /NM/ N,M
00260 COMMON /CONST2/ BETA,DELTA,B1
00270 COMMON /CONST3/ THETA1,THE!A2,GINF2,G02,EPH10,EPH11,EPH12,
00280 1 VL,VT,A2,A3,A4,A5
00290 COMMON /CONST4/ NP1,NP2,X1,X2,A1
00300 EXTERNAL FUNC3,FUNC4
00310 EXTERNAL FMN,FM
00320 WRITE(6,1)
00330 1 FORMAT('PARAMETER LIST: 1 ** TMIN: 2 ** TMAX: 3 ** ',
00340 4 ** DELT: 4 ** DONOR DENSITY: 5 ** ACCEPTOR DENSITY:
00350 6 ** PROPORTION OF COTE IN ALLOY: 7 ** DISORDER
00360 &ENERGY IN EV: ')
00500 ES=4.0325E-10
00510 HB=1.05459E-27
00520 K=1.380622E-16
00530 M0=9.109558E-28
00540 P1=3.141593
00550 CEVE=1.6021917E-12
00560 CALL FFCTS
00570 NRUN=1
00580 20 IF(N-UN.EQ.1) GO TO 21
00590 WRITE(6,3)
00600 3 FORMAT('CONTINUE? 1=YES, 2=NO')
00610 READ(2,*) NCONT
00620 IF(NCONT.EQ.2) GO TO 550
00630 21 NRUN=NRUN+1
00640 WRITE(6,4)
00650 4 FORMAT('ENTER NUMBER OF PARMS TO BE CHANGED AND ',
00660 6 '(PARM NO.,NEW VALUE) : FOR EACH CHANGE: ')
00670 READ(2,*) NCHNGE,(ISBSCP(I),VALUE(I),I=1,NCHNGE)
00680 DO 25 I=1,NCHNGE
00690 J=ISBSCP(I)
00700 25 PARM(J)=VALUE(I)
00705 X2=PARM(6)
00706 X1=-A2
00710 WRITE(6,6)
00720 6 FORMAT('PARAMETERS FOR THIS RUN ARE: ')
00730 DO 27 I=1,7
00740 27 WRITE(6,*) I,PARM(I)
00741 CALL HCSPOL(X2,THTRAN1,THTRAN2,THL1,THL2,ETRAN1,ETRAN2,
00742 1E0,EINF,E1RS,E2RS)
00743 WRITE(6,10) E0,EINF,E1RS,E2RS,THL1,THL2,THTRAN1,THTRAN2,
00744 1ETRAN1,ETRAN2
00745 10 FORMAT('X,EPSC=,F8.4, EPSINF=,F8.4/IX,HGTE CALLEN',
00746 1' CHARGE=,F8.4, COTE CALLEN CHARGE=,F8.4/IX,HGTE LO',
00747 2' PHONON TEMP=,F8.4, COTE LO PHONON TEMP=,F8.4/IX,
00748 3'HGTE TO PHONON TEMP=,F8.4, COTE TO PHONON TEMP=,F8.4/
00749 4IX,HGTE TRANSVERSE CHARGE=,F8.4, COTE TRANSVERSE ',
00750 5'CHARGE =,F8.4//)
00751 WRITE(6,5)
00760 5 FORMAT(' T Z EG(T) (EF-EG)/KT:
00770 6' NE NLH NHH:
00780 6' MOBILITY: ')
00790 TMIN=PARM(1)
00800 TMAX=PARM(2)
00810 DTEMP=PARM(3)
00820 ND=PARM(4)
00830 Z1=1.
00840 NA=PARM(5)
00850 ZA=1.
00880 DEV=1.08-0.18*X2
00885 D=DEV*CEVE
00890 UV=0.53

```

ORIGINAL PAGE IS
OF POOR QUALITY

```

00960      E0EV=9.5
00970      E1EV=4.
00980      E2EV=3.
00990      VI=(2.52+0.54*X2)*1.0E5
01000      VT=(1.60+0.27*X2)*1.0E5
01030      M0=127.60
01040      M1=200.59
01050      M2=112.4
01060      PHI=4.*(X2*112.4+X1*200.59+127.60)*1.66056551/(6.460+0.021*X2)
01070      1.*3
01100      AL=(6.460+0.021*X2)*1.0E-8
01110      EDISEV=PARM(7)
01120      EDIS=CEVE*EDISEV
01140      EPHI0=CEVE*E0EV
01150      EPHI1=CEVE*E1EV
01160      EPHI2=CEVE*E2EV
01170      E1S=E1RS*ES
01180      E2S=E2RS*ES
01190      M1B=1.66043E-24*M00*M1/(M00+M1)
01200      M2B=1.66043E-24*M00*M2/(M00+M2)
01210      VA=AL*AL*AL/4.
01220      WL1=K*THL1/HB
01230      WL2=K*THL2/HB
01240      XNAT=2.*PHI/(M00+X1*M1+X2*M2)/1.66043E-24
01250      T=TMIN
60 CONTINUE
01260      KT=K*T
01270      EG=CEVE*(-0.25+1.59*X2+0.327*X2*X2+5.233E-4*(1.0-2.08*X2)*T)
01285      P=8.6E-8*CEVE
01290      DELTA=EG/D
01300      BETA=KT/EG
01310      BI=1./BETA
01320      UP=3.*HB*HB*EG/(4.*M0*P*P)
01330      CALL SECULAR(2.*PI/AL,YBC,YBV,E3)
01340      YBC=YBC/KT
01350      YBV=-YBV/KT
01360      CON=2.*UP*M0*KT/(HB*HB)
01370      CON=CON*SQRT(CON)/(2.*PI*PI*SQRT(BETA))
01380      Z=1000./1
01390      DELZ=0.3*Z
01400      GEND=.FALSE.
70 XDL=FUNC(Z)
01410      IF(XDL.LT.0.0) GO TO 75
01420      GEND=.TRUE.
01430      XDU=XDL
01440      Z=Z-DELZ
01450      GO TO 70
01460      75 IF(GEND) GO TO 90
01470      GO TO 85
01480      80 XDL=XDU
01490      85 Z=Z+DELZ
01500      XDU=FUNC(Z)
01510      IF(XDU.LT.0.0) GO TO 80
01520      ZU=Z
01530      ZL=Z-DELZ
01540      GO TO 95
01550      90 ZL=Z
01560      ZU=Z+DELZ
01570      95 IF(DELZ.LE.2.E-4*ABS(Z)) GO TO 110
01580      DELZ=DELZ/2.
01590      Z=ZL+DELZ
01600      XDM=FUNC(Z)
01610      IF(XDM.LT.0.0) GO TO 100
01620      ZU=Z
01630      GO TO 95
01640      100 XDL=XDM
01650      ZL=Z
01660      GO TO 95
01670      110 Z=ZL+DELZ*(-XDL/(XDU-XDL))
01680      XZ1=FUNC(Z)
01690      CON=2.*UP*M0/(HB*HB)
01700      CON=CON*SQRT(CON)*2.*ES*ES*SQRT(KT/BETA)/PI
01710      XZ1=10.*BI
01720      IF(Z.GT.B1) XZ1=10.*Z
01730      XZ1=AMIN1(YBC,XZ1)
01740      XZ2=10.
01750      IF(Z.LT.0.0) XZ2=10.-Z
01760      XZ2=AMIN1(YBV,XZ2)
01770      CALL SIMP(FUNC3,1./BETA,XZ1,0.01,10,S11,KFTE2,N,IER)
01780      KFTE2=CON*KFTE2
01790      CALL SIMP(FUNC4,0.0,XZ2,0.01,10,S11,KFTLH2,N,IER)
01800      KFTLH2=CON*KFTLH2
01810      KFTHH2=(2.*UV*M0/(HB*HB))*(.3/2.)
01820      KFTHH2=KFTHH2*ES*ES*SQRT(KT)*F(-1,-Z)/PI
01830

```

```

01840 THETA1=THL1/T
01850 THETA2=THL2/T
01860 GINF2=HB*HB*(KFTE2*KFTLH2)/(2.*UP*M0*EG*EINF)
01870 G02=HB*HB*(KFTE2*KFTLH2*KFIHH2)/(2.*UP*M0*EG*E0)
01880 A1=E2S/E1S
01890 A1=A1*A1*M1B*WL1/(M2B*WL2)
01900 A2=EG*EPHI0/(PI*HB*E1S*E5*VL)
01910 A2=A2*A2*M1B*VA*WL1*UP*M0/(2.*HB*PHI)
01920 A3=ES/(E1S*E0)
01930 A3=A3*A3*HB*M1B*VA*WL1*(ND1*ZI*ZI*NA*ZA*ZA)/(4.*UP*M0*KT)
01940 A4=ES/(E1S*EINF)
01950 A4=A4*A4*HB*M1B*VA*WL1*NHH/(4.*UP*M0*KT)
01960 AS=EG*EG/HB*EDIS*EDIS/HB*UP*M0/HB*M1B/(E1S*ES)*VA/(E1S*ES)
01970 6*WL1/KT/XNAT*X1*X2/2./PI/PI
01980 NP1=1./(EXP(THETA1)-1.)
01990 NP2=1./(EXP(THETA2)-1.)
02000 BI=1./BETA
02010 THLIM=AMAX1(THETA1,THETA2)
02020 YLIM=10.*BI*THLIM
02030 IF(Z.GT.BI) YLIM=10.*Z*THLIM
02040 YLIM=AMIN1(YBC,YLIM)
02050 DO 200 I=1,3
02060 M=I-1
02070 DO 200 J=1,3
02080 N=J-1
02090 CALL SIMP(FMN,BI,YLIM,0.001,10,SII,MN(I,J),L,IER)
02100 200 CONTINUE
02110 DO 250 I=1,3
02120 M=I-1
02130 CALL SIMP(FM,BI,YLIM,0.001,10,SII,ML1(I),L,IER)
02140 250 CONTINUE
02150 Q1=MN(1,1)
02160 Q2=MN(1,1)*MN(2,2)-MN(1,2)*MN(2,1)
02170 Q3=MN(1,1)*(MN(2,2)*MN(3,3)-MN(2,3)*MN(3,2))
02180 1 +MN(1,2)*(MN(2,3)*MN(3,1)-MN(2,1)*MN(3,3))
02190 2 +MN(1,3)*(MN(2,1)*MN(3,2)-MN(2,2)*MN(3,1))
02200 QL1=MN(1,1)*ML1(2)-ML1(1)*MN(2,1)
02210 QL2=MN(1,1)*(MN(2,2)*ML1(3)-ML1(2)*MN(3,2))
02220 1 +MN(1,2)*(ML1(2)*MN(3,1)-MN(2,1)*ML1(3))
02230 2 +ML1(1)*(MN(2,1)*MN(3,2)-MN(2,2)*MN(3,1))
02240 G1=ML1(1)*ML1(1)/MN(1,1)*QL1*QL1/(Q2*Q1)*QL2*QL2/(Q3*Q2)
02250 X=KT/(PI*HB*E1S)
02260 SIGMA=M1B*VA*WL1*X*X*G1/(3.*PI)
02270 UH=6.935E6*SIGMA/NE
02280 EGOPT=BI*KT/1.6021917E-12
02290 EFEGKT=Z-BI
02300 7 WRITE(6,7) T,Z,EGOPT,EFEGKT
02310 7 FORMAT(1X,F12.4,2X,1PE12.4,2X,1PE12.4,2X,1PE12.4)
02320 WRITE(6,8) NE,NLH,NHH
02330 8 FORMAT(13X,1PE12.4,2X,1PE12.4,2X,1PE12.4)
02340 WRITE(6,9) UH
02350 9 FORMAT(13X,1PE12.4/)
02360 T=T+DTEMP
02370 IF(T.LE.TMAX) J TO 60
02380 GO TO 20
02390 550 CONTINUE
02400 STOP
02410 END
02420C *****
02430 SUBROUTINE SECULAR(KS,E1,E2,E3)
02440C *****
02450 REAL KT,ND,M0,NA
02460 REAL KS
02470 COMMON /CONST1/ PI,P,HB,KT,ND,UV,M0,D,EG,YBC,YBV,NA,ZI,ZA
02480 C0=P*P*KS*KS
02490 C2=D-EG
02500 C1=(EG*D+C0)
02510 C0=-2.*D*C0/3.
02520 CALL CUBE(C2,C1,C0,E1,E2,E3)
02530 RETURN
02540 END
02550C *****
02560 FUNCTION FUNC(X)
02570C *****
02580 REAL NE,NLH,NHH
02590 REAL KT,ND,M0,NA
02591 REAL NDD,ND1
02600 COMMON /CONST1/ PI,P,HB,KT,ND,UV,M0,D,EG,YBC,YBV,NA,ZI,ZA
02610 COMMON /NNN/ NE,NLH,NHH,ND1
02620 COMMON /VAR/ Z,CON
02630 COMMON /CONST2/ BETA,DELTA,BI
02640 EXTERNAL FUNC1,FUNC2
02650 NE=0.0
02660 X2=10.*BI
02670 IF(Z.GT.BI) X2=10.*Z

```

```

02680      X2=AMIN1(YBC,X2)
02690      IF (X2.LE.B1) GO TO 100
02700      CALL SIMP(FUNC1,B1,X2,0.01,10,S11,NE,N,IER)
02710      NE=CON*NE
02720 100    NLH=0.0
02730      X2=10.
02740      IF (Z.LT.0.0) X2=(10.-Z)
02750      X2=AMIN1(YBV,X2)
02760      IF (X2.LE.0.0) GO TO 200
02770      CALL SIMP(FUNC2,0.0,X2,0.01,10,S11,NLH,N,IER)
02780      NLH=CON*NLH
02790 200    NHH=((2.*UV*M0*KT)/(HB*HB))**(3./2.)
02800      NHH=NHH*F(1,-Z)/(2.*PI*PI)
02801      ED=0.003*1.6021917E-12
02802      E2=EG-ED
02803      NDD=1.0E6/(0.5*EXP(-E2/KT*Z)+1.0)
02804      NU1=NO*NDD
02810      FUNC=NE-NLH-NHH-ND1*ZI+NA*ZA
02820      RETURN
02830      END
02840C *****
02850      FUNCTION FV(Y,Z)
02860C *****
02870      IF (Y+Z.LE.-500.) GO TO 10
02880      IF (Y+Z.LE.500.) GO TO 20
02890      FV=0.0
02900      GO TO 30
02910 10 FV=1.0
02920      GO TO 30
02930 20 FV=1./(EXP(Y+Z)+1.)
02940 30 CONTINUE
02950      RETURN
02960      END
02970C *****
02980      FUNCTION FUNC1(Y)
02990C *****
03000      REAL LAMDA
03010      COMMON /VAR/ Z,CON
03020      FUNC1=FV(Y,-Z)*LAMDA(Y)
03030      RETURN
03040      END
03050C *****
03060      FUNCTION FUNC2(Y)
03070C *****
03080      REAL LAMDAV
03090      COMMON /VAR/ Z,CON
03100      FUNC2=FV(Y,Z)*LAMDAV(Y)
03110      RETURN
03120      END
03130C *****
03140      FUNCTION FVP(Y,Z)
03150C *****
03160      IF (Y+Z.LE.-200.) GO TO 10
03170      IF (Y+Z.LE.200.) GO TO 20
03180      FVP=0.0
03190      GO TO 30
03200 10 FVP=0.0
03210      GO TO 30
03220 20 FVP=EXP(Y+Z)
03230      FVP=FVP/(FVP+1.)/(FVP+1.)
03240 30 CONTINUE
03250      RETURN
03260      END
03270C *****
03280      FUNCTION FUNC3(Y)
03290C *****
03300      REAL LAMDA
03310      COMMON /VAR/ Z,CON
03320      FUNC3=LAMDA(Y)*FVP(Y,-Z)
03330      RETURN
03340      END
03350C *****
03360      FUNCTION FUNC4(Y)
03370C *****
03380      REAL LAMDAV
03390      COMMON /VAR/ Z,CON
03400      FUNC4=LAMDAV(Y)*FVP(Y,Z)
03410      RETURN
03420      END
03430C *****
03440      REAL FUNCTION LAMDA(Y)
03450C *****
03460      COMMON /CONST2/ BETA,DELTA,B1
03470      BY=BETA*Y

```

ORIGINAL PAGE 19
OF POOR QUALITY

```

03480 IF (Y.EQ.B1) BY=1.
03490 LAMDA=2.*DELTA*DELTA*BY*BY*BY*DELTA*(3.-DELTA)*BY*BY
03500 1.*4.*(1.-DELTA)*BY/3.-2./3.
03510 X=3.*DELTA*BY/2.+1.
03520 LAMDA=3.*LAMDA*SQRT (BY*(BY-1.)*(DELTA*BY+1.)/(X*X*X*X*X))/2.
03530 RETURN
03540 END
03550C *****
03560 REAL FUNCTION LAMDAV(Y)
03570C *****
03580 COMMON /CONST2/ BETA,DELTA,B1
03590 BY=BETA*Y
03600 LAMDAV=2.*DELTA*DELTA*BY*BY*BY*DELTA*(3.-DELTA)*BY*BY
03610 1.*4.*(1.-DELTA)*BY/3.-2./3.
03620 X=3.*DELTA*BY/2.+1.
03630 LAMDAV=3.*LAMDAV*SQRT (BY*(BY+1.)*(DELTA*BY-1.)/(X*X*X*X*X))/2.
03640 RETURN
03650 END
03660C *****
03670 FUNCTION S(Y)
03680C *****
03690 COMMON /CONST2/ BETA,DELTA,B1
03700 BY=BETA*Y
03710 IF (Y.EQ.B1) BY=1.
03720 S=SQRT (BY*(BY-1.)*(DELTA*BY+1.)/(3.*DELTA*BY/2.+1.))
03730 RETURN
03740 END
03750C *****
03760 REAL FUNCTION L1(Y)
03770C *****
03780 COMMON /CONST2/ BETA,DELTA,B1
03790 L1=S(Y)/SQRT(BETA)
03800 L1=L1*L1*L1
03810 RETURN
03820 END
03830C *****
03840 FUNCTION H(Y,THETA)
03850C *****
03860 H=0.0
03870 IF (Y.LT.THETA) RETURN
03880 H=1.0
03890 RETURN
03900 END
03910C *****
03920 SUBROUTINE NABC(Y,A,B,BP,C,CP,FL)
03930C *****
03940 REAL N
03950 COMMON /CONST2/ BETA,DELTA,B1
03960 BY=BETA*Y
03970 IF (Y.EQ.B1) BY=1.
03980 DBY=DELTA*BY
03990 DBY23=DBY*2./3.
04000 N=SQRT (BY*(DBY+1.)*DBY23+2.*(BY-1.)/9.+(BY-1.)*DBY23*DBY23)
04010 A=SQRT (BY*(DBY+1.)*DBY23)/N
04020 B=SQRT (2.*(BY-1.))/(3.*N)
04030 C=SQRT (BY-1.)*DBY23/N
04040 CP=SQRT ((3.*DBY/2.+1.)/(BY*(DBY+1.)))
04050 BP=SQRT (2.)*CP/(3.*N)
04060 CP=DBY23*CP/N
04070 FL=3.*(2.*DBY*DBY*BY*DELTA*(3.-DELTA)*BY*BY+4.*(1.-DELTA)
04080 1.*BY/3.-2./3.)/(2.*(3.*DBY/2.+1.)*(3.*DBY/2.+1.))
04090 RETURN
04100 END
04110C *****
04120 SUBROUTINE RSL(Y,RP1,RP2,RM1,RM2,SP1,SP2,SM1,SM2,LB)
04130C *****
04140 REAL LAMDA
04150 REAL LB
04160 COMMON /CONST2/ BETA,DELTA,B1
04170 COMMON /CONST3/ THETA1,THETA2,GINF2,G02,EPH10,EPH11,EPH12,
04180 1 VL,VT,SA2,SA3,SA4,SA5
04190 YM18=Y-THETA1-B1
04200 YM28=Y-THETA2-B1
04210 SY=S(Y)
04220 SP1=S(Y*THETA1)
04230 SP2=S(Y*THETA2)
04240 IF (YM18.LT.0.0) GO TO 10
04250 SM1=S(Y-THETA1)
04260 10 IF (YM28.LT.0.0) GO TO 20
04270 SM2=S(Y-THETA2)
04280 20 CONTINUE
04290 CALL NABC(Y,A,B,BP,C,CP,FL)
04300 CALL NABC(Y,THETA1,AP1,BP1,BPP1,CP1,CP1,FLP1)
04310 CALL NABC(Y,THETA2,AP2,BP2,BPP2,CP2,CP2,FLP2)

```



```

04320 IF (YM1B.LT.0.0) GO TO 30
04330 CALL NABC(Y-THETA1,AM1,BM1,BPM1,CM1,CPM1,FLM1)
04340 30 IF (YM2B.LT.0.0) GO TO 40
04350 CALL NABC(Y-THETA2,AM2,BM2,BPM2,CM2,CPM2,FLM2)
04360 40 CONTINUE
04370 S2=SQRT(2.)
04380 BC=B*CP1+C*BP1
04390 ROP1=A*A*AP1-B*BP1*BC/S2+BC*BC/2.+B*B*BP1*BP1/4.
04400 BC=B*CP2+C*BP2
04410 ROP2=A*A*AP2-B*BP2*BC/S2+BC*BC/2.+B*B*BP2*BP2/4.
04420 IF (YM1B.LT.0.0) GO TO 50
04430 BC=B*CM1+C*BM1
04440 ROM1=A*A*AM1-B*BM1*BC/S2+BC*BC/2.+B*B*BM1*BM1/4.
04450 50 IF (YM2B.LT.0.0) GO TO 60
04460 BC=B*CM2+C*BM2
04470 ROM2=A*A*AM2-B*BM2*BC/S2+BC*BC/2.+B*B*BM2*BM2/4.
04480 60 CONTINUE
04490 BB=BP*BPP1+CP*CPP1
04500 BC=BP*CPP1+CP*BPP1
04510 BX=BP*BPP1
04520 CX=CP*CPP1
04530 R1P1=2.*A*AP1*BB
04540 R2P1=3.*BX*BX/4.+BX*BC/S2+2.*BX*CX-BC*BC/2.+CX*CX
04550 BB=BP*BPP2+CP*CPP2
04560 BC=BP*CPP2+CP*BPP2
04570 BX=BP*BPP2
04580 CX=CP*CPP2
04590 R1P2=2.*A*AP2*BB
04600 R2P2=3.*BX*BX/4.+BX*BC/S2+2.*BX*CX-BC*BC/2.+CX*CX
04610 IF (YM1B.LT.0.0) GO TO 70
04620 BB=BP*BPM1+CP*CPM1
04630 BC=BP*CPM1+CP*BPM1
04640 BX=BP*BPM1
04650 CX=CP*CPM1
04660 R1M1=2.*A*AM1*BB
04670 R2M1=3.*BX*BX/4.+BX*BC/S2+2.*BX*CX-BC*BC/2.+CX*CX
04680 70 IF (YM2B.LT.0.0) GO TO 80
04690 BB=BP*BPM2+CP*CPM2
04700 BC=BP*CPM2+CP*BPM2
04710 BX=BP*BPM2
04720 CX=CP*CPM2
04730 R1M2=2.*A*AM2*BB
04740 R2M2=3.*BX*BX/4.+BX*BC/S2+2.*BX*CX-BC*BC/2.+CX*CX
04750 80 CONTINUE
04760 SY2=SY*SY
04770 Q1P=SP1*SP1*SY2
04780 Q2P=SP2*SP2*SY2
04790 IF (YM1B.LT.0.0) GO TO 90
04800 Q1M=SM1*SM1*SY2
04810 90 IF (YM2B.LT.0.0) GO TO 100
04820 Q2M=SM2*SM2*SY2
04830 100 CONTINUE
04840 P1P=Q1P*GINF2
04850 P2P=Q2P*GINF2
04860 IF (YM1B.LT.0.0) GO TO 110
04870 P1M=Q1M*GINF2
04880 110 IF (YM2B.LT.0.0) GO TO 120
04890 Q2M=Q2M*GINF2
04900 120 CONTINUE
04910 V1P=SY*SP1
04920 V2P=SY*SP2
04930 IF (YM1B.LT.0.0) GO TO 130
04940 V1M=SY*SM1
04950 130 IF (YM2B.LT.0.0) GO TO 140
04960 V2M=SY*SM2
04970 140 CONTINUE
04980 X=ALOG(ABS((P1P-2.*V1P)/(P1P+2.*V1P)))
04990 PV=P1P*P1P-4.*V1P*V1P
05000 VOP1=-(2.*GINF2*V1P/PV+X/2.)/Q1P
05010 V1P1=V1P*(P1P/PV-1./Q1P-P1P*P1P/(Q1P*PV))+(1.-2.*P1P/Q1P)*X/4.
05020 V2P1=(V1P*(1.-2.*P1P/Q1P*(1.-P1P/Q1P)*P1P*P1P/PV)
05030 1 *P1P*(2.-3.*P1P/Q1P)*X/2.)/4.
05040 V3P1=-V1P*V1P*V1P/(3.*Q1P)*P1P*V1P
05050 1 *(1.-3.*P1P/(2.*Q1P)*P1P*P1P/(2.*PV)-P1P*P1P*P1P/(2.*Q1P*PV))
05060 2 /2.*P1P*P1P*(3.-4.*P1P/Q1P)*X/16.
05070 X=ALOG(ABS((P2P-2.*V2P)/(P2P+2.*V2P)))
05080 PV=P2P*P2P-4.*V2P*V2P
05090 VOP2=-(2.*GINF2*V2P/PV+X/2.)/Q2P
05100 V1P2=V2P*(P2P/PV-1./Q2P-P2P*P2P/(Q2P*PV))+(1.-2.*P2P/Q2P)*X/4.
05110 V2P2=(V2P*(1.-2.*P2P/Q2P*(1.-P2P/Q2P)*P2P*P2P/PV)
05120 1 *P2P*(2.-3.*P2P/Q2P)*X/2.)/4.
05130 V3P2=-V2P*V2P*V2P/(3.*Q2P)*P2P*V2P
05140 1 *(1.-3.*P2P/(2.*Q2P)*P2P*P2P/(2.*PV)-P2P*P2P*P2P/(2.*Q2P*PV))
05150 2 /2.*P2P*P2P*(3.-4.*P2P/Q2P)*X/16.

```

```

05160 IF (YMH.LT.0.0) GO TO 150
05170 X=ALOG(ABS((P1M-2.*V1M)/(P1M+2.*V1M)))
05180 PV=P1M*P1M-4.*V1M*V1M
05190 V0M1=-2.*GINF2*V1M/PV*X/2./Q1M
05200 V1M=V1M*(P1M/PV-1./Q1M-P1M*(Q1M*PV))+(1.-2.*P1M/Q1M)*X/4.
05210 V2M=(V1M*(1.-2.*P1M/Q1M+(1.-P1M/Q1M)*P1M*P1M/PV)
05220 1 *P1M*(2.-3.*P1M/Q1M)*X/2.)/4.
05230 V3M1=-V1M*V1M*V1M/(3.*Q1M)+P1M*V1M
05240 1 *(1.-3.*P1M/(2.*Q1M)+P1M*P1M/(2.*PV)-P1M*P1M*P1M/(2.*Q1M*PV))
05250 2 /2.*P1M*P1M*(3.-4.*P1M/Q1M)*X/16.
05260 150 IF (YMH.LT.0.0) GO TO 160
05270 X=ALOG(ABS((P2M-2.*V2M)/(P2M+2.*V2M)))
05280 PV=P2M*P2M-4.*V2M*V2M
05290 V0M2=-2.*GINF2*V2M/PV*X/2./Q2M
05300 V1M2=V2M*(P2M/PV-1./Q2M-P2M*P2M/(Q2M*PV))+(1.-2.*P2M/Q2M)*X/4.
05310 V2M2=(V2M*(1.-2.*P2M/Q2M+(1.-P2M/Q2M)*P2M*P2M/PV)
05320 1 *P2M*(2.-3.*P2M/Q2M)*X/2.)/4.
05330 V3M2=-V2M*V2M*V2M/(3.*Q2M)+P2M*V2M
05340 1 *(1.-3.*P2M/(2.*Q2M)+P2M*P2M/(2.*PV)-P2M*P2M*P2M/(2.*Q2M*PV))
05350 2 /2.*P2M*P2M*(3.-4.*P2M/Q2M)*X/16.
05360 160 CONTINUE
05370 RP1=FL*FLP1*(SP1*SP1+SY2)
05380 SP1=RP1*SY2
05390 RP1=RP1*(R0P1*V1P1+R1P1*V2P1+R2P1*V3P1)
05400 SP1=SP1*(R0P1*V0P1+R1P1*V1P1+R2P1*V2P1)
05410 RP2=FL*FLP2*(SP2*SP2+SY2)
05420 SP2=RP2*SY2
05430 RP2=RP2*(R0P2*V1P2+R1P2*V2P2+R2P2*V3P2)
05440 SP2=SP2*(R0P2*V0P2+R1P2*V1P2+R2P2*V2P2)
05450 IF (YMH.LT.0.0) GO TO 170
05460 RM1=FL*FLM1*(SM1*SM1+SY2)
05470 SM1=RM1*SY2
05480 RM1=RM1*(R0M1*V1M1+R1M1*V2M1+R2M1*V3M1)
05490 SM1=SM1*(R0M1*V0M1+R1M1*V1M1+R2M1*V2M1)
05500 GO TO 180
05510 170 RM1=0.0
05520 SM1=0.0
05530 180 IF (YMH.LT.0.0) GO TO 190
05540 RM2=FL*FLM2*(SM2*SM2+SY2)
05550 SM2=RM2*SY2
05560 RM2=RM2*(R0M2*V1M2+R1M2*V2M2+R2M2*V3M2)
05570 SM2=SM2*(R0M2*V0M2+R1M2*V1M2+R2M2*V2M2)
05580 GO TO 200
05590 190 RM2=0.0
05600 SM2=0.0
05610 200 CONTINUE
05620 P10=A*A*A*A+B*B*B*B/4.-S2*B*B*B*C+2.*B*B*B*C
05630 P11=2.*A*A*(BP*RP*CP*CP)
05640 P12=3.*BP*BP*BP*BP/4.+S2*BP*BP*BP*CP+CP*CP*CP*CP
05650 X=ALOG(ABS((G02+4.*SY2)/G02))
05660 XEH=ALOG(ABS((GINF2+4.*SY2)/GINF2))
05670 X1=SY2/(G02+4.*SY2)
05680 X1EH=SY2/(GINF2+4.*SY2)
05690 PH10=X-4.*X1
05700 PH1EH=XEH-4.*X1EH
05710 PH11=(G02+SY2)*X-4.*X1*(G02+3.*SY2)
05720 PH1EH1=(GINF2+SY2)*XEH-4.*X1EH*(GINF2+3.*SY2)
05730 PH12=(1.-4.*SY2*(G02+SY2))/(G02+2.*SY2)*(3.*G02+2.*SY2)*X/2.
05740 1 -2.*X1*(G02+2.*SY2)*(G02+2.*SY2)/2.
05750 PH1EH2=(-4.*SY2*(GINF2+SY2)+(GINF2+2.*SY2)*(3.*GINF2+2.*SY2)
05760 1 *XEH/2.-2.*X1EH*(GINF2+2.*SY2)*(GINF2+2.*SY2))/2.
05770 PH1=PH10*PH10*P11*PH11*P12*PH12
05780 PH1EH=PH10*PH1EH0*P11*PH1EH1*P12*PH1EH2
05790 E1=EPH11/EPH10
05800 E2=EPH12/EPH10
05810 A1=A*A*E1*B*B/2.+E2*(C*C*B*B/2.)
05820 A2=-E1*(C*C*B*B/2.)+E2*(5.*C*C*B*B/2.)
05830 A3=4.*E2*(C*C*B*B/2.)
05840 A4=E1*E1*B*B*C*C
05850 B1=B*B*B*B/4.
05860 B2C=B*S2*C
05870 B2C2=B*C/S2
05880 B2=-B*B*(B*B2C*B*B/4.-B2C*B2C)
05890 B3=B*B*(B2C*B2C*B*B2C-2.*B2C*B2C-B2C*B2C)
05900 B4=2.*B*B*B2C*B2C
05910 B5=-B*B*B2C*B2C
05920 B6=C*C*B*B/2.
05930 B6=(B*B*C*C*B6*B6/3.)/2.
05940 FLY=A1*A1+2.*(A1*A2+A4)/3.+(2.*A1*A3+A2*A2-A4)/2.
05950 1 +4.*A2*A3/5.+A3*A3/3.
05960 FTY=E1*E1*(B1+2.*B2/3.+B3/2.+2.*B4/5.+B5/3.+B6)
05970 X=LAMDA(Y)
05980 X1=VL/VT
05990 PHIDIS=2.*A**4.*B**4.+2./3.*C**4.-4.*SQRT(2.)/3.*B**3.*C

```

(+)

ORIGINAL PAGE IS
OF POOR QUALITY

```
06000      1 +4.*(R*C)**2.-4./3.*A**2.*(B**2.*C**2.)
06010      LB=SA2*X*X*SY2*(FLY*X1*X1*FTY)*FL*FL*(SA3*PHI*SA4*PHIEM)
06020      1 +SA5*X*X*SY2*PHI0IS
06030      RETURN
06040      END
06050C *****
06060      SUBROUTINE ROOT(F,A,B,TOL)
06070C *****
06080      Z=1.0
06090      FA=F(A)
06100      IF(FA.GT.0.0) Z=-1.0
06110      7 X=(A+B)/2.0
06120      Y=F(X)
06130      IF(Y*Z) 10,100,20
06140      10 A=X
06150      GO TO 30
06160      20 B=X
06170      30 IF(B-A.LT.TOL) RETURN
06180      GO TO 7
06190      100 RETURN
06200      END
06210C *****
06220      SUBROUTINE INTEG(F,R,A,B,V)
06230C *****
06240      V=0.0
06250      DEL=0.0001*(B-A)
06260      X=R
06270      100 Y=X*DEL
06280      DEL=5.*DEL
06290      IF(Y.GT.B) Y=B
06300      CALL SIMP(F,X,Y,0.01,10,SP,VAL,N,IE)
06310      WR1(6,) X,Y,SP,VAL,N,IE
06320      V=V+AL
06330      IF(Y.EQ.B) GO TO 200
06340      X=Y
06350      GO TO 100
06360      200 DEL=0.0001*(B-A)
06370      Y=R
06380      300 X=Y-DEL
06390      DEL=5.*DEL
06400      IF(X.LT.A) X=A
06410      CALL SIMP(F,X,Y,0.01,10,SP,VAL,N,IE)
06420      WRITE(6,) X,Y,SP,VAL,N,IE
06430      V=V+VAL
06440      IF(X.EQ.A) RETURN
06450      Y=X
06460      GO TO 300
06470      END
06480C *****
06490      FUNCTION FMN(Y)
06500C *****
06510      REAL LR,NP1,NP2
06520      COMMON /VAR/ Z,CON
06530      COMMON /NM/ N,M
06540      COMMON /CONST2/ BETA,DELTA,BI
06550      COMMON /CONST3/ THETA1,THETA2,GINF2,G02,EPHI0,EPHI1,EPHI2,
06560      1 VL,VT,A2,A3,A4,A5
06570      COMMON /CONST4/ NP1,NP2,X1,X2,A1
06580
06590      X=Y-BI
06600      CALL RSL(Y,RP1,RP2,RM1,RM2,SP1,SP2,SM1,SM2,LB)
06610      XM=0.0
06620      XN=0.0
06630      IF(X.EQ.0.0) GO TO 10
06640      XM=X**M
06650      XN=X**N
06660      10 XMN=XM*XN
06670      XP1N=(X+THETA1)**N
06680      XP2N=(X+THETA2)**N
06690      XM1N=0.0
06700      XM2N=0.0
06710      IF(X-THETA1.LE.0.0) GO TO 20
06720      XM1N=(X-THETA1)**N
06730      20 IF(X-THETA2.LE.0.0) GO TO 30
06740      XM2N=(X-THETA2)**N
06750      30 CONTINUE
06760      FY=FV(Y,-Z)
06770      FMN=X1*BI*XM*(FV(Y,THETA1,-Z)*(NP1+1.)*(XP1N*RP1-XN*SP1)/FY
06780      1 +FV(Y,THETA1,-Z)*NP1*H(Y,THETA1)*(XM1N*RM1-XN*SM1)/FY)
06790      2 +X2*A1*BI*XM*(FV(Y,THETA2,-Z)*(NP2+1.)*(XP2N*RP2-XN*SP2)/FY
06800      3 +FV(Y,THETA2,-Z)*NP2*H(Y,THETA2)*(XM2N*RM2-XN*SM2)/FY)
06810      4 -LB*XMN
06820      FMN=FMN+FVP(Y,-Z)
06830      RETURN
06840      END
```

```

06850C *****
06860      FUNCTION FM(Y)
06870C *****
06880      REAL L1
06890      COMMON /VAR/ Z,CON
06900      COMMON /NM/ N,M
06910      COMMON /CONST2/ BETA,DELTA,BI
06920      X=Y-BI
06930      XM=0.0
06940      IF(X.EQ.0.0) GO TO 10
06950      XM=X**M
06960 10  CONTINUE
06970      FM=-FVP(Y,-Z)*L1(Y)*XM
06980      RETURN
06990      END
07500      SUBROUTINE HCSPOL(X,THT1,THT2,THL1,THL2,ESTR1,ESTR2,EPS0,
07510      1EPSI,EC1,EC2)
07520      ESTR1=2.96
07530      ESTR2=2.35
07531      XM1=1.295058E-22
07532      XM2=9.923396E-23
07533      A=(6.460+0.21*X)*1.0E-8
07540      EPSI=15.1077-13.8823*X+9.88928*X*X-3.67133*X*X*X
07550      EPS0=20.286-15.1531*X+6.59091*X*X-0.951826*X*X*X
07560      WT2=152.0-9.0*X
07570      WT1=118.0+12.0*X
07580      ES=4.80325E-10
07590      HB=1.0545919E-27
07600      BK=1.380622E-16
07610      PI=3.141593
07620      C=2.9979250E10
07630      THT1=2.*PI*C*HB/BK*WT1
07640      THT2=2.*PI*C*HB/BK*WT2
07641      OMT1=BK*THT1/HB
07642      OMT2=BK*THT2/HB
07643      F1=4.*PI/(A**3./4.)*ESTR1**2./XM1*(1.-X)*ES**2.
07644      F2=4.*PI/(A**3./4.)*ESTR2**2./XM2*X*ES**2.
07645      S1=F1/OMT1**2.
07646      S2=F2/OMT2**2.
07650      THLM2=1./2./EPSI*(EPSI*(THT1**2.+THT2**2.)*S1*THT1**2.
07660      1+S2*THT2**2.-SQRT((EPSI*(THT2**2.-THT1**2.)*S2*THT2**2.
07670      2-S1*THT1**2.))*2.+4.*THT1**2.*THT2**2.*S1*S2))
07680      THLP2=1./2./EPSI*(EPSI*(THT1**2.+THT2**2.)*S1*THT1**2.
07690      1+S2*THT2**2.-SQRT((EPSI*(THT2**2.-THT1**2.)*S1*THT2**2.
07700      2-S1*THT1**2.))*2.+4.*THT1**2.*THT2**2.*S1*S2))
07710      THL0=SQRT((EPSI*S1/EPSI)*THT1
07720      THL12=THLM2
07730      THL22=THLP2
07740      IF(THT2.GT.THL0) GO TO 10
07750      THL12=THLP2
07760      THL22=THLM2
07770 10  THL1=SQRT(THL12)
07780      THL2=SQRT(THL22)
07781      THL1=(THL1+THL2)/2.
07782      THL2=THL1
07860      EC1=ESTR1/EPSI
07870      EC2=ESTR2/EPSI
07880      RETURN
07890      END
00200$FIXED
04200      SUBROUTINE CUBE(B,C,D,E1,E2,E3)
04210C *****
04220C      CUBE          WRITTEN 9/19/74          JMP
04230C
04240C      COMMENTS:
04250C
04260C      THIS ROUTINE SOLVES THE GENERAL CUBIC EQUATION
04270C
04280C       $X**3 + B*X**2 + C*X + D = 0$ 
04290C
04300C      HAVING ONLY REAL SOLUTIONS. E1 > E2 > E3.
04310C      IT IS ASSUMED THAT ALL SOLUTIONS ARE REAL.
04320C *****
04330C      REAL E(3)
04600      COMPLEX W,X1,X2,X3,F,SD,Y,Z,S
05200      W=CMPLX(-.5,SQRT(3.)/2.)
06200      P=(-(B*B/3.)*C
07200      Q=(2.*B*B*B/27.)-(C*B/3.)*D
08200      F=(Q*Q/4.)*(P*P/27.)
09200      SD=CSQRT(F)
11200      S=SD-Q/2.
11300      Y=0.0
11400      IF(CABS(S).NE.0.0) Y=CEXP(CLOG(S)/3.)
11500

```

(+)

```
11900 S=-SU-Q/2.
12000 Z=0.0
12100 IF (CABS(S).NE.0.0) Z=CEXP(CLOG(S)/3.)
12200 X1=Y+Z-B/3.
12300 X2=W*Y+W*W*Z-B/3.
12400 X3=W*W*Y+W*W*Z-B/3.
12500 E(1)=REAL(X1)
12600 E(2)=REAL(X2)
12700 E(3)=REAL(X3)
12800 DO 100 I=1,2
12900 J=I+1
13000 DO 100 K=J,3
13100 IF (E(I).GE.E(K)) GO TO 100
13200 X=E(I)
13300 E(I)=E(K)
13400 E(K)=X
13500 100 CONTINUE
13600 E1=E(1)
13700 E2=E(2)
13800 E3=E(3)
13900 RETURN
14000 END
00050$FREE
00060$SOURCE:INTRPL.M0326B
00100 SUBROUTINE FFCTS
00120 COMMON ETATAB(241),FTM12(241),FT12(241),FT32(241),FT52(241),
00130 FT72(241)
00130 CALL OPEN(4,'FRTBLS.M0326B ',0,1)
00140 DO 10 I=1,241
00150 10 ETATAB(I)=(I-1)/10.
00160 READ(4, '(FTM12(I),I=1,241),(FT12(I),I=1,241),(FT32(I),I=1,241)
00170 , (FT52(I),I=1,241),(FT72(I),I=1,241)
00175 CALL CLOSE(4)
00180 RETURN
00190 END
00200 FUNCTION F(K2,ETA)
00210 DIMENSION CON(4,5)
00220 COMMON ETATAB(241),FTM12(241),FT12(241)
00230 DATA CON/1.7724539,1.4142136,-.41123351,-1.7756866,
00240 ,88622593,2.8284271,1.2337005,1.0654119,
00250 ,1.3293404,5.6568542,6.1685027,-1.7756866,
00260 ,3.323351,11.313708,14.393173,12.429806,
00270 ,11.631728,22.627417,25.907711,111.86825/
00280 IK=(K2+3)/2
00290 X=ETA
00300 IF (X.GE.-4.) GOTO 10
00301 EXPX=0.0
00302 IF (X.LE.-200.) GO TO 5
00310 EXPX=EXP(X)
00311 5 CONTINUE
00320 F=CON(1,IK)*EXPX*(1.-EXPX/CON(2,IK))
00330 RETURN
00340 10 IF (X.GT.20.) GOTO 20
00350 CALL INTRPL(X,ETATAB,FT12(1),17,241,F,IND)
00360 IF (IND.EQ.0) RETURN
00370 WRITE(6,8001) K2,X
00380 8001 FORMAT('INTERPOLATION ERROR IN F(,I2,1/2.,012.5,')')
00390 CALL EXIT
00400 20 XM2=X**(-2)
00410 XKP1=IK-.5
00420 F=X**XKP1/XKP1*(1.+CON(3,IK)*XM2*CON(4,IK)*XM2**2)
00430 RETURN
00440 END
00050$FREE
00100C LAGRANGIAN INTERPOLATION ROUTINE
00110 SUBROUTINE INTRPL(X,TABX,TABY,NC,N,Y,IND)
00120C X=INDEPENDENT VARIABLE
00130C TABX=X ARRAY
00140C TABY=Y ARRAY
00150C NC - CONTROL WORD
00160C 1 TENS POSITION - EXTRAPOLATION OUTSIDE RANGE OF X IN TABLE
00170C 0 NO
00180C 0 YES
00190C 0 UNITS POSITION - DEGREE OF INTERPOLATION (1-7)
00200C N=NO. OF VALUES IN TABLE
00210C Y=DEPENDENT VARIABLE RETURNED TO CALLING PROGRAM
00220C IND=ERROR INDICATOR RETURNED TO CALLING PROGRAM
00230C DIMENSION TABX(1),TABY(1)
00240 NC=IABS(NC)
00250 IF (NC.GE.10) GOTO 65
00260 KEY=0
00270 GOTO 70
00280 65 KEY=1
00290 KC=KC+10
00300 70 IDX=KC
```

ORIGINAL PAGE IS
OF POOR QUALITY

ORIGINAL PAGE IS
OF POOR QUALITY

```

00310 IND=0
00320 XA=X
00330 CALL DISSER(XA,TABX,N,IDX,NPX,KEY,IND)
00340 CALL LAGRAN(XA,TABX(NPX),TABY(NPX),IDX+1,1)
00350 RETURN
00360 END
00370 SUBROUTINE DISSER(XA,TAB,NX,IDX,NPX,KEY,IND)
00380C DISSER LOCATES XA IN TAB AND RETURNS WITH
00390C NPX=LOWER LIMIT FOR SUMMATION. IND=1 IF ERROR
00400 DIMENSION TAB(1)
00410 IF (NX.GT.IDX+1) GOTO 70
00420 ID=NX-1
00430 70 IF (XA-TAB(1)) 71,73,72
00440 71 IND=IND+1
00450 IF (KEY.EQ.0) GOTO 74
00460 73 XA=TAB(1)
00470 74 NPX=1
00480 RETURN
00490 72 IF (XA-TAB(NX)) 1,77,76
00500 76 IND=IND+1
00510 IF (KEY.EQ.0) GOTO 78
00520 77 XA=TAB(NX)
00530 78 NPX=NX-ID
00540 RETURN
00550C IF DISSER TAKES THIS PATH XA IS WITHIN RANGE OF TAB
00560 1 NPT=ID+1
00570 IF (XA.EQ.NPT) GOTO 74
00580 NPB=NPT/2
00590 NPU=NPT-NPB
00600 10 NLOW=1+NPB
00610 NUPP=NX-NPU
00620 IF (NX.LE.20) GOTO 18
00630 NXX=NX/2+1
00640 IF (XA-TAB(NXX)) 12,17,13
00650 13 NXX=NXX+NX/4
00660 IF (XA.GE.TAB(NXX)) GOTO 17
00670 NLOW=NXX-NX/4
00680 GOTO 18
00690 12 NXX=NXX-NX/4
00700 IF (XA.LT.TAB(NXX)) GOTO 18
00710 17 NLOW=NXX
00720 18 DO 19 II=NLOW,NUPP
00730 NLOC=II
00740 IF (TAB(II).GE.XA) GOTO 20
00750 19 CONTINUE
00760 NPX=NUPP-NPB+1
00770 RETURN
00780 20 NL=NLOC-NPB
00790 NU=NL-ID
00800 DO 25 JJ=NL,NU
00810 NDIS=JJ
00820 IF (TAB(JJ).EQ.TAB(JJ+1)) GOTO 30
00830 25 CONTINUE
00840 NPX=NL
00850 RETURN
00860 30 IF (TAB(NDIS).LT.XA) GOTO 40
00870 NPX=NDIS-ID
00880 RETURN
00890 40 NPX=NDIS+1
00900 RETURN
00910 END
00920 SUBROUTINE LAGRAN(XA,X,Y,N,SUM)
00930C LAGRAN PERFORMS THE SUMMATION
00940 DIMENSION X(1),Y(1)
00950 SUM=0.0
00960 DO 3 I=1,N
00970 PROD=Y(I)
00980 DO 2 J=1,N
00990 A=X(I)-X(J)
01000 IF (A.EQ.0.0) GOTO 2
01010 B=(XA-X(J))/A
01020 PROD=PROD*B
01030 2 CONTINUE
01040 3 SUM=SUM+PROD
01050 RETURN
01060 END
001005FIXED
00110C *****
00120 SUBROUTINE SIMP(F,A,B,DEL,IMAX,S1,S,N,IER)
00130C *****
00140C SIMPSON INTEGRATION ROUTINE.
00170 N=0
00180 BA=B-A
00190 IF (BA\20,19,20

```

```

00200 19 IER=1
00210 RETURN
00220 20 IF (DEL) 22,22,23
00230 22 IER=2
00240 RETURN
00250 23 IF (IMAX=1) 24,24,25
00260 24 IER=3
00270 RETURN
00280 25 X=BA/2.*A
00290 NHALF=1
00300 SUMK=F(X)*BA*2./3.
00310 S=SUMK*(F(A)+F(B))*BA/6.
00320 DO 28 I=2,IMAX
00330 SI1=S
00340 S=S-SUMK/2./2.
00350 NHALF=NHALF*2
00360 ANHMF=NHALF
00370 FRSTX=A*(BA/ANHMF)/2.
00380 SUMK=F(FRSTX)
00390 XK=FRSTX
00400 KLAST=NHALF-1
00410 FINC=BA/ANHMF
00420 DO 26 K=1,KLAST
00430 XK=XK+FINC
00440 26 SUMK=SUMK+F(XK)
00450 SUMK=SUMK*2.*BA/(3.*ANHMF)
00460 S=S+SUMK
00465 IF (S.EQ.0.0) GO TO 29
00470 IF ((ABS(S-SI1)/ABS(S))-DEL) 29,28,28
00480 28 CONTINUE
00490 IER=4
00500 OUTPUT(108) IER,SI1,S
00510 GO TO 30
00520 29 IER=0
00530 30 N=2*NHALF
00540 RETURN
00550 END

```

ORIGINAL PAGE 19
OF POOR QUALITY